Phosphorescent Metal Complexes and Their Molecular Aggregates for Stable and Efficient Organic Light-Emitting Diodes

by

Linyu Cao

A Dissertation Presented in Partial Fulfilment
of the Requirements for the Degree
Doctor of Philosophy

Approved August 2021 by the
Graduate Supervisory Committee:

Jian Li, Chair
James Adams
Terry Alford

ARIZONA STATE UNIVERSITY

December 2021

ABSTRACT

Over the past three decades, significant progress in the development of organic light-emitting diodes (OLEDs) has been achieved, enabling OLEDs to become a main component in state-of-the-art displays and next generation solid-state lighting. As this technology advances, it is highly desirable to further improve the device efficiency and operational stability to drive the success of OLEDs in future display and lighting applications. This dissertation aims at developing novel organic emitting materials covering visible and near-infrared (NIR) emissions for efficient and table OLEDs.

Firstly, a series of tetradentate Pd(II) complexes, which have attractive phosphorescent aggregate emission performance especially at high brightness level in device settings, have been developed. The luminescent lifetime of Pd(II) complex aggregates was demonstrated to be shorter than 1 μs with a close-to-unity photoluminescence quantum yield. Moreover, a systematic study regarding structure-property relationship was conducted on four tetradentate Pd(II) complexes, i.e., Pd3O3, Pd3O8-P, Pd3O8-Py2, and Pd3O8-Py5, featuring aggregate emission. As a result, an extremely efficient and stable OLED device utilizing Pd3O8-Py5 was achieved. It demonstrated a peak external quantum efficiency (EQE) of 37.3% with a reduced efficiency roll-off retaining a high EQE of 32.5% at 10000 cd m^{-2}, and an estimated LT_{95} lifetime (time to 95% of the initial luminance) of 48246 h at 1000 cd m^{-2}.

Secondly, there is an increasing demand for NIR OLEDs with emission spectra beyond 900 nm to expand their applications in biometric authentication, night vision display, and telecommunication, etc. A stable and efficient NIR Pt(II) porphyrin complex named PtTPTNP-F_8 was developed, and exhibited an electroluminescent spectrum at 920

nm. By carefully choosing the host materials, an PtTPTNP-F_8 based NIR OLED achieved a EQE of 1.9%. Furthermore, an PtTPTNP-F_8 OLED fabricated in a stable device structure demonstrated extraordinary operational stability with LT_{99} of >1000 h at 20 mA cm^{-2}.

Lastly, a series of imidazole-based blue Pt(II) complexes were developed and studied. Results indicated that structural modification of ligand molecules effectively tuned the emission spectral wavelength and bandwidth. Two blue complexes, i.e., Pt2O2-P2M and Pt2O2-PPy5-M, emitting at 472 and 476 nm respectively, exhibited narrow-band emission spectra with a full width at half maximum of 16 nm.

ACKNOWLEDGMENTS

I would like to acknowledge the support and encouragement I received during my PhD journey. This dissertation would not haven't been possible without the contribution of many people along the way. To start with, I would like to thank my advisor, Dr. Jian Li, for his support during these years, and the opportunity to work on such exciting projects. His insightful and challenging feedback pushed me to sharpen my thoughts and brought my work to a higher level. I would also like to acknowledge the hard work and time invested by my committee members, Dr. James Adams and Dr. Terry Alford, in my comprehensive exam and dissertation defense.

I would like to offer my thanks to the wonderful chemists and engineers with whom I have worked throughout my whole Ph.D. program: Dr. Zhi-Qiang Zhu, Dr. Jiang Wu and Dr. Yunlong Ji for their expertise in, advice on and assistant with organic synthesis and characterization; Dr. Kody Klimes for receiving training on and aid in optical instruments, device fabrication and characterization, and learning detailed knowledge of high-vacuum deposition chamber from him; Jingjun Li for her help with the preparation of platinum porphyrin complexes; Dr. Liang Huang for his invaluable experience in metal porphyrin complex synthesis; Lydia Ameri and Dr. Samuel shin for all the inspiring conversations we had regarding our research projects, and Lydia for her continued assistance with materials and devices investigations. I am also very grateful to Dr. Tyler Fleetham at Universal Display Corporation for his help in material characterization.

In addition, I would like to thank my friends and family for their love and support. Most of all, I would like to particularly thank my supportive husband. His love,

encouragement, and patience helped me to get through the difficult times during my PhD journey.

Lastly, I acknowledge the financial support provided by Universal Display Corporation and Department of Energy.

TABLE OF CONTENTS

Page

CHAPTER Page

CHAPTER Page

LIST OF TABLES

Table Page

LIST OF FIGURES

Figure Page

Figure Page

Figure Page

Figure Page

Figure Page

Figure Page

Figure Page

1 INTRODUCTION

1.1 Organic Light-Emitting Diodes

In 1963, M. Pope and co-workers revealed that they observed the electroluminescence in single crystal anthracene at ~400 V with about 10^{-1} mole% tetracene as an impurity.[1] In 1965, Pope's team proposed that the electroluminescence in anthracene was generated from electron-hole recombination by judicious experimental design. They conclude that the holes are produced by the acceleration which takes place via injection of the electrons into an upper and broad electron conduction band.[2] In the same year, W. Helfrich and co-coworker also reported that the recombination of electrons and holes in anthracene single crystal led to the fluorescence which was proved by the dependence of current and light intensity through conducting the preliminary measurement of the light output.[3] However, in order to realize the electroluminescence, very high voltages have to be applied to inject charges into these organic crystals. Therefore, from a practical perspective, it is highly desired to develop organic light-emitting diodes (OLEDs) operating at low driving voltages.

In 1987, C. W. Tang and S. A. VanSlyke constructed a novel thin-film organic device consisting of a double layered organic thin films compared with previous single layered organic electroluminescent cells.[4] Such thin film light emitting diode demonstrated a respectable device efficiency; especially, it can be driven at a much lower voltage range below 10 V, expediting the progress of organic electroluminescent device towards practical applications. Since then, considerable interest in OLEDs from both academia and industry has been ignited.

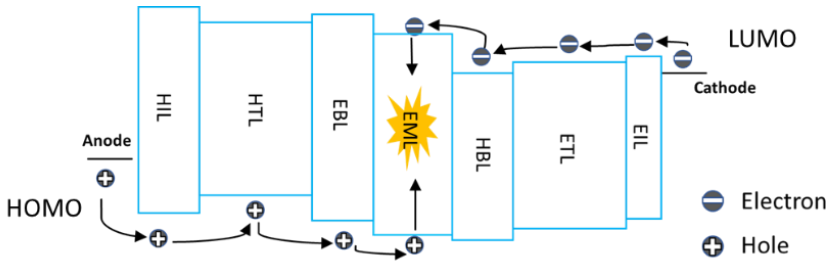

Figure 1.1 Schematic drawing of OLED device consisting of an anode, hole injection layer (HIL), hole transporting layer (HTL), electron blocking layer (EBL), emissive layer (EML), hole blocking layer (HBL), electron transporting layer (ETL), electron injection layer (EIL), and cathode.

As shown in Figure 1.1, an OLED device is composed of multiple functional organic layers situated between two electrodes, i.e., anode and cathode. Typically, a bottom-emitting OLED is fabricated by vacuum-depositing organic thin films on a pre-patterned ITO substrate and with an aluminum (Al) cathode grown on top. Holes and electrons are injected from the anode and cathode, respectively, and move towards each other and eventually recombine on an emitting molecule inside the emissive layer, leading to the formation of excitons. These excited emitters, i.e., excitons will decay to ground state, thereby generating light emission.

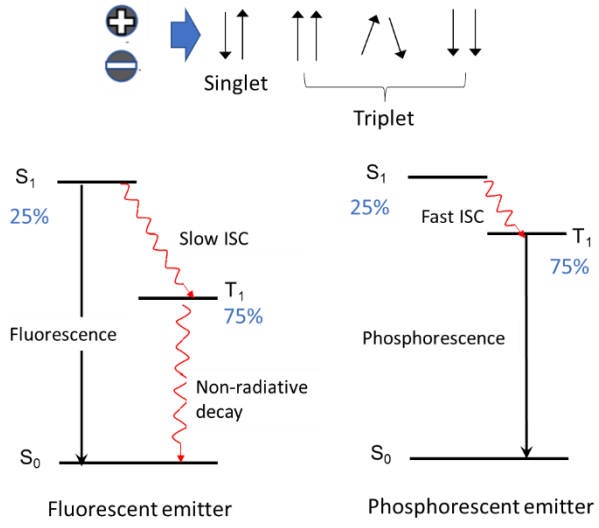

Figure 1.2 Fluorescence and phosphorescence formation processes.[5]

The electron-hole recombination process can form 25% of singlet and 75% of triplet excitons, as shown in Figure 1.2.[5] For fluorescent emitters, the transition from triplet exciton to singlet ground state requires electron spin-flip, resulting in a long-lived excited state. In comparison, fluorescence from singlet exciton to ground state features a fast radiative decay process because there is no change in electron spin from excited to ground state.[6] Thus, for OLEDs utilizing fluorescent emitters, the maximum internal quantum efficiency (IQE) can only realize 25%, and a large portion of injected electrons, i.e., 75%, are wasted into heat.

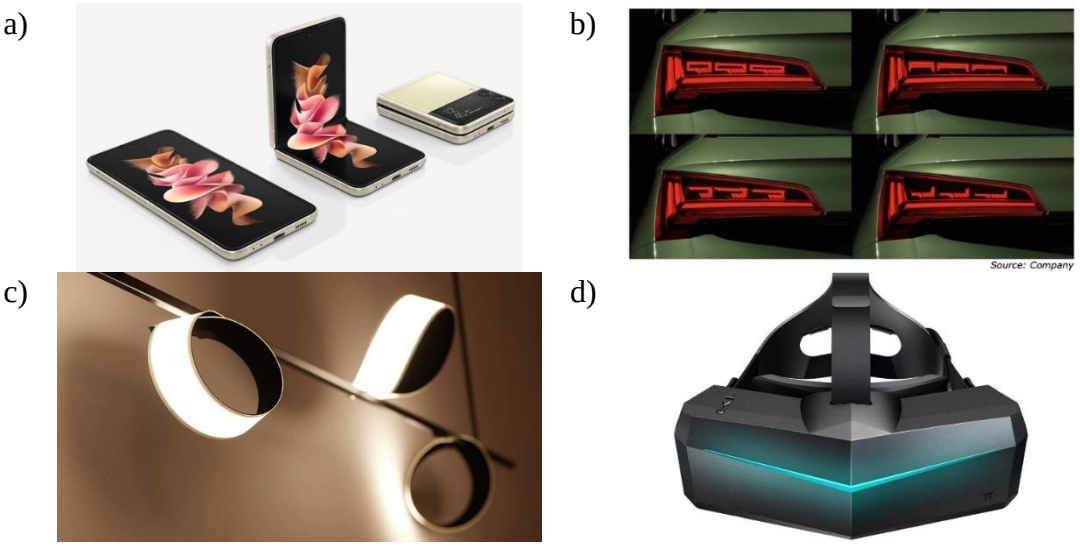

Figure 1.3 (a) Samsung's Galaxy Z Flip 3 with a foldable OLED display. (b) Audi Q5 luxury SUV with OLED tail-lights. (c) Flexible OLED light panels by LG Display. (d) Pimax 5K XR OLED VR virtual reality headset.

Over the past three decades, both the academic and industrial communities have working relentlessly to improve the device performance in efficiency and reliability by continuously extending the emitting material systems and improving the device architecture, etc.[7–26] Therefore, OLED has become a main component in state-of-the-art displays, as well as in next-generation solid-state lighting applications.[27, 28] As

shown in Figure 1.3, lots of OLED related products are springing up in the market, such as foldable phones, ecofriendly energy-saving lighting products or even AR/VR headsets. Despite the fact of the commercialization of OLED technology, some drawbacks have hindered their further development and applications in high-resolution display and cost-effective lighting. OLEDs typically experience expedited degradation processes at a high brightness range, leading to drastically decreased efficiency called efficiency roll-off and significantly shortened operational lifetime.[29] Therefore, it is highly desirable to develop efficient and stable OLEDs under conditions of high-brightness operation.

1.2 Excited State Interactions in OLEDs

There is a common phenomenon in most OLEDs that their efficiency tends to decrease as brightness increases, which is known as efficiency roll-off. Enormous efforts have been taken to understand the underlying processes and to develop methods to improve the high-brightness performance of OLEDs. Research have demonstrated that multiple factors likely contributed to the so-called roll-off in efficiency, including triplet-triplet annihilation (TTA), singlet-singlet annihilation (SSA), singlet-triplet annihilation (STA), triplet-polaron quenching (TPQ), singlet-polaron quenching (SPQ), etc., as shown in Figure 1.4.[30–32] However, for phosphorescent OLEDs, TTA and TPQ are considered two main reasons to cause the fast decline in efficiency especially during high-brightness operation as a result of highly concentrated triplet excitons and polarons.[13, 33]

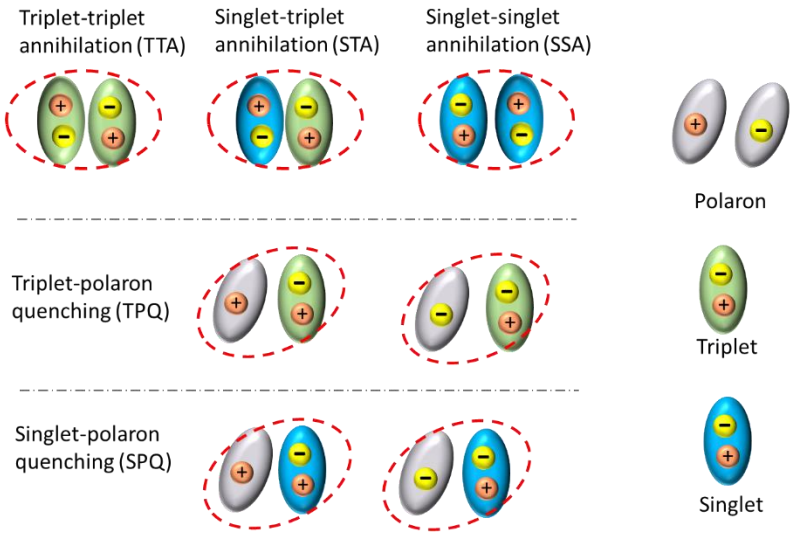

Figure 1.4 Schematic illustration of the highly possible interactions among excited states in OELDs.

For TTA, two triplets form an intermediate state X, which consequently transfer into one singlet and three triplets according to spin statistics.

$$T_1 + T_1 \xrightarrow{k_{TT}} X \begin{cases} \xrightarrow{25\%} S_n + S_0 \rightarrow S_1 + S_0 \\ \xrightarrow{75\%} T_n + S_0 \rightarrow T_1 + S_0 \end{cases}$$

Then S_1 transfers back to radiative triplet exciton via SOC; however, T_1 will be released via non-radiative pathways. Hence, 15% of triplet excitons will be lost during the whole process, leading to a significant efficiency loss in the phosphorescent OLEDs. OLEDs usually adopt host-guest systems, i.e., phosphorescent emitters doped in host materials, to avoid self-absorption of emitters and concentration quenching. Although various TTA forms can occur due to the triplet interactions among guest and/or host molecules, TTA occurring on guest molecules, i.e., guest-guest TTA, is typically assumed to be dominant.

For the occurrence of TTA, two triplet excitons must be in close proximity. Triplets could move towards each other though Dexter or Förster energy transfer.[11, 34] Dexter energy transfer requires a short distance (~2 nm) to realize a wavefunction

overlap. In contrast, Förster energy transfer is a long-range (typically 0.8-5 nm) energy transfer. Staroske et al. indicated that the dominant mechanism of TTA is the singlet-step long-range Förster energy transfer between two excited guests.[35] However, some researcher believed Dexter energy transfer is more relevant to TTA in practical systems due to aggregation of emitter molecules within matrix material, evidenced by the observation of 3-30 nm dopant agglomerates in the emissive layer with Ir(ppy)3 doped TCTA by Reineke and co-workers,[36] and $Ir(ppy)_3$ aggregates in CBP: $Ir(ppy)_3$ films after annealing at 80 ℃.[37] Therefore, small intermolecular distance between emitter aggregation most likely leads to enhanced diffusion-based TTA.

1.3 Phosphorescent Emitters

Many efforts have been taken to develop new emitting material systems in order to efficiently utilize both singlet and triplet excitons and realize 100% IQE of OLED devices. In the late 1990s, Forrest and Thompson and coworkers reported phosphorescent OLED devices with IQE of 100% by developing a novel organo-transition metal complex based emitters.[7] For phosphorescent metal complex, the spin-orbital coupling effect of transition metal ion largely facilitates the radiative decay from excited triplet to ground singlet state, and also induces an efficient and fast transfer from 25% populated singlets to emitting triplets, as depicted in Figure 1.2. Since then, numerous phosphorescent emitters (such as Ir(III), Pt(II) or Pd(II) based complexes etc.) emitting in the visible or even near-infrared (NIR) range have been developed.[6, 20, 21, 38–42]

In general, photoluminescent properties of metal complexes are largely determined by the nature of their molecular orbitals (MOs), which are mainly responsible for the electronic ground state and the lowest excited state. Metal complex based

phosphorescent emitters typically possess three transition characters: ligand-centered (LC) excitons with π-π^* character, metal-centered (MC) excitations characterized d-d^* character, and metal-to-ligand charge transfer (MLCT) excitations featuring d-π^* character.[43–46]

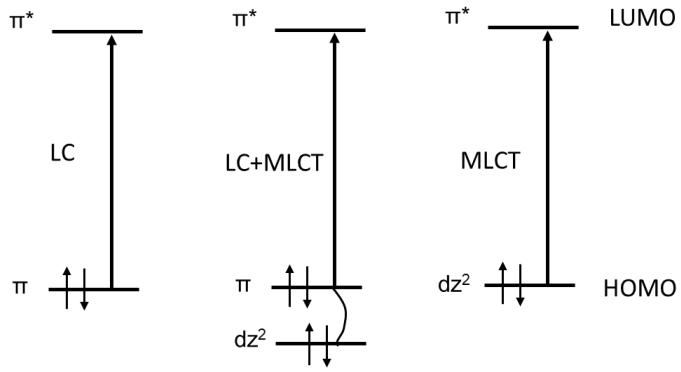

Figure 1.5 Schematic diagram of frontier molecular orbitals involved in various emitting scenarios.

1.4 Beyond Conventional Phosphorescent Monomer Emission: Phosphorescent Molecular Aggregate Based Emission

In the recent years, phosphorescent aggregate based emitting molecules, such as excimers and dimers etc., have emerged as a new class of emitters.[47–57] Phosphorescent aggregate based emitters achieved great performance in the visible as well near-infrared (NIR) emission range. Kim and coworkers reported an efficient phosphorescent Pt(II) complex aggregates based OLED with a maximum EQE of 38.8% due to their high horizontal emitting dipole ration of 93% as well as photoluminescent quantum yield of 96%. It has been well documented that if the emitting dipoles are 100% parallel to the substrate, an EQE of 45% can be realized without any outcoupling enhancement compared to 20-25% with random oriented emitting dipoles.[16, 58] Wei et al. developed a series of Pt(II) complexes that emitted in aggregate form at 866–960 nm

with a photoluminescence quantum yield of 5–12% in solid films. An OLED utilizing the molecular aggregates of a Pt(II) complex demonstrated a emission peaking at 930 nm and a EQE of 2.0% (Figure 1.6).[40]

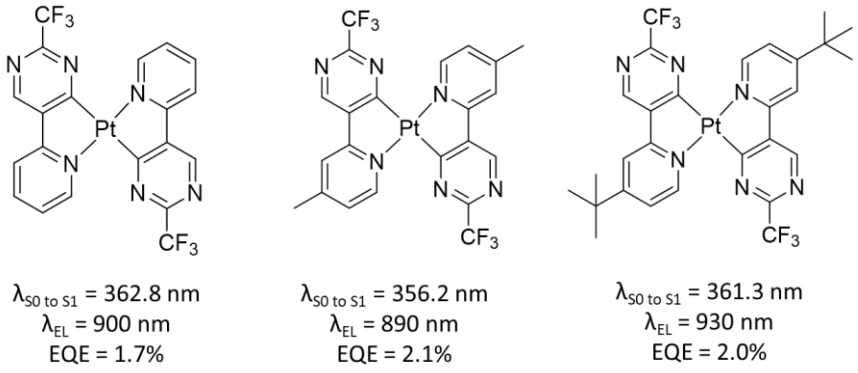

Figure 1.6 Photophysical properties and device performance of three bidentate Pt(II) complexes.[40]

Ma and coworkers synthesized a series of pyrazolate-bridged cyclometalated platinum(II) complexes. By adding substituting bulky groups to the pyrazole bridge, Pt-Pt distance were elaborately controlled, through which the emission color was adjusted. Results indicated when the Pt(II) complex has an shorter Pt-Pt spacing, it showed a red-shifted emission which was assigned to a triplet metal-metal-to-ligand charger transfer (MMLCT) involving charge transfer between a filled Pt-Pt antibonding σ* orbital and a vacant, ligand-based π* orbital,[47, 59–61] as shown in Figure 1.7.

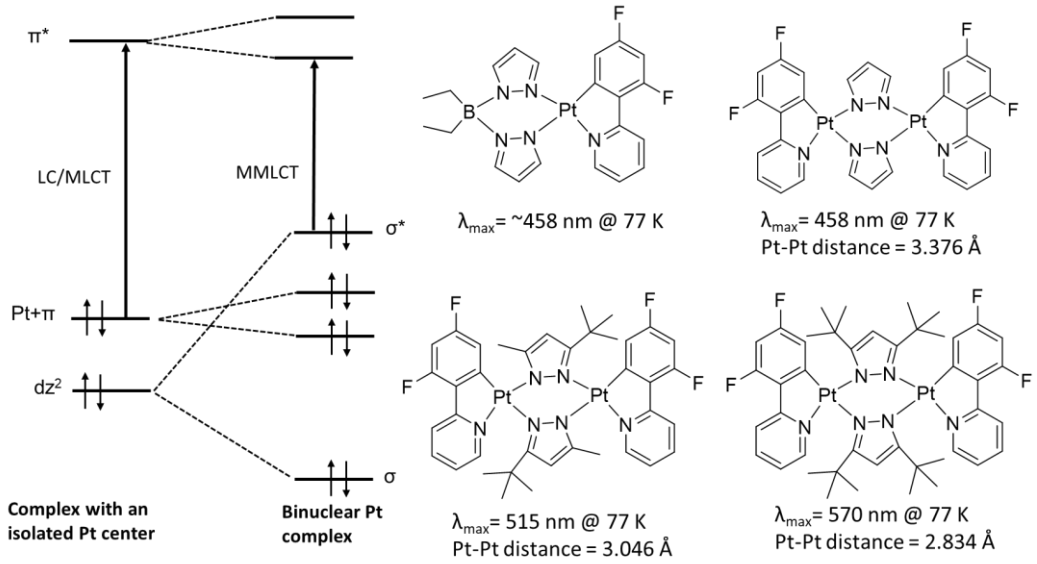

Figure 1.7 Maximum emission wavelength of four Pt(II) complexes with isolated Pt center or binuclear Pt centers, and corresponding quantum molecular orbital scheme.[48]

Compared to conventional phosphorescent monomer emission, one advantage of phosphorescent aggregate emission stands out. Through adjusting the dopant concentration of emitter in the host, intermolecular spacing will be affected. As a result, emission from a single-doped emissive layer includes both blue monomer emission and broad aggregate emission in the red emission range, which can potentially cover the visible emission range, thereby realizing the white emission by a single emitting molecule. By comparison, there are several approaches to fabricate WOLEDs including tandem or striped device, blue devices with down-conversion phosphors, multiple emissive layers within a single device, or multiple emissive dopants within a single emissive layer.[62] However, incorporating several colors in one single device will generate two problems: poor stability of color, which is caused by energy transfer between different emitters and driving voltage dependence of emitters; color aging, which is due to the different degradation process for each emissive dopant in WOLEDs.

Thus, it will be an elegant solution to fabricate WOLEDs using a single emitter, of which the electroluminescence spectrum is broad enough to cover the visible spectrum. Blue phosphorescent metal complex with aggregate emission has been considered as a strong emitter candidate for realizing single-doped white OLEDs. It is worth mentioning that the excimer-based phosphorescent aggregate emission can prevent the energy cascade from monomer to excimer due to absent ground state.

Molecular design principle for phosphorescent molecular aggregates: typically, to realize efficient aggregate emission, it requires a rigid molecular structure to suppress the non-radiative pathways of the emitter, and a planar molecular geometry to allow sufficient excimer formation. To now, almost all of excimer emitters mainly focus on Pt complexes.[63–66] In recent years, excimer based WOLEDs has been expanded to Pd complexes.[56] However, the relationship between molecular structure and aggregate emission is still poorly understood.

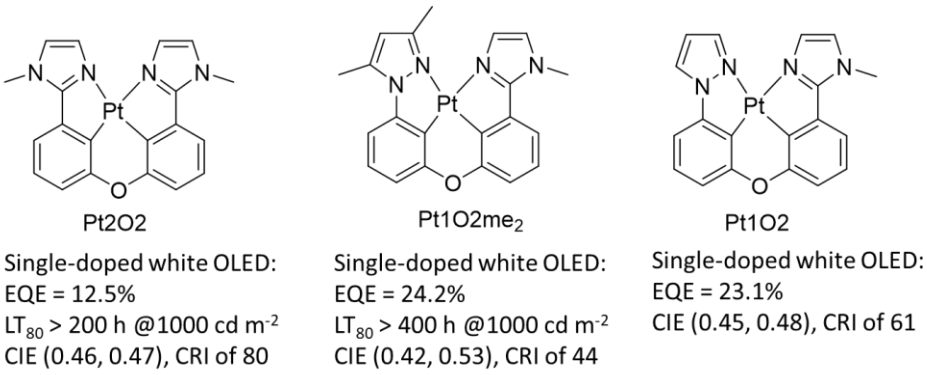

Figure 1.8 Three tetradentate Pt(II) complexes with blue monomer and red-shifted molecular aggregate emissions, and their corresponding performance in single-doped white device settings.[67]

Williams et al. first demonstrated excimer-based white phosphorescent employing platinum(II) [2-(4′6′-difluorophenyl) pyridinato-N,$C^{2'}$]2,4-pentanedionato (FPt), which

exhibited moderate EQE of 15.9%, CIE coordinates (0.46, 0.47) and poor CRI value of 69.[63] After one decade of enormous efforts, WOLEDs employing excimer-based metal complexes has gained huge development in terms of efficiency, CIE coordinates, CRI, and stability. Fleetham and coworkers report efficient and stable excimer-based WOLEDs utilizing symmetric Pt2O2, which demonstrated both efficient monomer and excimer emission.[67] A known stable device structure employing Pt2O2 achieved LT_{80} of over 200 h at 1000 cd m^{-2} with CIE of (0.46, 0.47) and a CRI of 80. Moreover, the monomer and excimer emissions can be tuned with molecular modification, yielding two complexes, i.e., Pt1O2, and $Pt1O2me_2$ with monomer emission at 474 and 472 nm, and excimer emission at 592 and 556 nm, respectively, as shown in Figure 1.8. A single-doped OLED utilizing $Pt1O2me_2$ demonstrates an LT_{80} of over 400 h at 10000 cd m^{-2}.

1.5 Dissertation Outline

This dissertation focuses on developing novel phosphorescent metal complexes based emitters for high-performance OLEDs to further push the development of OLEDs in future display and solid-state lighting applications. These newly developed emitting materials include tetradentate Pd(II) complex aggregates based amber emitters, Pt(II) porphyrin complex based NIR emitters, and tetradentate Pt(II) complex based blue emitters. Their electrochemical and photophysical properties, and/or performance in device settings were carefully investigated.

Chapter 2 provided a summary of the methods and characterizations adopted in this dissertation, including materials and OLED device characterization methods, and device fabrication procedure.

Chapter 3 explored a series of tetradentate Pd(II) complexes featuring efficient molecular aggregate emission. Firstly, a novel tetradentate Pd(II) complex named Pd3O8-P was designed and synthesized. The photophysical and electrochemical properties of Pd3O8-P, in both dilute solution and thin film with various dopant concentrations, were thoroughly studied to confirm and explore the molecular aggregate emission. Four OLED devices with various Pd3O8-P doping concentrations, i.e., 6%, 20%, 50%, and 100%, were fabricated. Their electroluminescent spectra, EQE, power efficiency, and operational lifetime were collected and analyzed. Secondly, four tetradentate Pd(II) complexes, i.e., Pd3O3, Pd3O8-P, Pd3O8-Py2, and Pd3O8-Py5, featuring aggregate emission were prepared. Electrochemical and photophysical properties of these four emitters along with their performance in device settings were explored and discussed. Moreover, the emitting dipole orientation of these Pd(II) complexes were carefully probed by varying the deposition rates and/or templating layers to further uncover the relationship between ligand structures and device performance.

Chapter 4 focused on developing a new phosphorescent emitter with emission beyond 900 nm for efficient and stable NIR OLEDs. A background was provided to elaborately describe the motivation behind this piece of research work. A Pt(II) porphyrin complex named PtTPTNP-F_8 was designed, and the molecular design concept and synthetic method were also discussed. In brief, a large conjugation system was adopted to extend the emission into longer wavelength range, and fluorine atoms was added to the metal complex to improve the material purity. The cyclic voltammetric and photoluminescent emission behaviors of PtTPTNP-F_8 were characterized. The

performance of PtTPTNP-F_8 in device settings was improved by exploring various host materials and emissive layer structures.

Chapter 5 presented three groups of Pt(II) complexes based blue emitters. The molecular design concept and synthetic method were carefully discussed. Then the photophysical properties of these emitters were investigated by examining the absorption and photoluminescent emission spectra, and cyclic voltammetry.

Chapter 6 summarized the findings of all chapters, and also discussed the future outlook of the research work presented in this dissertation.

2 MEHODS AND CHARACTERIZATION

2.1 Materials Characterization

The absorption spectrum was recorded on an Agilent 8453 UV−visible Spectrometer. The photoluminescent spectra were performed on a Horiba Jobin Yvon FluoroLog-3 spectrometer. The PLQY was carried out on a Hamamatsu absolute PL quantum yield spectrometer model C11347. Cyclic voltammetry and differential pulsed voltammetry were performed on a CHI610B electrochemical analyser in a solution of anhydrous DMF using 0.1 M tetra(*n*butyl) ammonium hexafluorophosphate as the supporting electrolyte. A ferrocene/ferrocenium (Fc+/Fc) redox couple was used as an internal reference. XRD measurements were performed on a Bruker D8 focus diffractometer using Cu Kα radiation (λ=1.5406 Å) with a step size of 0.02˚ and a scan rate of 0.6 sec/step. Density functional theory (DFT) calculations were performed using the Titan software package (Wavefunction, Inc.) at the B3LYP/LACVP** level. HPLC analysis was performed on an Agilent 1200 series LC system equipped with an Agilent Eclipse XDB-C18 column (4.6×150mm, 5 μm) at room temperature. For the sample of Pd3O8-P, the HPLC chromatogram was run with the elution solvents of acetonitrile and distilled water (97/3, v/v), and the flow rate of 1.0 mL/min. The sample was prepared by dissolving Pd3O8-P in acetonitrile and filtered through a 0.2 μm PTFE membrane syringe filter.

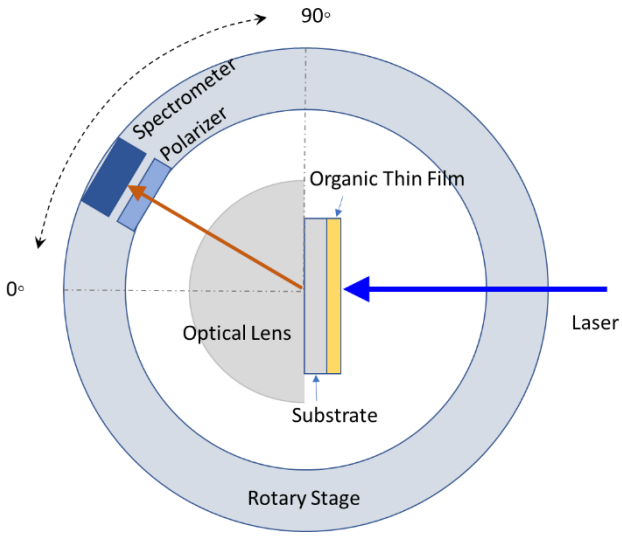

Figure 2.1 Schematic illustration of angle-dependent PL measurement setup (top view).

Angle-dependent PL measurement: As shown in Figure 2.1, Vapor-deposited organic layers on glass was attached to a half-cylinder glass with optical matching gel and then excited by an ultra-violet diode (405 nm). The PL spectrum of *p*-polarized light was detected by collecting the emission passing through a linear polarizer, and the detector (Flame-T Ocean Optics Inc. Spectrometer) was automatically rotated by a programmed rotation stage. By analyzing the angle-dependent PL intensities of the *p*-polarized light at 580 nm according to the classical dipole model, the emitting dipole orientations of these Pd complex films were determined.[68, 69, 49] The refractive indices of the Pd complex thin films were measured using a VASE ellipsometer, as shown in Figure A.1. For theoretical fitting, the refractive index of 1.7 was adopted, which was close to the refractive index value of the organic films investigated.

2.2 Device Fabrication and Characterization

The materials used in the devices were purified via train sublimation in a four-zone thermal-gradient furnace under high vacuum. Prior to deposition, the prepatterned

ITO-coated glass substrates were cleaned by subsequent sonication in deionized water, acetone, and isopropyl alcohol. Organic layers were deposited by vacuum thermal evaporation in a custom-made vacuum thermal evaporation chamber built by Travato Man. Inc. Base pressure were kept between 10^{-8} to 10^{-7} torr and deposition rates were kept between 0.5 to 1.0 Å s^{-1}, monitored by quartz-crystal microbalances. A 1 nm of LiF or 2 nm of Liq buffer layer was deposited at 0.2 Å s^{-1}. The Al cathode was deposited at 1-2 Å s^{-1} through a shadow mask without breaking vacuum, defining a device area of 0.04 cm^2. EL spectra were measured with a Horiba Jobin Yvon FluoroLog-3 spectrometer. The current–voltage–luminance and EQE measurements were measured using a Keithley 2400 Source-Meter in conjunction with a calibrated Thorlabs FDS10X10 Si photodiode. The photodiode area was considerably larger than that of the OLED, and the OLED was placed very close to the photodiode without any intervening optics. Accelerated lifetime testing was performed in a nitrogen filled glove box without encapsulation.

3 PHOSPHORESCENT MOLECULAR AGGREGATES BASED ORGANIC LIGHT-EMITTING DIODES

3.1 Efficient and Stable Organic Light-Emitting Devices Employing Phosphorescent Molecular Aggregates

3.1.1 Background

Over the past three decades, significant progress in the development of organic light-emitting diodes (OLEDs) has been achieved due to extensive research within the academic and industrial communities enabling OLEDs to become a main component in state-of-the-art displays, as well as in next generation solid-state lighting.[20, 52, 70, 4, 7, 21, 15] As this technology advances, there is a urgent need to develop stable and efficient OLEDs with higher brightness to be compatible with high resolution displays and more cost-effective lighting products.[71–73] Typically, OLEDs operating within the high brightness range experience a drastic drop in efficiency, known as the efficiency roll-off. It has been well documented that triplet-triplet annihilation (TTA) and triplet-polaron quenching (TPQ) are the two main mechanisms that cause an efficiency roll-off for phosphorescent emitters.[74, 75] Moreover, device operational stability has been demonstrated to be also closely related to TTA or TPQ in the emissive layer (EML), which generate hot (multiply excited) excitons or polarons, and in turn, induce chemical bond dissociation, resulting in the expedited device degradation process especially at the condition of high brightness operation.[30, 33]

In OLEDs with conventionally doped emissive layers, TTA and TPQ processes often occur as a result of poor charge balance inside of compact recombination zones where exciton and polaron densities are high at large driving currents.[76] This can

typically be combatted with gradient doping of the emissive material or utilizing cohost structure which both serve to spread out the recombination zone.[13, 77–81] However, at even moderate doping concentrations there is still a high likelihood of excitons interacting with other triplets or polarons on neighbouring dopant evidenced by the reduction in photoluminescent quantum yield (PLQY) of doped films of archetypical phosphors such as $Ir(ppy)_3$ or FIrpic with increasing doping concentrations.[82, 83] In contrast, highly doped or neat films of select square planar metal complexes have suppressed TTA losses and, in some cases, show enhancement in the PLQY at higher doping concentrations.[49] This enhancement coincides with the appearance of aggregate emissive species and indicates that there may be a more favourable distribution of excited-state molecular aggregates or that the interaction between discrete excitonic aggregates may be suppressed. Thus, utilizing the unique exciton dynamics of aggregate emitters, it is possible to significantly improve both the device efficiency and the operational lifetime.[23, 57, 67] Some studies regarding molecular-aggregate-based OLEDs have already demonstrated that host-free devices can realize high efficiency.[49, 50, 84] However, the operational stability of such OLEDs with aggregate emission have not been extensively investigated due to the insufficient material development efforts.

In the first part of this chapter, an efficient and stable OLEDs operating at high brightness was demonstrated by utilizing molecular aggregates of a tetradentate Pd(II) complex, i.e., palladium (II) 7-(3-(pyridin-2-yl-κN)phenoxy-κC)(benzo[4,5]imidazo-κN)([1,2-f]phenanthridine-κN) named Pd3O8-P, as shown in Figure 3.7a inset. To date, nearly all Pd(II) complexes have performed poorly at high brightness compared to Pt or Ir analogues due to the long excited state lifetimes (τ) of Pd complexes, typically in the

range of hundreds of μs.[56, 85] Pd3O8-P was designed and synthesized with a rigid molecular structure to enhance its chemical stability and a planar geometry to enable favourable intermolecular interactions and produce aggregate emission. Utilizing aggregate emission properties of Pd(II) complexes, it has been demonstrated an 100-fold reduction in the excited state lifetime to achieve a τ of 0.62 μs at room temperature. This τ value is at least an order of magnitude smaller than other reported Pd(II) emitters and is competitive with the fastest Ir and Pt complexes, which launches Pd(II) complexes into the conversation for commercial viability.[5, 15, 20, 56] A host-free Pd3O8-P device achieved an external quantum efficiency (EQE) of 34.8% without any out-coupling enhancement, retaining a high EQE of 29.5% at 10000 cd m^{-2}. Such devices exhibited a measured LT_{95} (time to 95% of the initial luminance) of 170.7 h at the brightness of 16650 cd m^{-2} and an estimated LT_{50} of 9.59 million hours at 1000 cd m^{-2}. These studies demonstrate that phosphorescent molecular aggregates can be a feasible emitter candidate for display and lighting applications, opening a new avenue of materials development in such an exciting, competitive and lucrative arena.

3.1.2 Experimental Section

Materials and regents: All commercial reagents were purchased and used as received without further purification. CuI and picolinic acid were purchased from Sigma Aldrich. K_3PO_4 were purchased from Alfa Aesar. Silica gel (40-60μm) was purchased from Agela Technologies and BDH. Solvent DMSO was purchased from Alfa Aesar. The reaction was carried out under an inert N_2 atmosphere in oven-dried glassware. External bath temperatures were used to record all reaction temperatures.

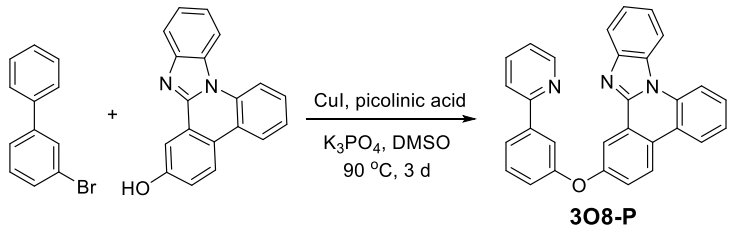

Figure 3.1 Synthesis of ligand 7-(3-(pyridin-2-yl)phenoxy)benzo[4,5]imidazo[1,2-f]phenanthridine (3O8-P).

The synthetic method of ligand 3O8-P is shown in Figure 3.1. To a three-necked flask equipped with a magnetic stir bar, added benzo[4,5]imidazo[1,2-f]phenanthridin-7-ol (2.0 g, 7.04 mmol, 1 eq), 2-(3-bromophenyl)pyridine (1.97 g, 8.45 mmol, 1.2 eq), picolinic acid (0.17 g, 1.41 mmol, 0.2 eq), K_3PO_4 (2.99 g, 14.1 mmol, 2.0 eq), and CuI (0.27 g, 14.1 mmol, 0.2 eq). Then the flask underwent the procedure of the evacuation and backfill with nitrogen for three times. Solvent of DMSO (65 mL) was added under the protection of nitrogen. Then the mixture was stirred in an oil bath at 100 °C for 3 days, then cooled down to ambient temperature. The solid was filtered off and washed with ethyl acetate. The filtrate was concentrated under reduced pressure. Then the residue was purified through column chromatography on silica gel using dichloromethane/ethyl acetate (20:1-10:1-6:1) as eluent to obtain the desired product 3O8-P as a light orange solid. Yield: 2.15 g, 70%. ^{1}H NMR (DMSO-d_6, 500 MHz): δ 7.34-7.38 (m, 2H), 7.49-7.51 (m, 2H), 7.60-7.67 (m, 3H), 7.80 (t, J = 8.0 Hz, 1H), 7.87-7.92 (m, 2H), 7.97 (s, 1H), 8.04 (t, J = 7.6 Hz, 2H), 8.12 (d, J = 2.8 Hz, 1H), 8.63-8.66 (m, 2H), 8.73 (d, J = 7.6 Hz, 1H), 8.76 (d, J = 8.9 Hz, 1H), 8.78 (d, J = 8.5 Hz, 1H).

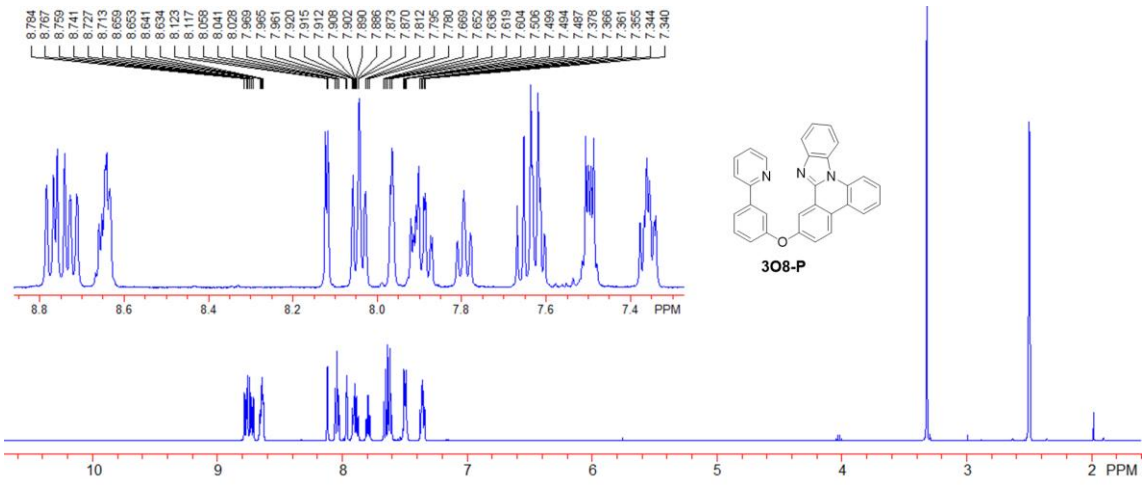

Figure 3.2 ^{1}H NMR of ligand 3O8-P.

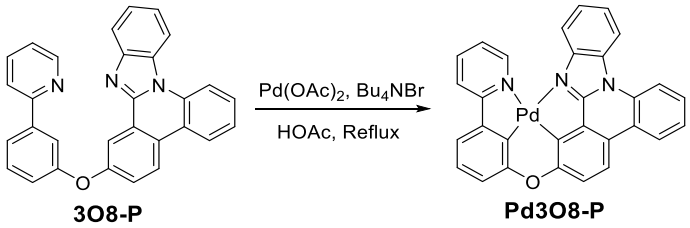

Figure 3.3 Synthesis of palladium (II) 7-(3-(pyridin-2-yl-κN)phenoxy-κC)(benzo[4,5]imidazo-κN)([1,2-f]phenanthridine-κN) (Pd3O8-P).

The synthetic method of metal complex Pd3O8-P is shown in Figure 3.3. To a three-necked flask equipped with a magnetic stir bar, added ligand 3O8-P (2.15 g, 4.9 mmol, 1 eq), $Pd(OAc)_2$ (1.32 g, 5.9 mmol, 1.2 eq), and Bu_4NBr (0.16 g, 0.5 mmol, 0.1 eq). Then the flask underwent the procedure of the evacuation and backfill with nitrogen for three times. Solvent of HOAc (280 mL) was added under the protection of nitrogen. Then the mixture was stirred in an oil bath under reflux for 3 days, then cooled down to ambient temperature. The mixture was concentrated under reduced pressure. Then the residue was purified through column chromatography on Al_2O_3 using dichloromethane as eluent to obtain the desired product Pd3O8-P as a light yellow solid. Yield: 1.72 g, 65%. The product of 1.72 g was further purified by sublimation in a four-zone thermal-gradient

furnace under high vacuum (280°C, 4.5×10^{-6} Torr). To ensure the quality, Pd3O8-P was sublimed twice to obtain the final yellow crystal. The chemical structure of Pd3O8-P was confirmed by ^{1}H NMR, and its purity was verified by HPLC, as shown in Figure 3.4 and 3.5, respectively. Yield: 1.34 g, 78%. A single chromatographic peak at a retention time of 10.483 minutes (Figure 3.5) was observed, indicating a high purity of prepared Pd3O8-P sample.^{1}H NMR (DMSO-*d6*, 500 MHz): δ 7.30 (d, *J* = 8.0 Hz, 1H), 7.35 (t, *J* = 7.6 Hz, 1H), 7.60-7.66 (m, 2H), 7.71-7.75 (m, 3H), 7.83-7.87 (m, 2H), 8.18 (t, *J* = 8 Hz, 1H), 8,28 (d, *J* = 8.2 Hz, 1H), 8.35 (d, *J* = 8.2, 1H), 8.45 (d, *J* = 8.5 Hz, 1H), 8.79 (d, *J* = 8.4 Hz, 1H), 8.87 (d, *J* = 8.3 Hz, 1H), 8.94 (d, *J* = 8.5 Hz, 1H), 9.38 (d, *J* = 5.1 Hz, 1H).

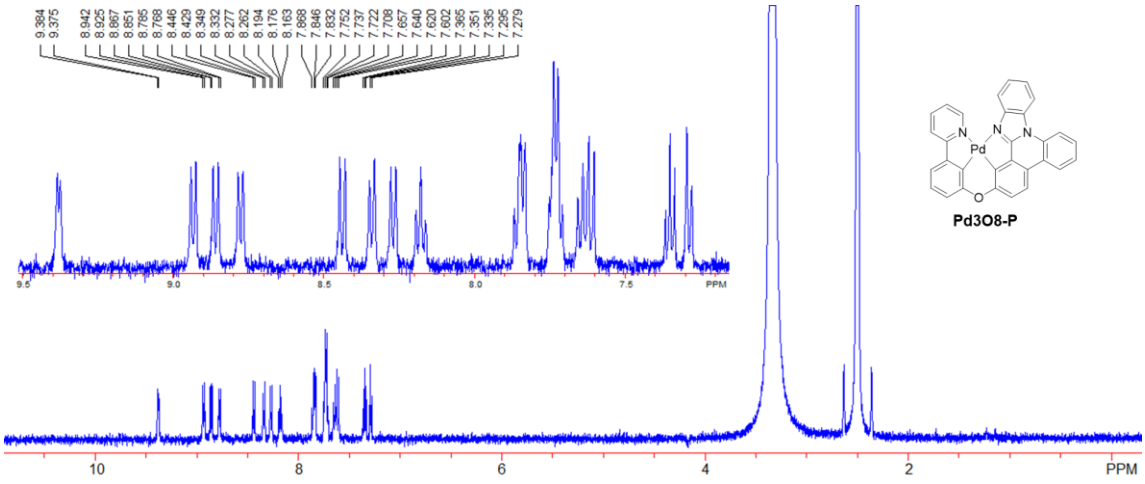

Figure 3.4 ^{1}H NMR of metal complex Pd3O8-P.

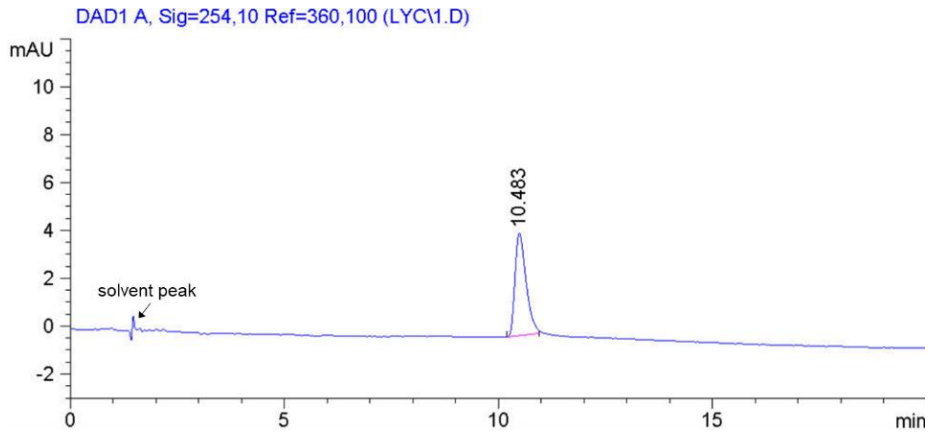

Figure 3.5 HPLC chromatogram for the analysis of Pd3O8-P.

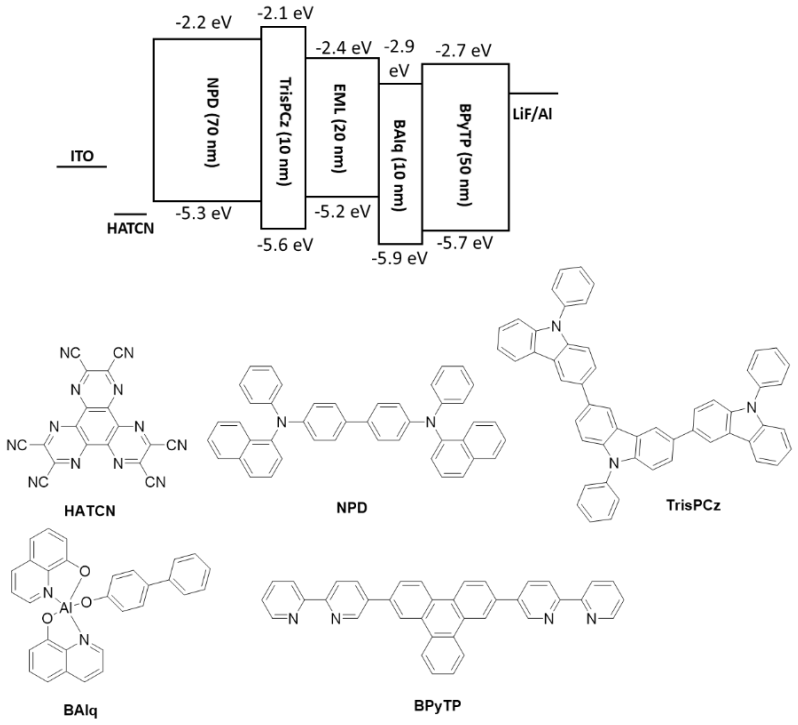

Figure 3.6 Device structure and chemical structures of the materials used in the device.

Additionally, Figure 3.6 shows a schematic diagram of the device structure fabricated in this study, and chemical structure of the materials used in each layer. The general device structure is ITO (100 nm)/ HATCN (10 nm)/ NPD (70 nm)/ TrisPCz (10 nm)/ EML (20 nm)/ BAlq (10 nm)/ BPyTP (50nm)/ LiF (1 nm)/ Al (100 nm), where ITO is indium tin oxide, HATCN is 1,4,5,8,9,11-hexaazatriphenylenehexacarbonitrile, NPD is N^4,$N^{4'}$-di(naphthalen-1-yl)-N^4,$N^{4'}$-diphenyl-[1,1'-biphenyl]-4,4'-diamine, TrisPCz is 9,9',9''-triphenyl-9H,9'H,9''H-3,3':6',3''-tercarbazole, BAlq is bis(8-hydroxy-2-methylquinoline)-(4-phenylphenoxy)aluminium, BPyTP is 2,7-di([2,2'-bipyridin]-5-yl)triphenylene, LiF is lithium fluoride, Al is aluminium.

3.1.3 Results and Discussion

The room-temperature absorption and emission spectra of Pd3O8-P in the solution of dichloromethane (DCM) and low temperature (77 K) emission spectrum in 2-methyltetrahydrofuran (2-MeTHF) are shown in Figure 3.7a. The distinct strong absorption peaks between 250 and 360 nm can be assigned to $^1(\pi\text{-}\pi^*)$ transitions on the cyclometalating ligand.[86, 87] The weak absorption band between 360 and 420 nm is attributed to metal-to-ligand charge transition (^{1}MLCT) involving both the cyclometalating ligand and the palladium metal ion. At 77 K, Pd3O8-P showed an emission peak of 464 nm indicating a triplet energy of 2.67 eV, and a long luminescent lifetime of 179 μs (Figure 3.8) which is similar to those of previously reported Pd complexes.[56, 85] At room temperature, Pd3O8-P exhibits a slightly red-shifted emission peak of 468 nm. The sharp vibronic emission peaks and the long transient photoluminescent (PL) decay indicate that the lowest triplet state of Pd3O8-P is a predominant ligand centred state (^{3}LC) with minimal MLCT admixture. Additionally, the electrochemical property of Pd3O8-P was examined by performing the cyclic voltammetry in a solution of anhydrous DMF, as shown in Figure3.9. The oxidation and reduction potentials were 0.41 V and -2.41 V respectively, determined by differential pulse voltammetry in dimethylformamide versus a ferrocene internal reference.

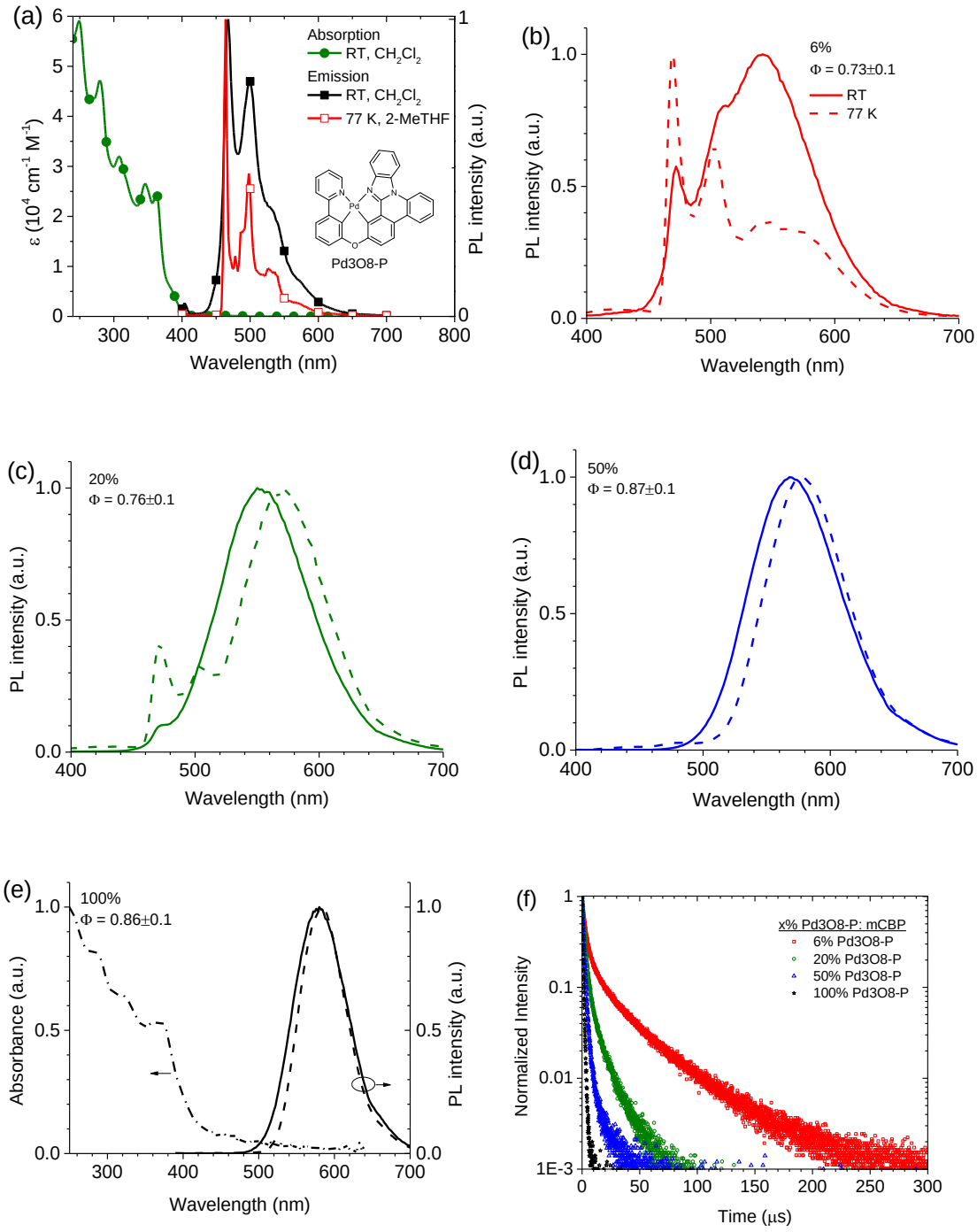

Figure 3.7 Photophysical study of Pd3O8-P in solution and thin film. a), Room-temperature absorption spectrum of Pd3O8-P (solid circles), and its photoluminescent (PL) spectra at room temperature (solid squares) and 77 K (open squares). The room-temperature absorption and PL spectra were measured in dichloromethane (DCM), and the 77 K PL spectrum was measured in 2-methyltetrahydrofuran (2-MeTHF). Inset: chemical structure of Pd3O8-P. b)-e), Room-temperature (solid lines) and 77 K (dashed

lines) PL spectra of 20-nm-thick x% Pd3O8-P: mCBP films with dopant concentrations of 6% (red), 20% (green), 50% (blue), and 100% (dark). The room-temperature absorption spectrum of neat Pd3O8-P film (dash-dotted line) is also included in the part e. f), Transient PL decays of 20-nm-thick x% Pd3O8-P: mCBP films measured at 580 nm at room temperature.

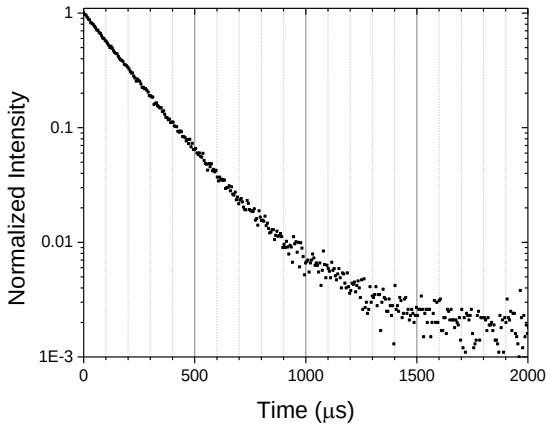

Figure 3.8 Transient PL decay of a dilute solution of Pd3O8-P in 2-MeTHF at 77 K measured at 461 nm.

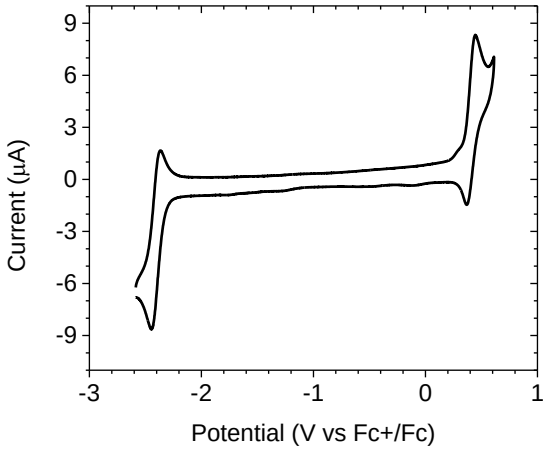

Figure 3.9 Cyclic voltammogram for Pd3O8-P.

To investigate the photophysical properties of Pd3O8-P aggregates in solid state, four thin films were prepared by doping Pd3O8-P into 3,3'-di(9H-carbazol-9-yl)biphenyl (mCBP) with dopant concentrations of 6%, 20%, 50%, and 100%. The room temperature

and 77 K emission spectra are shown in Figure 3.7b-e. At a low doping concentration (6%), the Pd3O8-P film at 77 K showed a mixture of the monomer emission coinciding with the emission peaks of the dilute solution sample and a broad emission band between 500 and 650 nm which could be attributed to an aggregate emission. At room temperature, the aggregate emission became more pronounced indicating these aggregate emissive species are thermally accessed. This temperature dependence may be the result of a diffusion process or could indicate that a thermal reorganization is required to access a favourable packing for the aggregate emission to occur. As the doping concentration increased to 20%, the relative contribution from the monomer was significantly reduced at 77 K giving a broad emission spectrum peaking at 570 nm, and the monomer emission was nearly absent at room temperature. Further increases to 50% and 100% dopant concentration of Pd3O8-P led to broad and featureless emission spectra even at 77 K, peaking at 578 and 583 nm respectively corresponding to exclusive aggregate emission. Additionally, the absorption spectrum of neat Pd3O8-P film is shown in Figure 3.7e, which exhibited very similar absorption patterns as that of Pd3O8-P in solution except for the observation of the weak and broad absorbance in the range of 420-520 nm due to the formation of Pd3O8-P aggregates in the solid film. Furthermore, the crystallinity of the Pd3O8-P in thin film was investigated by powder X-ray diffraction (XRD) on neat Pd3O8-P film and sublimed Pd3O8-P crystalline solid (Figure 3.10). The XRD pattern of sublimed Pd3O8-P solid showed a sharp peak at 8.46°, whereas the neat Pd3O8-P film, showed a weak and broadened peak suggesting the vapor deposited film is primarily amorphous.

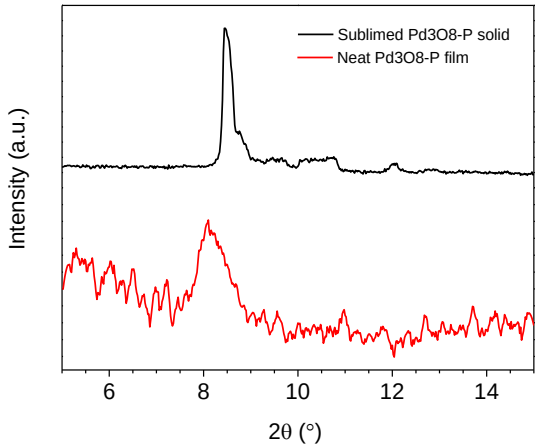

Figure 3.10 Powder X-ray diffraction patterns of neat 30 nm Pd3O8-P film and sublimed Pd3O8-P solid.

The transient PL decays of these four films were measured at 580 nm at room temperature as shown in Figure 3.7f and summarized in Table 3.1. The 6% doped film showed a bi-exponential decay of 2.80 μs (weighting: 26%) + 27.18 μs (74%), which is expected for an emission spectrum comprising both monomer and aggregate species in the 6% doped Pd3O8-P film. The 20% and 50% doped films exhibited dramatically shorter decays but were still best fitted to bi-exponential decays of 1.83 μs (53%) + 9.60 μs (47%) and 1.10 μs (63%) + 3.58 μs (37%) respectively, albeit with faster and less significant long components. Lastly, the neat Pd3O8-P film demonstrated a mono-exponential emission decay with a transient lifetime of 0.62 μs. Furthermore, PLQY values of 6%, 20%, 50%, and 100% Pd3O8-P doped films were measured to be 73±10, 76±10, 87±10, and 86±10% respectively. The radiative decay rate of Pd3O8-P aggregates in neat film was determined to be 1.4×10^{-6} s^{-1}, which is 200 times higher than that of Pd3O8-P monomer, which was estimated to be 5.6×10^{-3} s^{-1} based on a τ of 179 μs and a presumptive unity PLQY for a dilute Pd3O8-P solution at 77K.

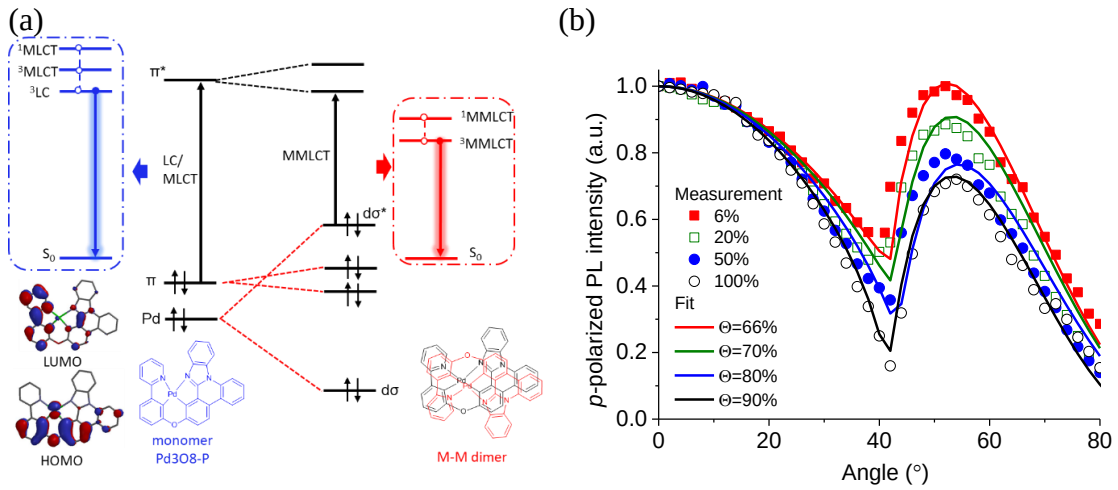

Figure 3.11 Qualitative molecular orbital schemes for Pd3O8-P and its aggregate, and analysis of horizontal emitting dipole orientation ratios for Pd3O8-P aggregates. a), Simplified molecular orbital and schematic energy level diagrams for phosphorescent emitter Pd3O8-P featuring monomer and metal-metal dimer emissions. b), Experimentally obtained angle-dependent PL intensities of the p-polarized light of 20-nm-thick x% Pd3O8-P: mCBP films at 580 nm (symbols). Solid lines represent theoretical fits to the experimental data.

To explain the photophysical properties of Pd3O8-P doped films, it is instructive to consider the energetic landscape of the monomer and potential metal-metal (M-M) dimer species of Pd3O8-P, as illustrated in Figure 3.11a. Due to their excellent molecular planarity, Pd3O8-P molecules have the tendency to form facially packed aggregates with Pd-Pd interaction and/or ππ stacking that can generate red-shifted aggregate emission. The extent of metal-metal interaction and/or ππ stacking are closely related to the intermolecular distance.[53, 88, 89] When emitters are lightly doped into the host, emission from an isolated Pd3O8-P monomer will be dominant, owing to the extended intermolecular distance and low probability of forming co-facial pairs. As is the case with many other Pd(II) complexes, the emission from isolated Pd3O8-P monomers is characterized by a long-lived (179 μs) and highly vibronic featured emission spectrum suggesting a localized ligand-centred excited state. This is in contrast to Pt(II) complexes

which have varying admixtures of ^{3}LC and ^{3}MLCT character and are routinely reported to have emission decay lifetime on the order of a few microseconds.[5] The slower radiative decay process for Pd3O8-P can be partially attributed to more stabilized Pd(II) d-orbitals and less metal ion involvement in the frontier orbitals compared to Pt analogs.[56, 85, 90]

Table 3.1 Photophysical properties of the 20-nm-thick x% Pd3O8-P: mCBP films.

x% Pd3O8-P: mCBP films	λ_{max} (nm)	τ (μs)	Φ_{PL} (%)	Θ (%)	λ_{max} (nm) @ 77 K
6%	542	2.80 (weighting: 26%) 27.18 (74%)	73±10	66	470
20%	550	1.83 (53%) 9.60 (47%)	76±10	70	570
50%	568	1.10 (63%) 3.58 (37%)	87±10	80	578
100%	580	0.62	86±10	90	583

As the doping concentration increases, the Pd3O8-P molecules are more likely to be nearest neighbours and their planar molecular geometry allows efficient face-to-face intermolecular interactions. For particular orientations and intermolecular spacings, a strong interaction is expected between the Pd d-orbitals in adjacent molecules which will lead to the formation of Pd-Pd bonding (dσ) and antibonding (dσ*) orbitals. If a strong interaction exists, the Pd-Pd dσ* will be destabilized above the ligand π orbitals and the highest occupied molecular orbital (HOMO) will be predominantly localized on the two metal centres. This results in emission dominated by singlet and triplet metal-metal-to-ligand charge transfer (^{1,3}MMLCT) transition that is a charge transfer between filled Pd-Pd dσ* and a vacant, ligand-based π* orbital (dσ* $\rightarrow$ π*).[91] This MMLCT transition can explain the broad and red-shifted emission band that becomes increasingly

dominant at higher concentrations of Pd3O8-P doped films.[48] The increased metal character from the MMLCT transitions can significantly reduce the excited state lifetime resulting in a transient decay of 0.62 μs for Pd3O8-P aggregates which is 100 times shorter than the Pd3O8-P monomer emission, and is on par with the fastest Ir or Pt phosphors. The ^{1,3}MMLCT emission from closely spaced dimers of square planar Pt(II) complexes has been previously explored through computational methods where it was demonstrated the formation of dimers that exhibit ^{1,3}MMLCT emission was highly dependent on both orientation and spacing.[92] The amorphous nature of vacuum deposited films makes it challenging to determine the exact orientations and spacing responsible for the emission properties, but the dramatic increase in the radiative decay rate suggests that an ^{1,3}MMLCT state is likely involved. A more accurate depiction would require an in-depth computational study of the quantum mechanics of both the monomer and aggregate species and their molecular dynamics inside these films, which are beyond the scope of the present work.

To determine whether the Pd3O8-P aggregates exhibit predominant horizontal emitting dipoles for potential optical outcoupling enhancement,[68] the horizontal emitting dipole ratio (Θ) for the doped thin films were measured by analysing the angle-dependent p-polarized PL spectra (Figure 3.11b) at 580 nm, where Θ was defined as the ratio of the horizontal emitting dipoles to the total emitting dipoles. The Θ values of Pd3O8-P aggregates in 6%, 20%, 50% and 100% Pd3O8-P: mCBP films were determined to be 66%, 70%, 80% and 90% respectively, indicating that Pd3O8-P aggregates exhibited more preferential horizontal emitting dipole orientation in the pure solid film. Thus, the combination of a close to unity PLQY, and a high Θ of 90%

observed in the pure Pd3O8-P film make Pd3O8-P aggregates an ideal emitter candidate for efficient OLED fabrication.

To evaluate the electroluminescent properties and operational stability of Pd3O8-P aggregates in the device settings, four devices were fabricated and tested with a general structure of ITO (100 nm)/ HATCN (10 nm)/ NPD (70 nm)/ TrisPCz (10 nm)/ x% Pd3O8-P:mCBP (20 nm)/ BAlq (10 nm)/ BPyTP (50nm)/ LiF (1 nm)/ Al (100 nm), where x is 6, 20, 50 and 100 for Devices 1-4 with various Pd3O8-P concentrations.

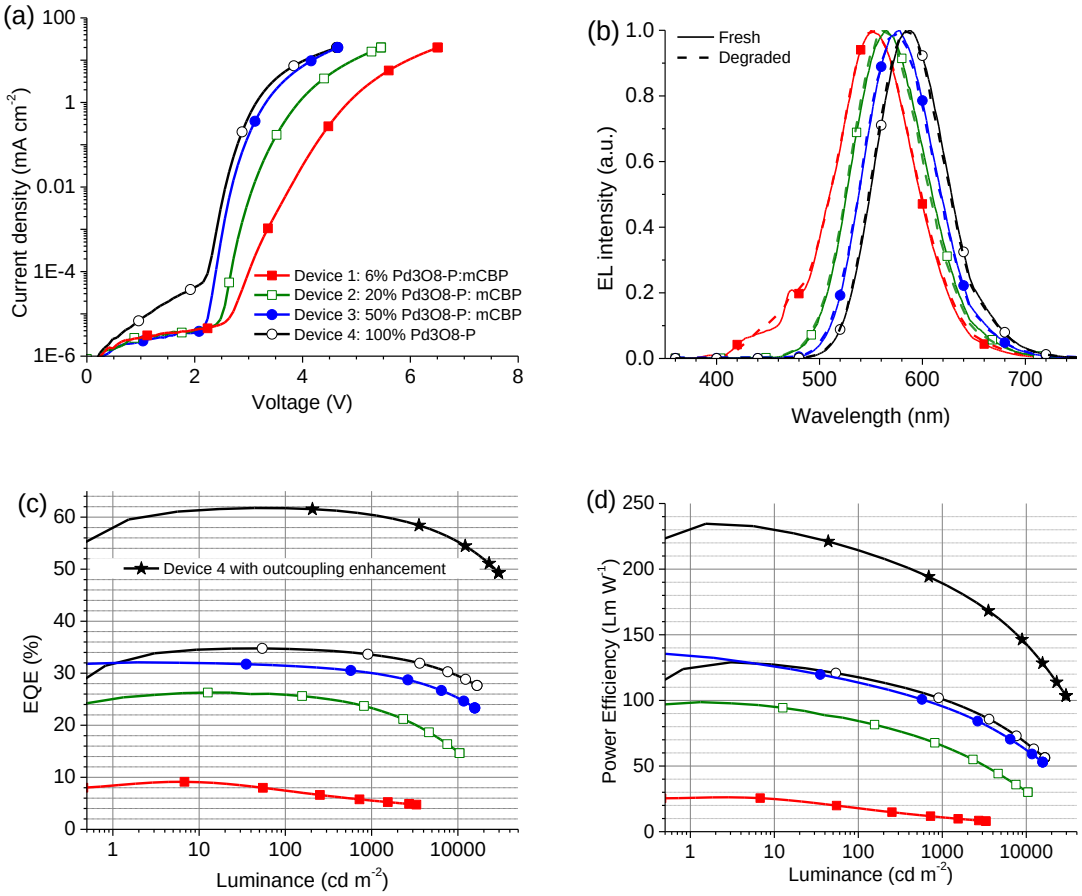

Figure 3.12 Performance of OLEDs. a)-d), Current density–voltage characteristics (a), electroluminescent (EL) spectra before lifetime testing (solid lines) and after LT_{95} testing (dashed lines) (b), EQE (c), and power efficiency (PE) (d) versus luminance for Devices 1-4 in the general structure ITO/ HATCN (10 nm)/ NPD (70 nm)/ TrisPCz (10 nm)/ x% Pd3O8-P: mCBP (20 nm)/ BAlq (10 nm)/ BPyTP (50 nm)/ LiF (1 nm)/ Al (100 nm).

Device 1 (solid squares): 6%; Device 2 (open squares): 20%; Device 3 (solid circles): 50%; Device 4 (open circles): 100%. EQE and PE versus luminance of Device 4 with outcoupling enhancement (solid stars) by applying index matching gel between silicon photodiode and glass substrate.

Figure 3.12a illustrates the current density-voltage characteristics of Devices 1-4. Both the turn-on voltages and the driving voltages for Device 1-4 decreased with the increase of dopant concentrations. The voltages at 1mA cm^{-2} were 4.85, 3.93, 3.32 and 3.15 V for Devices 1-4 respectively. Such changes indicated potential improvement of both charge injection to the EML and charge transport inside the EML. The electroluminescent (EL) spectra of these four devices are shown in Figure 3.12b with CIE coordinates of (0.37, 0.53), (0.44, 0.54), (0.48, 0.51), and (0.52, 0.47), respectively. Devices 2-4 all exhibited exclusive Pd3O8-P aggregate emissions, whereas Device 1 showed a broad EL spectrum ranging from 400-720 nm with the majority emission components originated from both monomers and aggregates. The observation of the non-exclusive emission ranging from 400 to 450 nm in Device 1 is likely attributed to poor charge confinement by adopting moderate blocking materials like TrisPCz and BAlq with the goal of fabricating potential stable devices.[56] In comparison to observed PL spectra of the corresponding doped films, aggregate emission peaks in the EL spectra of Devices 1-4, i.e. ranging from 550-588 nm, were all red-shifted. Such discrepancies can be attributed to the effect of optical cavity device settings on the EL spectra measured at the forward direction. For example, the light distribution pattern analysis of Device 4 (Figure 3.13) indicated a slightly detuned cavity device structure. Additionally, the ratio of aggregate/monomer emission was observed to be increased significantly in comparison to its PL spectra. The enhanced aggregate emission can be the result of potential direct charge trapping on Pd3O8-P aggregates during electrical pumping.[54] It is worth

mentioning that the EL spectra of 5% degraded Devices 1-4 showed negligible changes relative to those of fresh devices, suggesting a similar degradation rate for both Pd3O8-P monomers and aggregates.

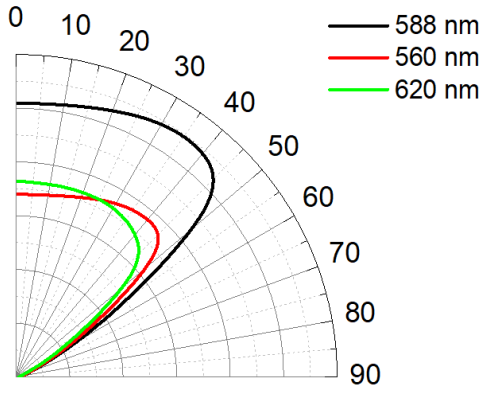

Figure 3.13 Emission patterns for host-free Pd3O8-P Device 4 at 560, 588, and 620 nm.

The plots of EQE versus luminance for Devices 1-4 are shown in Figure 3.12c. As the dopant concentration increased, the EQEs were greatly improved, and the host-free OLED (Device 4) achieved an EQE of 34.8% without any out-coupling enhancement, which, to the authors' knowledge, is the highest reported device efficiency based on a Pd(II) complex.[56, 93] The achievement of such record-breaking EQE is mainly attributed to the close to unity PLQY and the predominant horizontal emitting dipoles of Pd3O8-P aggregates. In addition, Device 4 also exhibited a very reduced efficiency roll-off, retaining high EQEs of 33.5% at 1000 cd cm^{-2} and 29.5% at 10000 cd cm^{-2}. Due to an amazingly short τ of 0.62 μs for Pd3O8-P aggregates, TTA, TPQ and other quenching processes inside the EML were effectively suppressed. Furthermore, potential large spacing among discrete excited Pd3O8-P aggregates may also play a crucial role in further reducing the possibility of TTA and TPQ processes.

By applying an index matching gel between silicon photodiode and the OLED glass substrate without an air gap,[12, 94] the remeasured external quantum efficiency of Device 4 reached 61.7%, which consists of both air mode and substrate mode device efficiencies. It is worthy of mentioning that the high substrate mode quantum efficiency of 26.9% supported that phosphorescent emitters with predominant horizontal emitting dipoles could not only produce more photons in the air mode but also generate more photons trapped in the substrate mode, which can be easily harvested by cost-effective external light extraction techniques. As a result, a simple OLED device with a potential EQE of over 60% has been demonstrated, which cannot be previously accomplished without expensive and un-manufacturable light extraction technologies like photonic crystals, substrates with low-index grids, or substrates with corrugated surface.[12, 95, 96, 14] Moreover, Device 4 exhibited a maximum power efficiency (PE) of over 230 lm W^{-1}, and maintained a high PE of 189 lm W^{-1} at 1000 cd m^{-2} due to a high EQE of 60.4% and a low driving voltage of 3.14 V. Such a high efficacy amber light panel (blue light free) can already make a strong impact on the development of specialized lighting products for medical and automobile applications, indicating a great potential of utilizing phosphorescent molecular aggregates for lighting applications.

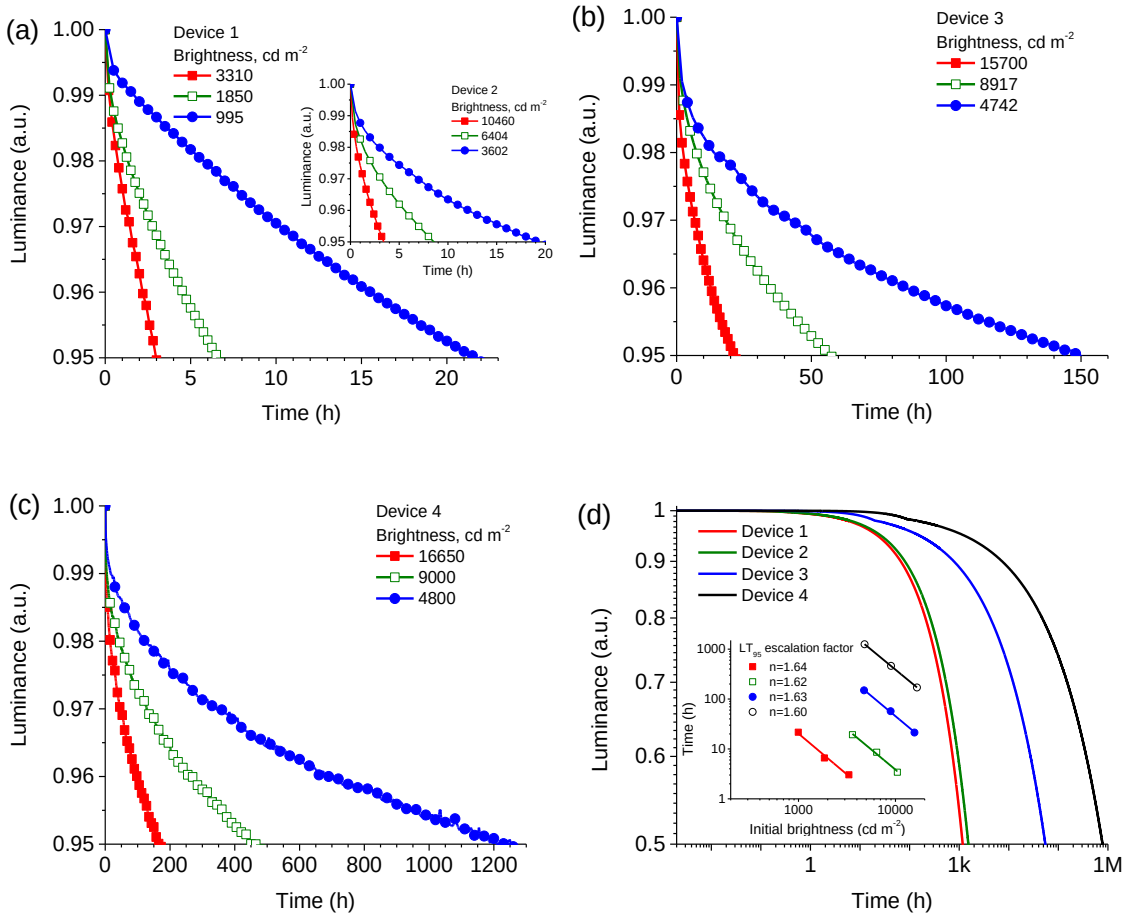

Figure 3.14 Operational stability of OLEDs. a)-c), Plots of relative luminance versus operation time at constant current densities of 20 (solid squares), 10 (open squares), and 5 mA cm^{-2} (solid circles) for Devices 1-4. d), Extrapolated LT_{50} of Devices 1-4 at constant current density of 5 mA cm^{-2} by using equation $L/L_0 = \exp[-(t/\varepsilon)^{\beta}]$. Inset shows the plots of LT_{95} lifetime vs initial brightness (L_0) for Devices 1-4 together with the fit using the formula $LT_{95}L_0^{n}$ = constant.

Table 3.2 Summary of device performance data.

Device	1	2	3	4	4[c]
Dopant Conc. (%)	6	20	50	100	100
λ_{max} (nm)	550	564	578	588	588
CIE coordinates	(0.37, 0.53)	(0.44, 0.54)	(0.48, 0.51)	(0.52, 0.47)	(0.52, 0.47)
Peak EQE (%)	9.1	26.3	32.1	34.8	61.7
EQE @ 1000 cd m^{-2}	5.5	23.5	30.0	33.5	60.4
EQE @ 10000 cd m^{-2}	--	14.8	25.4	29.5	55.2
Peak PE (lm W^{-1})	26	99	135	129	235
PE (lm W^{-1}) @ 1000 cd m^{-2}	11	66	95	101	189
PE (lm W^{-1}) @ 10000 cd m^{-2}	--	31	62	68	143
L_0 (cd m^{-2})	3310	10460	15700	16650	29687
LT_{95} (h) @ L_0	3.0	3.4	21.3	170.7	170.7
LT_{95} (h)[a] @ 1000 cd m^{-2}	21	152	1900	15400	38800
LT_{50} (h)[b] @ 1000 cd m^{-2}	1.15×10^3	1.22×10^4	6.91×10^5	9.59×10^6	--

[a] Estimated from the equation $LT(L_1) = LT(L_0)(L_0/L_1)^n$, where n is from the experimental data, i.e., n=1.64, 1.62, 1.63, 1.60 for Devices 1-4, respectively; [b] Extrapolated operational lifetime by fitting experimental curves of Devices 1-4 at 5 mA cm^{-2} using equation $L/L_0 = \exp[-(t/\varepsilon)^{\beta}]$; [c] Device 4 is remeasured with out-coupling enhancement by attaching an index matching gel coated photodiode to the glass substrate.

The device operational stabilities of Devices 1-4 were also examined. Figure 3.14a-c show the normalized electroluminescent intensity versus operational time for Devices 1-4 at constant driving current densities of 20, 10 and 5 mA cm^{-2}. All the key device performance data are summarized in Table 3.2. Given that the display industry is trying to minimize the image sticking effect as well as differential aging effect on the displays, LT_{95} lifetimes were chosen as metrics and experimentally determined.[97] At a constant driving current density of 20 mA cm^{-2}, the LT_{95} values of Devices 1-4 were 3.0, 3.4, 21.3, and 170.7 h with initial luminance (L_0) of 3310, 10460, 15700, and 16650 cd m^{-2} respectively, indicating the operational stabilities were greatly improved as dopant concentrations increased. Lifetime (LT) at different luminance values can be estimated

using the formula $LT(L_1) = LT(L_0)(L_0/L_1)^n$, where L_1 is the desired luminance, and n is the escalation factor.[24] As shown in the inset of Figure 3.14d, n values for Devices 1-4 were determined by fitting the formula $LT_{95}L_0^n$= constant with LT_{95} at 20, 10, and 5 mA cm^{-2} and the corresponding L_0, and obtained the values of 1.64, 1.62, 1.63, and 1.60 respectively.[98, 99] The LT_{95} at 1000 cd m^{-2} for Device 4 is estimated to be 15400 h. Such superior operational stability is consistent with the reversible oxidation and reduction behaviour of Pd3O8-P in solution (Figure 3.9), a short τ of 0.62 μs for Pd3O8-P aggregates, and the potentially large spacing among the discrete excitonic aggregates, which could suppress TTA, TPQ and other degradation pathways. Moreover, the half-lifetime LT_{50} was also extrapolated by using an empirical method based on the stretched exponential decay equation $L/L_0 = \exp[-(t/\varepsilon)^{\beta}]$,[13, 98] where ε and β are phenomenological parameters. Figure 3.14d shows the extrapolated LT_{50} lifetimes of Devices 1-4 based on the plots of measured EL intensity versus time at a constant current density of 5 mA cm^{-2}. The LT_{50} of Device 4 was fitted to be 7.8×10^5 h with initial brightness of 4800 cd m^{-2}, and estimated to be 9.59×10^6 h at 1000 cd m^{-2}, which is ten times better than the state-of-the-art iridium-based yellow OLED device in a more sophisticated device structure.[100] To the authors' best knowledge, Device 4 is the most stable reported OLED among all of the emissive materials on the public domain.[33, 56, 79, 100–102] In summary, the extraordinary performance of Pd3O8-P devices with high EQE and superior operational stability demonstrates the utility of phosphorescent molecular aggregates as emitters for display and lighting applications. Pd3O8-P based devices can be further optimized with utilization of the state-of-the-art charge transporting and charge blocking materials.

3.1.4 Conclusion

It has been demonstrated that phosphorescent molecular aggregates can realize efficient and stable OLEDs with largely reduced efficiency roll-off. In the host-free environment, Pd3O8-P aggregates demonstrated a 100-fold reduction in luminescent lifetime with a τ of 0.62 μs relative to its monomer form, a close to unity PLQY, and predominant horizontal emitting dipoles at room temperature. Additionally, a host-free Pd3O8-P device showed a peak EQE of 34.8% with an emission peak of 588 nm and an emission half bandwidth of 84 nm, maintained very high EQEs of 33.5% at 1000 cd m^{-2} and 29.5% at 10000 cd m^{-2}, and exhibited an estimated LT_{50} lifetime of 9.59 million hours at 1000 cd m^{-2}. The outstanding device performance indicated phosphorescent molecular aggregates can be a feasible emitter candidate for lighting and display applications. The remarkable electrochemical stability of Pd3O8-P demonstrated in the device settings, coupled with the fact that Pd3O8-P has a triplet in the blue emitting region, provides some promise the tetradentate complex design may assist the development of efficient and long-lived blue OLEDs in the future.

3.2 Efficient and Stable Molecular Aggregate Based Organic Light-Emitting Diodes with Judicious Ligand Design

3.2.1 Background

Organic light-emitting diode (OLED) technology has been widely adopted in the mobile displays and TV applications, and is becoming one of potential candidates for next generation solid-state lighting products due to its high electron to photon conversion efficiency and compatibility with flexible substrate, which generates a great deal of interests within the academic and industrial communities.[103, 20, 16, 28, 4, 5, 72]

Driven by the technological needs for high-resolution mobile displays and more cost-effective lighting products, further development of efficient and stable OLEDs operating at high brightness will be highly desired.[73, 104, 30] However, such OLEDs with high brightness tend to suffer a sharp decline in efficiency (known as an efficiency roll-off) and experience an expedited degradation process due to possible triplet-triplet annihilation (TTA) and triplet-polaron quenching (TPQ) processes.[30, 33, 74, 75] More materials and device development efforts will be needed to overcome such technical challenges and expedite the commercialization of OLEDs for display and lighting applications.

In contrast to the conventional approaches of adopting a co-host structure for a moderately doped emissive layer to operate high-brightness OLED,[78, 105] phosphorescent molecular aggregate based OLED also demonstrated a great promise.[40, 50, 84, 67, 23, 49] An OLED device employing a polycrystalline film of Pt(II) bis[3-(tri-fluoro-methyl)-5-(2-pyridyl)-pyrazolate], i.e. $Pt(fppz)_2$, exhibited a high peak external quantum efficiency (EQE) of 38.8% on a bare glass substrate.[49] Moreover, the OLED utilizing an amorphous film of a tetradentate Pd(II) complex, i.e. Pd(II) 7-(3-(pyridine-2-yl-κN)phenoxy-κC)(benzo[4,5]imidazo-κN)([1,2-f]phenanthridine-κC) (Pd3O8-P), can realize a peak EQE of 34.8%, retain an EQE of 33.5% and demonstrate an estimated LT_{95} (time to 95% of the initial luminance) lifetime of 15391 hours at 1000 cd m^{-2}. Such excellent device performance indicated that phosphorescent molecular aggregate can be one of feasible emitter candidates for future display and lighting applications. The nature of amorphous emissive layer will ensure the success of producing uniform self-illuminating devices through the large-scale manufacturing process, while there is a

limited knowledge of key factors for such emissive materials to achieve a high photoluminescent quantum efficiency and exhibit a preferred horizontal emitting dipole orientation at their aggregate form.[68, 69, 92, 106–108] Thus, further progress of molecular aggregate based OLED hinges on the continued development of new emissive materials and the optimization of their materials deign principle.

In the second part of this chapter, the electrochemical and photophysical properties of four Pd(II) complexes including two new derivatives of Pd3O8-P, i.e. Pd(II) 7-(3-(pyridine-2-yl-κN)phenoxy-κC)(benzo-κC)([c]benzo[4,5]imidazo-κN)[1,2-a][1,8]naphthyridine (Pd3O8-Py2) and Pd(II) 7-(3-(pyridine-2-yl-κN)phenoxy-κC)(benzo-κC)([c]benzo[4,5]imidazo-κN)[1,2-a][1,5]naphthyridine (Pd3O8-Py5), were examined. Their chemical structures are shown in the inset of Figure 3.19. This study indicated that the slight structural changes can modify the hole and electron transporting capabilities and alter the horizontal emitting dipole ratios of aggregates in the thin film, and the latter of which were also sensitive to the thin film deposition conditions including the deposition rate and the choice of the templating layer. By optimizing thin film deposition conditions, a Pd3O8-Py5 based OLED device achieved a peak EQE of 37.3%, retained high EQEs of 36.0% and 32.5% at 1000 and 10000 cd m^{-2} respectively. Such device also demonstrated an outstanding operational stability with a measured LT_{95} lifetime of 504 h at the brightness of 17304 cd m^{-2} corresponding to an estimated LT_{95} lifetime of 48246 h at 1000 cd m^{-2}.

3.2.2 Experimental Section

Materials and regents: All commercial reagents were purchased and used as received without further purification. CuI and picolinic acid were purchased from Sigma

Aldrich. K_3PO_4 were purchased from Alfa Aesar. Silica gel (40-60μm) was purchased from Agela Technologies and BDH. Solvent DMSO was purchased from Alfa Aesar. The reaction was carried out under an inert N_2 atmosphere in oven-dried glassware. External bath temperatures were used to record all reaction temperatures.

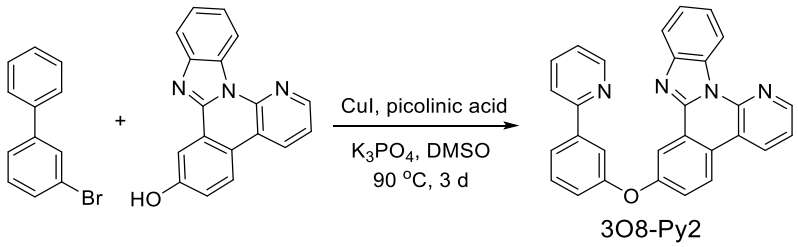

Figure 3.15 Synthesis of ligand 3O8-Py2.

Figure 3.15 shows the synthetic method of ligand 3O8-Py2. To a three-necked flask equipped with a magnetic stir bar, added benzo[c]benzo[4,5]imidazo[1,2-a][1,8]naphthyridin-7-ol (0.50 g, 1.75 mmol, 1 eq), 2-(3-bromophenyl)pyridine (0.49 g, 2.10 mmol, 1.2 eq), picolinic acid (0.043 g, 0.35 mmol, 0.2 eq), K_3PO_4 (0.74 g, 3.50 mmol, 2.0 eq), and CuI (0.067 g, 0.35 mmol, 0.2 eq). Then the flask underwent the procedure of the evacuation and backfill with nitrogen for three times. Solvent of DMSO (20 mL) was added under the protection of nitrogen. Then the mixture was stirred in an oil bath at 100 ℃ for 3 days, then cooled down to ambient temperature. The solid was filtered off and washed with ethyl acetate. The filtrate was concentrated under reduced pressure. Then the residue was purified through column chromatography on silica gel using dichloromethane/ethyl acetate as eluent to obtain the desired product 3O8-Py2 as a light orange solid (0.53 g, yield: 68%). ^{1}H NMR (DMSO-d_6, 400 MHz, δ): 9.17(d, J = 8.6 Hz, 1H), 8.99 (d, J = 9.2 Hz, 1H), 8.85 (d, J = 4.7 Hz, 1H), 8.68-8.61 (m, 2H), 8.09-8.04

(m, 3H), 7.99 (s, 1H), 7.96-7.86 (m, 2H), 7.83-7.76 (m, 1H), 7.70-7.64 (m, 2H), 7.56-7.48 (m, 2H), 7.40-7.35 (m, 2H).

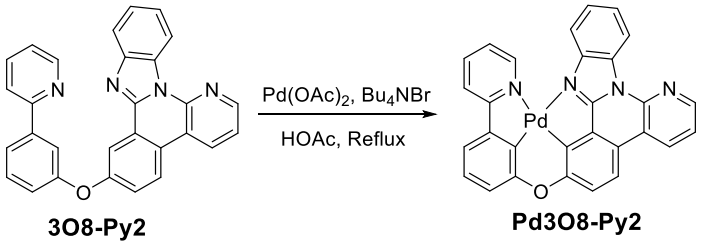

Figure 3.16 Synthesis of Pd3O8-Py2.

The synthetic route of Pd3O8-Py2 is presented in Figure 3.16. To a three-necked flask equipped with a magnetic stir bar, added ligand 3O8-Py2 (0.50 g, 1.14 mmol, 1 eq), $Pd(OAc)_2$ (0.28 g, 1.25 mmol, 1.1 eq), and Bu_4NBr (0.040 g, 0.11 mmol, 0.1 eq). Then the flask underwent the procedure of the evacuation and backfill with nitrogen for three times. Solvent of HOAc (70 mL) was added under the protection of nitrogen. Then the mixture was stirred in an oil bath under reflux for 3 days, then cooled down to ambient temperature. The mixture was concentrated under reduced pressure. Then the residue was purified through column chromatography on Al_2O_3 using dichloromethane as eluent to obtain the desired product Pd3O8-Py2 as a light yellow solid (0.32 g, yield: 51%). The product (0.32 g) was further purified by sublimation in a four-zone thermal-gradient furnace under high vacuum to obtain yellow crystal (0.25 g, yield: 78%). ^{1}H NMR (DMSO-*d6*, 400 MHz, δ): 9.36-9.32 (m, 1H), 9.27 (d, *J* = 8.4 Hz, 1H), 8.92 (d, *J* = 4.3 Hz, 1H), 8.81 (d, *J* = 8.4 Hz, 1H), 8.57 (d, *J* = 9.0 Hz, 1H), 8.33 (d, *J* = 7.6 Hz, 1H), 8.26 (d, *J* = 8.1 Hz, 1H), 8.20-8.13 (m, 1H), 7.86-7.79 (m, 2H), 7.76-7.69 (m, 2H), 7.67-7.59 (m, 2H), 7.35 (t, *J* = 7.0 Hz, 1H), 7.28 (d, *J* = 7.5 Hz, 1H).

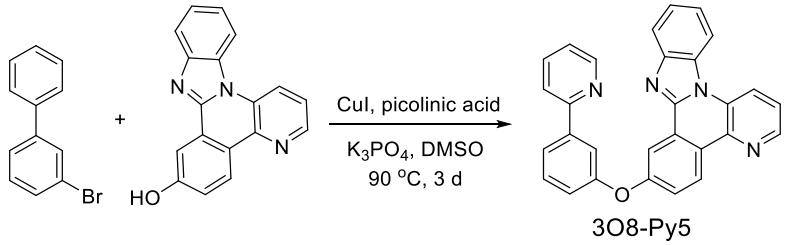

Figure 3.17 Synthesis of ligand 3O8-Py5.

The synthetic route of ligand 3O8-Py5 is shown in Figure 3.17. To a three-necked flask equipped with a magnetic stir bar, added benzo[c]benzo[4,5]imidazo[1,2-a][1,5]naphthyridin-7-ol (1.20 g, 4.23 mmol, 1 eq), 2-(3-bromophenyl)pyridine (1.18 g, 5.07 mmol, 1.2 eq), picolinic acid (0.11 g, 0.85 mmol, 0.2 eq), K_3PO_4 (1.80 g, 8.50 mmol, 2.0 eq), and CuI (0.16 g, 0.85 mmol, 0.2 eq). Then the flask underwent the procedure of the evacuation and backfill with nitrogen for three times. Solvent of DMSO (40 mL) was added under the protection of nitrogen. Then the mixture was stirred in an oil bath at 100 ℃ for 3 days, then cooled down to ambient temperature. The solid was filtered off and washed with ethyl acetate. The filtrate was concentrated under reduced pressure. Then the residue was purified through column chromatography on silica gel using dichloromethane/ethyl acetate as eluent to obtain the desired product 3O8-Py5 as a light orange solid (1.30 g, yield: 70%). ^{1}H NMR (DMSO-d_6, 400 MHz, δ): 9.13 (d, J = 7.8 Hz, 1H), 9.10-9.05(m, 1H), 8.84 (d, J = 4.2 Hz, 1H), 8.79 (d, J = 9.0 Hz, 1H), 8.64 (d, J = 4.8 Hz, 1H), 8.10-8.03 (m, 3H), 7.98 (s, 1H), 7.93-7.86 (m, 2H), 7.71-7.63 (m, 3H), 7.52-7.46 (m, 2H), 7.40-7.34 (m, 2H).

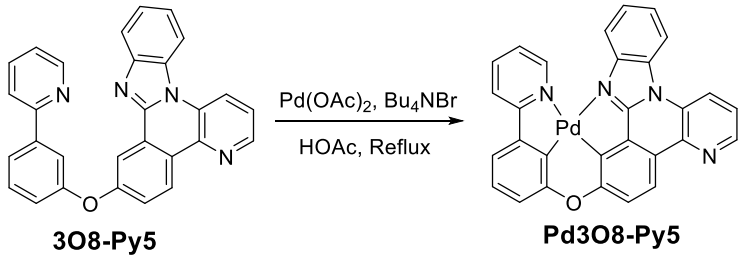

Figure 3.18 Synthesis of Pd3O8-Py5.

Figure 3.18 depicts the synthetic method of Pd3O8-Py5. To a three-necked flask equipped with a magnetic stir bar, added ligand 3O8-Py5 (0.72 g, 1.64 mmol, 1 eq), $Pd(OAc)_2$ (0.41 g, 1.81 mmol, 1.1 eq), and Bu_4NBr (0.052 g, 0.16 mmol, 0.1 eq). Then the flask underwent the procedure of the evacuation and backfill with nitrogen for three times. Solvent of HOAc (100 mL) was added under the protection of nitrogen. Then the mixture was stirred in an oil bath under reflux for 3 days, then cooled down to ambient temperature. The mixture was concentrated under reduced pressure. Then the residue was purified through column chromatography on Al_2O_3 using dichloromethane as eluent to obtain the desired product Pd3O8-Py5 as a light yellow solid (0.68 g, yeild: 76%). The product (0.68 g) was further purified by sublimation in a four-zone thermal-gradient furnace under high vacuum to obtain yellow crystal (0.49 g, yield:72%). ^{1}H NMR (DMSO-*d6*, 400 MHz, δ): 9.26-9.19 (m, 1H), 9.11 (d, *J* = 8.4 Hz, 1H), 9.04 (d, *J* = 7.6 Hz, 1H), 8.83 (d, *J* = 4.1 Hz, 1H), 8.31 (d, *J* = 8.8 Hz, 1H), 8.24 (d, *J* = 8.3 Hz, 1H), 8.16-8.07 (m, 2H), 7.79-7.61 (m, 4H), 7.57 (t, *J* = 7.5 Hz, 1H), 7.47 (d, *J* = 8.3 Hz, 1H), 7.30 (t, *J* = 7.6 Hz, 1H), 7.20 (d, *J* = 8.2 Hz, 1H).

3.2.3 Results and Discussion

Pd3O3 has a symmetric tetradentate cyclometalating ligand compromising of a pair of phenyl-pyridine ligand components. It has been well documented that Pd3O3 has

more favorable electron transporting capability, which requires a high-energy electron-blocking material to ensure a strong charge confinement inside of emissive layer and achieve a high device efficiency.[56] Thus, the replacement of one phenyl-pyridine group with benzo[4,5]imidazo[1,2-f]phenanthridine will potentially enhance its hole transporting functionality for Pd3O8-P, which could provide a key role to support efficient and stable device operation in a typical host-free device setting, since Pd(II) complex needs to act as effective hole and electron conductors in addition to generate electroluminescent emission. Furthermore, the addition of the aza atoms on the phenyl ring in the benzo[4,5]imidazo[1,2-f]phenanthridine moiety of Pd3O8-P, e.g. Pd3O8-Py2 and Pd3O8-Py5, will lead to modest changes in their hole and electron transporting functionalities, resulting in a possibly broadened exciton formation zone and potential device performance improvement.

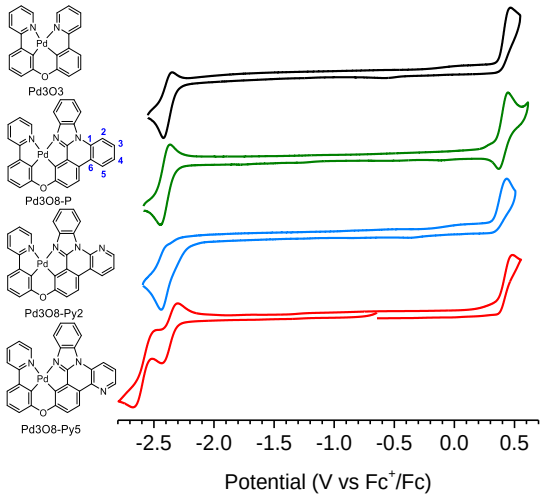

Figure 3.19 Cyclic voltammogram and chemical structures of Pd3O3, Pd3O8-P, Pd3O8-Py2, and Pd3O8-Py5.

The electrochemical properties of these four Pd(II) complexes were examined by performing the cyclic voltammetry in a solution of anhydrous DMF, as shown in Figure

3.19. The oxidation and reduction potentials were determined by differential pulse voltammetry versus an internal ferrocenium/ferrocene (Fc^+/Fc) reference. All four Pd(II) complexes showed similar values in their oxidation (0.40 - 0.42 V) and first reduction potentials (-2.37 - -2.42 V), indicating similar HOMO and LUMO energy levels for all of them, which are presented in Figure 3.19. Pd3O3 exhibited a quasi-reversible reduction peak at -2.40 V and an irreversible oxidation peak at 0.42 V. The reduction process of Pd3O3 mainly occurred at the pyridyl ring of the cyclometalating ligand, and its oxidation is considered a Pd(II)-aryl centered process, which is often irreversible due to the effect of solvent on square planar Pd(II) ions.[109] On the other hand, Pd3O8-P appeared to have a reversible oxidation, indicating a relocation of oxidation site from the Pd(II) center to the phenanthridine fragment of the ligand. For similar reasons, Pd3O8-Py5 exhibited a quasi-reversible oxidation process in addition to two reversible reduction peaks at -2.37 and -2.59 V. It should be noted the second reduction peak of Pd3O8-Py5 can be attributed to the pyridyl group on the benzo[c]benzo[4,5]imidazo[1,2-a][1,5]naphthyridine moiety of the ligand. Moreover, the DFT calculations of these four Pd(II) complexes (Figure 3.20) also suggested that their LUMO was localized largely on the pyridyl orbitals of the phenyl pyridine fragment, and HOMO consisted mainly of a mixture of phenyl-π and Pd-d orbitals, both of which are consistent with the electrochemical analysis. Pd3O8-Py2 demonstrated both irreversible reduction and oxidation processes (Figure 3.19), which can be possibly attributed to its poor solubility in DMF solvent and potential destabilization of the 2-aza atom on Pd3O8-Py2 cations respectively.

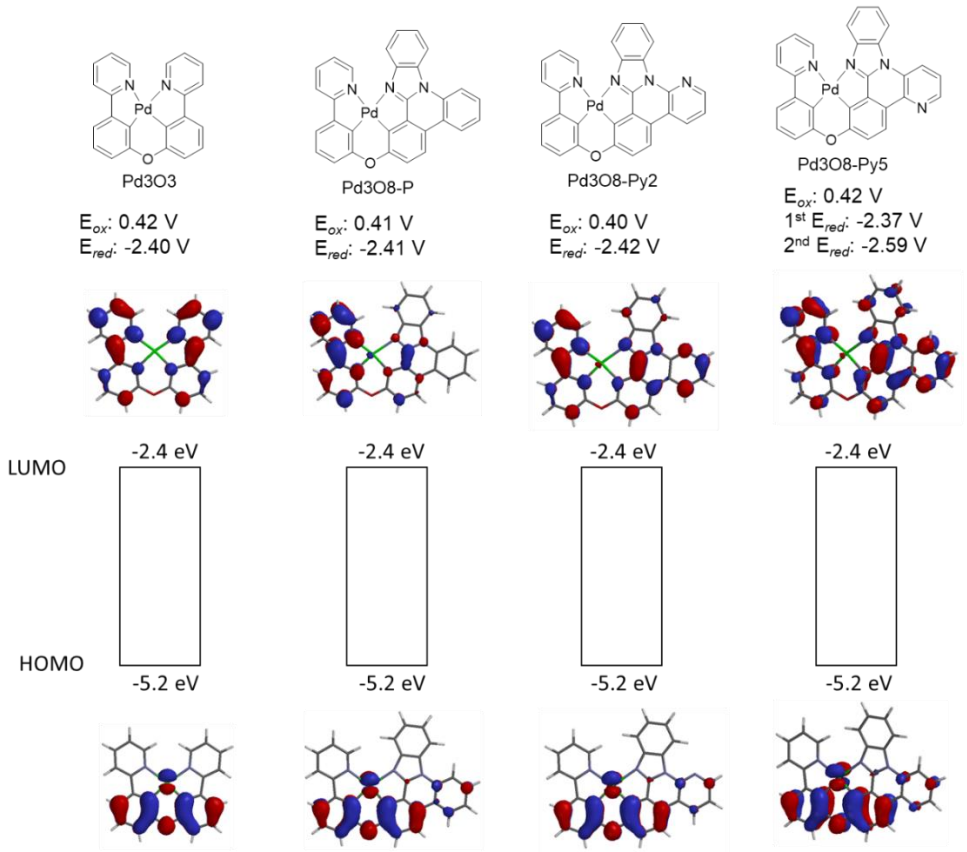

Figure 3.20 Reduction and oxidation peak potentials, corresponding HOMO and LUMO levels, and density functional theory (DFT) calculation of HOMO and LUMO for Pd3O3, Pd3O8-P, Pd3O8-Py2 and Pd3O8-Py5.

The room-temperature absorption spectra in dichloromethane and 77 K photoluminescent spectra in 2-methyltetrahydrofuran of Pd3O3 and Pd3O8-Py5 are shown in Figure 3.21. For both complexes, the distinct strong absorption peaks between 250 and 370 nm (ε = 0.6-6.6×10^4 M^{-1} cm^{-1}) can be assigned to $^1(\pi$-$\pi^*)$ transitions on the cyclometalating ligand. The weak absorption bands between 370 and 440 nm were attributed to metal-to-ligand charge transfer (^{1}MLCT) transitions involving both the cyclometalating ligand and the palladium ion. Pd3O8-Py5 displayed an almost identical absorption pattern to Pd3O8-Py2 and previously reported Pd3O8-P (shown in Figure 3.22). Compared to Pd3O3, Pd3O8-Py5 showed more intensive $^1(\pi$-$\pi^*)$ transitions at a

longer wavelength range owing to its relatively larger conjugated ligand system, and a higher ^{1}MLCT transition energy with a cut-off at 405 nm. As shown in Figure 3.21 and Figure 3.22, all 4 Pd complexes exhibited similar monomer emission peaks between 464-466 nm at 77 K while they showed slightly red-shifted monomer emission spectra peaking between 468-470 nm at room temperature. Thus, their emission spectra with pronounced vibronic features and small rigidochromic shift (i.e. energy difference in their emission peaks at room temperature and 77 K) indicated that their lowest triplet states are predominant ligand centred states (^{3}LC) with minimal MLCT admixtures. At a high concentration, pronounced broad emissions in the range 520-700 nm were observed for all four Pd complexes (Figure 3.22), which were attributed to the phosphorescent molecular aggregate emission.

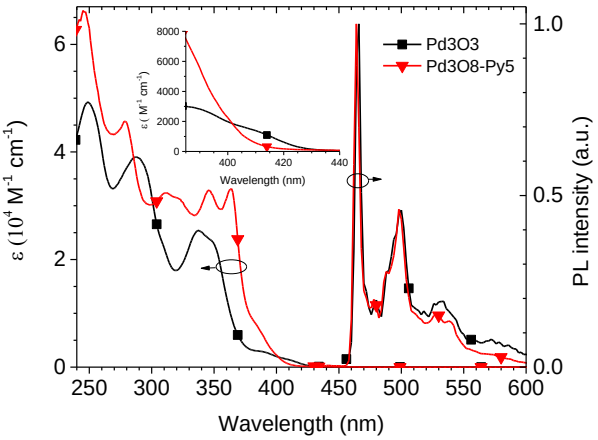

Figure 3.21 Room-temperature absorption and 77 K photoluminescent spectra of Pd3O3 and Pd3O8-Py5.

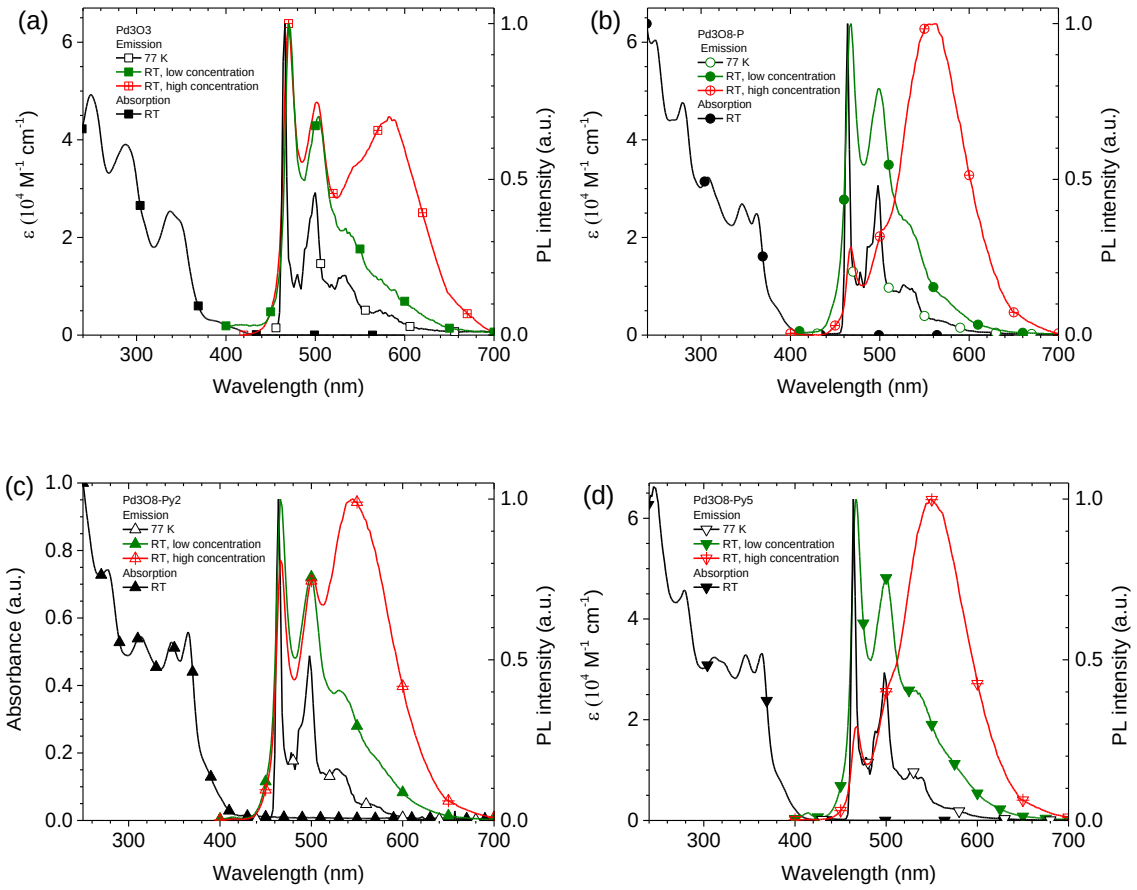

Figure 3.22 Room-temperature absorption, and room-temperature and 77 K photoluminescent spectra of (a) Pd3O3, (b)Pd3O8-P, (c) Pd3O8-Py2 and (d) Pd3O8-Py5.

The PL spectra of 20-nm-thick Pd3O3, Pd3O8-P, Pd3O8-Py2 and Pd3O8-Py5 thin films on TriPCz/quartz substrates are measured and shown in Figure 3.26a. They all exhibited exclusive aggregate emission with similar peak values in the range between 578 and 590 nm with high thin film photoluminescent quantum yield (PLQY) values between 0.79±0.1 and 0.88±0.1. Compared to Pd3O3, films of Pd3O8-P, Pd3O8-Py2 and Pd3O8-Py5 demonstrated narrower emission spectra with full width half maximum (FWHM) of 82-84 nm. The transient PL decays of Pd3O3, Pd3O8-Py2 and Pd3O8-Py5 thin films on glass substrate were measured at 580 nm at room temperature, as shown in Figure 3.23, and demonstrated mono-exponential emission decays with transient lifetimes

of 1.65, 0.70 and 0.67 μs, respectively, similar to previously reported Pd3O8-P film, which indicated that such red-shifted emission is likely originated from the singlet and triplet metal-metal-to-ligand charge transfer (^{1,3}MMLCT) states.[49, 50] It should also be noted that these vapor-deposited Pd3O8-Py2 and Pd3O8-Py5 films showed weak and broadened XRD peak (shown in Figure 3.24) similar to Pd3O8-P film, suggesting majority of amorphous film formed in the vapor deposition process. Additionally, angle-dependent PL intensities of the *p*-polarized light at 580 nm of Pd3O3, Pd3O8-P, Pd3O8-Py2 and Pd3O8-Py5 films on TrisPCz/glass were also measured and illustrated in Figure 3.25. The horizontal emitting dipole ratios (Θ) of their molecular aggregates were determined, and added to Figure 3.26a inset, where Θ is defined as the ratio of the horizontal emitting dipoles to the total emitting dipoles. Compared with symmetric Pd3O3, Pd3O8-P exhibited an improved Θ value to 90%. Further structural modification of Pd3O8-P with additional aza atoms, i.e. Pd3O8-Py5 and Pd3O8-Py2, increased Θ values to 95%, which indicated a predominant horizontal emitting dipole orientation for Pd3O8-Py5 and Pd3O8-Py2 aggregates, making them ideal emissive materials for OLED applications.

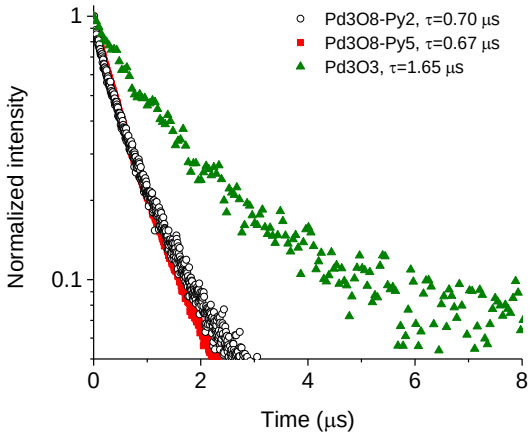

Figure 3.23 Transient PL decays of 20-nm-thick Pd3O3, Pd3O8-Py2 and Pd3O8-Py5 films measured at 580 nm at room temperature.

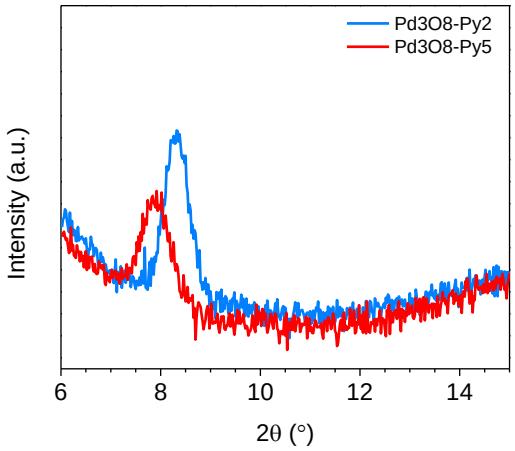

Figure 3.24 Powder X-ray diffraction patterns of neat 30 nm Pd3O8-Py2 and Pd3O8-Py5 films.

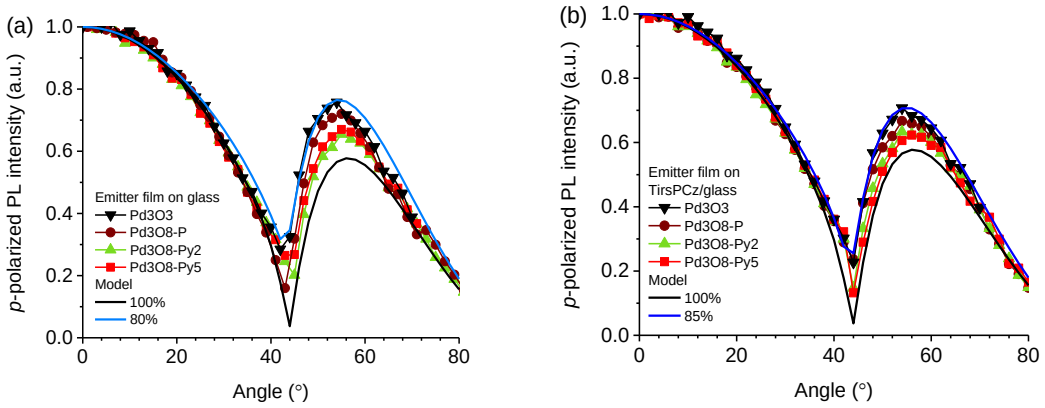

Figure 3.25 Experimentally obtained angle-dependent PL intensities of the *p*-polarized light for 20-nm-thick Pd3O3, Pd3O8-P, Pd3O8-Py2 and Pd3O8-Py5 films with deposition rate of 0.3 Å s^{-1} grown a) on glass substrates and b) on TriPCz/glass.

To evaluate the electroluminescent properties and operational stability of Pd3O3, Pd3O8-P, Pd3O8-Py2 and Pd3O8-Py5 aggregates in device settings, devices were fabricated and tested with a general structure of ITO (100 nm)/ HATCN (10 nm)/ NPD (70 nm)/ TrisPCz (10 nm)/ EML (20 nm)/ BAlq (10 nm)/ BPyTP (50 nm)/ LiF (1 nm)/ Al (100 nm), where EML is Pd3O3, Pd3O8-P, Pd3O8-Py2 and Pd3O8-Py5 film respectively. All their device data are collected and summarized in Table 3.3, and selectively presented in Figure 3.26 and Figure A.2. Due to poor solubility of Pd3O8-Py2 in all general organic solvents, the purity of Pd3O8-Py2 might not be deemed satisfactory even after repeated sublimations, which is considered to be an essential prerequisite to the meaningful device operational stability studies. Thus, the following discussion will focus the analysis on the devices based on Pd3O3, Pd3O8-P and Pd3O8-Py5 in the next sections.

As illustrated in the inset of Figure 3.26b, Pd3O3, Pd3O8-P and Pd3O8-Py5 based devices exhibited similar turn-on voltages (defined as the voltage required to

achieve external brightness of 1 cd m^{-2}) in the range of 2.34 and 2.45 V due to their similar HOMO and LUMO energy levels. However, Pd3O8-P based device demonstrated the highest driving voltage of 4.65 V to reach the current density of 20 mA cm^{-2}, indicating a higher resistance than Pd3O3. The addition of 5-aza atom for Pd3O8-Py5 reduced the device driving voltage to 4.41 V to reach 20 mA cm^{-2} due to a potential improvement in its electron conductivity.

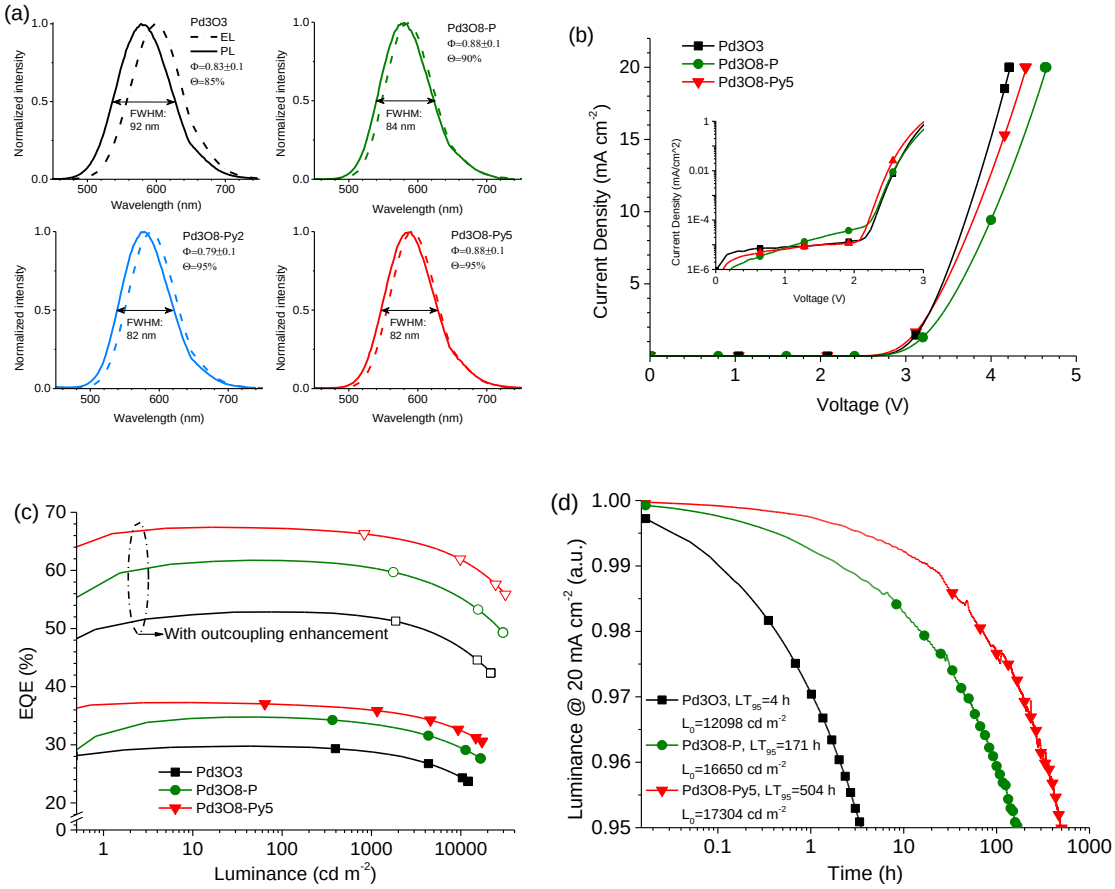

Figure 3.26 a) Photoluminescent spectra of the emitter thin films and electroluminescent spectra of the Pd3O3, Pd3O8-P, Pd3O8-Py2 and Pd3O8-Py5 based devices. b) Current density–voltage characteristics, c) EQE versus luminance, and d) plots of relative luminance versus operational time at a constant current density of 20 mA cm^{-2} for Pd3O3, Pd3O8-P and Pd3O8-Py5 based devices. The general device structure is ITO/ HATCN (10 nm)/ NPD (70 nm)/ TrisPCz (10 nm)/ emitter (20 nm)/ BAlq (10 nm)/ BPyTP (50 nm)/ LiF (1 nm)/ Al (100 nm). EQE versus luminance of the devices with

optical outcoupling enhancement were measured by applying index matching gel between silicon photodiode and glass substrate.

As shown in Figure 3.26a, all devices showed exclusive and redshifted aggregate emission in comparison to the observed PL spectra of their corresponding emitter thin films. Such discrepancies can be attributed to the effect of the optical cavity device settings on the EL spectra measured in the forward direction. Additionally, the device efficiencies exhibited a large degree of variation due to the choice of emissive materials. The peak EQEs of Pd3O8-Py5, Pd3O8-P and Pd3O3 based devices are 37.3%, 34.8% and 29.8% respectively (Figure 3.26c), which could be attributed to the difference of their Θ values of 95%, 90% and 85%. It is worth mentioning that Pd3O8-Py5 device retained high EQEs of 36.0% and 32.5% at 1000 and 10000 cd m^{-2} respectively, indicating that Pd3O8-Py5 based device had a broader exciton recombination zone, leading to suppressed TTA and TPQ processes and a reduced efficiency roll-off. Moreover, by applying an index matching gel between silicon photodiode and the OLED glass substrate without an air gap, the device efficiency consisting of both air mode and substrate mode ($EQE_{air+sub}$) was remeasured.[12, 94] The peak $EQE_{air+sub}$ of Pd3O8-Py5 device was increased to 67.4% with around 80% enhancement. The observation of similar efficiency enhancement for all devices indicated that phosphorescent emitters with predominant horizontal emitting dipoles could not only produce more photons in the air mode but also generate more photons trapped in the substrate mode.

Table 3.3 Device performance data summary for Pd3O3, Pd3O8-P, Pd3O8-Py2 and Pd3O8-Py5 based devices.

Devices	Pd3O3	Pd3O8-P	Pd3O8-Py2	Pd3O8-Py5	Pd3O8-Py5-*f*
Deposition rate of emitter	0.3 Å s^{-1}	0.3 Å s^{-1}	0.3 Å s^{-1}	0.3 Å s^{-1}	2.4 Å s^{-1}
λ_{max} [nm]	600	588	590	592	592
Peak EQE [%]	29.8	34.8	33.9	37.3	34.0
EQE (%) @ 1000 cd m^{-2}	28.8	33.5	31.2	36.0	31.0
EQE (%) @ 10000 cd m^{-2}	24.5	29.5	26.8	32.5	25.5
Peak PE [lm W^{-1}]	94.1	129.0	137.0	140.7	129.0
PE [lm W^{-1}] @ 1000 cd m^{-2}	74.1	101.0	100.8	105.8	92.3
PE [lm W^{-1}] @ 10000 cd m^{-2}	48.4	67.4	65.4	74.0	57.7
L_0 [cd m^{-2}]	12098	16650	15466	17304	13789
LT_{95} @ L_0 [h]	4	171	28	504	50
LT_{95} @ 1000 cd m^{-2} [h][a)]	215	15391	2240	48246	3328
Peak $EQE_{air+sub}$ [%]	52.9	61.7	63.9	67.4	62.3
$EQE_{air+sub}$ [%] @ 1000 cd m^{-2}	51.9	60.4	60.7	66.2	58.9
$EQE_{air+sub}$ [%] @ 10000 cd m^{-2}	46.7	55.3	54.8	61.9	51.3
Peak $PE_{air+sub}$ [lm W^{-1}]	166.8	234.5	268.8	253.4	241.8
$PE_{air+sub}$ [lm W^{-1}] @ 1000 cd m^{-2}	138.0	189.4	196.4	201.5	181.6
$PE_{air+sub}$ [lm W^{-1}] @ 10000 cd m^{-2}	102.6	142.8	146.8	155.0	130.0

[a)] Estimated from the equation $LT(L_1) = LT(L_0)(L_0/L_1)^n$, where n is 1.60.

The device operational stabilities of Pd3O3, Pd3O8-P and Pd3O8-Py5 devices at a constant driving current density of 20 mA cm^{-2} were examined, as shown in Figure 3.26d. Given that the display industry is trying to minimize the image sticking effect as well as differential aging effect on the displays, LT_{95} lifetime was chosen as metrics and experimentally determined.[97] The measured LT_{95} value of Pd3O3, Pd3O8-P and Pd3O8-Py5 devices was 4, 17 and 504 h respectively. Compared to Pd3O3 with possibly poor hole mobility, Pd3O8-P has improved its hole transporting capability with the

addition of benzo[4,5]imidazo[1,2-f]phenanthridine component, leading to a broadened exciton recombination zone and an improved device operational stability. Further balanced hole and electron conductivities with the existence of 5-aza atom for Pd3O8-Py5 appeared to play an effective role in increasing LT_{95} value at 20 mA cm^{-2} to 504 h with close to 200% enhancement compared to Pd3O8-P device. It is worth noting that a small structural change between Pd3O8-P and Pd3O8-Py5 could lead to drastic improvement in both device efficiency and operational stability, which completely validate the significance of maintaining a robust material development effort for the rapid growth of organic semiconductor industries. Moreover, lifetime (LT) at different luminance value can be estimated using the formula $LT(L_1) = LT(L_0)(L_0/L_1)^n$, where L_1 is the desired luminance, and the escalation factor n value is based on the experimentally obtained n of 1.60 for Pd3O8-P devices.[98] As a result, Pd3O8-Py5 device demonstrated a long estimated LT_{95} lifetime of 48246 h at 1000 cd m^{-2}, to the authors' best knowledge, which is the most stable reported OLED among all of emissive materials on the public domain.[19, 33, 56, 79, 100–102, 111]

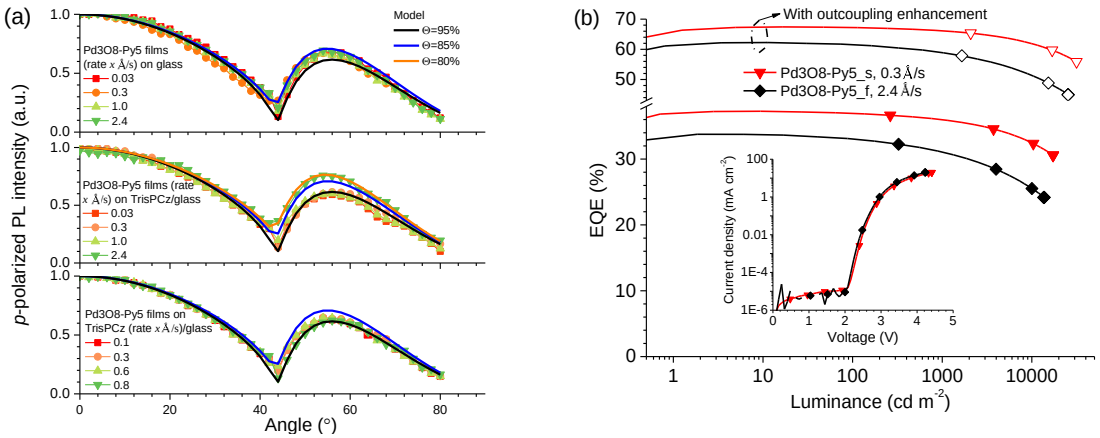

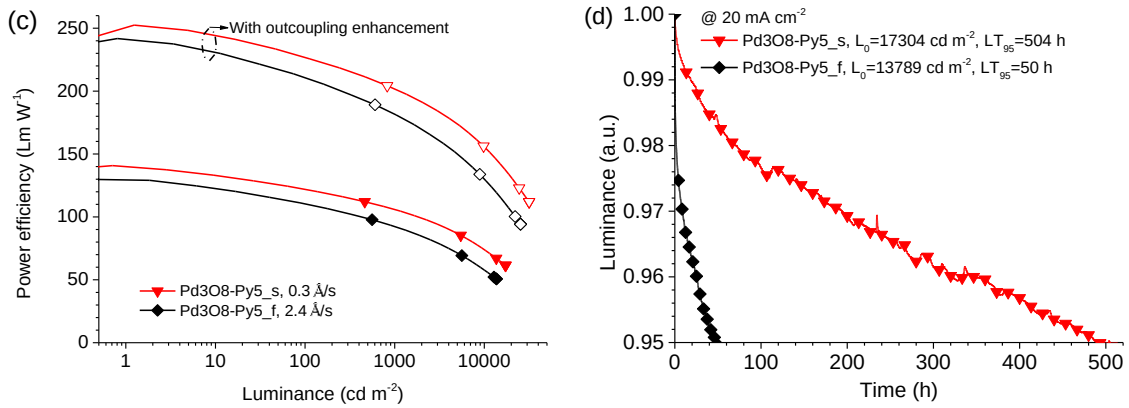

Figure 3.27 a) Experimentally obtained angle-dependent PL intensities of the *p*-polarized light for 20-nm-thick Pd3O8-Py5 films with various deposition rates of 0.03, 0.3, 1.0, 2.4 Å s^{-1} grown on glass substrate (top), 10-nm-thick TriPCz/glass substrate (middle), and experimentally obtained angle-dependent PL intensities of the *p*-polarized light for 20-nm-thick Pd3O8-Py5 thin films with fixed rate of 0.3 Å s^{-1} grown on template layers of TriPCz deposited at various rates of 0.1, 0.3, 0.6 and 0.8 Å s^{-1} (bottom). b) EQE versus luminance, c) PE versus luminance and d) plots of relative luminance versus operational time at a constant current density of 20 mA cm^{-2} for two devices by depositing Pd3O8-Py5 at 0.3 and 2.4 Å s^{-1} in a general structure ITO/ HATCN (10 nm)/ NPD (70 nm)/ TrisPCz (10 nm)/ Pd3O8-Py5 (20 nm, *x* Å s^{-1})/ BAlq (10 nm)/ BPyTP (50 nm)/ LiF (1 nm)/ Al (100 nm).

To further investigate the influence of the deposition condition on the quality of aggregate emissive layers, a series of Pd3O8-Py5 films were prepared at various deposition rates and on various substrates. Figure 3.27a shows the angle-dependent PL intensities of the *p*-polarized light for Pd3O8-Py5 films with various deposition rates of 0.03, 0.3, 1.0 and 2.4 Å s^{-1}. At the deposition rate ranging from 0.03 to 2.4 Å s^{-1} on a bare glass, Pd3O8-Py5 films maintained identical Θ values of 90%. On the other hand, the glass substrate with pre-deposited 10-nm-thick TrisPCz increased Θ values of Pd3O8-Py5 aggregates to 95% at moderate deposition rates between 0.03 and 1.0 Å s^{-1}, and decreased the Θ value to 85% with a deposition rate of 2.4 Å s^{-1}. In addition, the TrisPCz layer deposition rate appeared to have no effect on the quality of Pd3O8-Py5

films. The Θ values of Pd3O8-Py5 thin films were kept at a constant value of 95% with various pre-deposited TriPCz layers.

Provided that Pd3O8-Py5 thin films with deposition rate below 1.0 Å s^{-1} showed almost identical Θ values, two devices with Pd3O8-Py5 layer at the deposition rate of 0.3 and 2.4 Å s^{-1} (named as Pd3O8-Py5_s and Pd3O8-Py5_f devices respectively) were fabricated and studied. As shown in Figure 3.27b, compared to the peak EQE of 37.3% for Pd3O8-Py5_s device, Pd3O8-Py5_f device displayed a smaller peak EQE of 34.0%, which could be attributed to its smaller Θ value of 85%. Moreover, a more pronounced efficiency roll-off was observed for Pd3O8-Py5_f device, which exhibited EQEs of 31.0 % and 25.5% at 1000 and 10000 cd m^{-2} respectively. Similarly, Pd3O8-Py5_f device exhibited a much shortened measured LT_{95} lifetime of 50 h with an initial brightness of 13789 cd m^{-2}, as shown in Figure 3.27d. It becomes apparent that the quality of aggregate emissive layer is susceptible to the thin film deposition conditions, which could modify the charge recombination and exciton formation processes inside of emissive layer, leading to the variation in device efficiency and operational stability. For an optimized Pd3O8-Py5 device, it exhibited a peak power efficiency (PE) of 140.7 lm W^{-1}, and maintained a high PE of 105.8 lm W^{-1} at 1000 cd m^{-2} (Figure 3.27c), which is attributed to its high EQE and low corresponding driving voltage. Moreover, by utilizing the photons trapped in air and substrate mode, its remeasured peak $PE_{air+sub}$ was increased to 253.4 lm W^{-1}, and the device $PE_{air+sub}$ can reach 201.5 lm W^{-1} at 1000 cd m^{-2}. Such a high efficacy amber light panel (blue light free) can make a strong impact on the development of specialized lighting products for medical and automobile applications, indicating a

great potential of utilizing phosphorescent molecular aggregates for future lighting applications.

3.2.4 Conclusion

In summary, the electrochemical and photophysical properties of four tetradentate Pd(II) complexes with judicious ligand design, i.e. Pd3O3, Pd3O8-P, Pd3O8-Py2 and Pd3O8-Py5, were examined. By optimizing the thin film deposition condition, a host-free OLED device employing Pd3O8-Py5 aggregates achieved a peak EQE of 37.3% and a reduced efficiency roll-off with high EQEs of 36.0% and 32.5% at 1000 and 10000 cd m^{-2} respectively. Moreover, such efficient device also demonstrated a long measured LT_{95} lifetime of over 500 h with an initial brightness of 17304 cd m^{-2} corresponding to an estimated LT_{95} of 48246 h at 1000 cd m^{-2}, which is the most stable reported OLED among all of emissive materials on the public domain. Such outstanding performance demonstrated the great potential of square planar Pd(II) complexes as emissive materials for display and lighting applications. Moreover, the further improved device efficiency can be expected by utilizing the low-refractive-index charge transporting and blocking materials to maximize device outcoupling efficiency.[16, 112, 113]

4 STABLE AND EFFICIENT NEAR-INFRARED ORGANIC LIGHT-EMITTING DIODES EMPLOYING A PLATINUM(II) PORPHYRIN COMPLEX

4.1 Background

Near-infrared light-emitting diodes have been intensively investigated by academics and industrial professionals for their application in biometric authentication as well as in night vision displays and telecommunications.[114–116] Most recently, there has been a specific interest in near-infrared organic light-emitting diodes (NIR OLEDs) as they show distinct advantages over their inorganic counterparts due to their compatibility with flexible substrates, high-resolution patterning, and fabrication with low-cost vapor deposition process.[42, 49, 73, 103] An increasing demand for applications in the NIR region has driven the development of NIR OLEDs with an emission spectrum beyond 900 nm. Typically, OLEDs within the near-infrared emission region experience poor device efficiencies which can be attributed to inefficient emissive materials or poorly designed device architectures.[114] Moreover, NIR OLEDs have to be operated at a high current density range to reach a targeted output optical power for practical applications which consequently results in expedited device degradation. Thus, there is an urgent need to develop efficient and stable NIR OLEDs from the perspective of both emissive material development and device structure optimization.

Among all the emissive material candidates for NIR OLEDs, including fluorescent materials[117–121], thermally activated delayed fluorescent materials,[18, 122] lanthanide complexes,[123–125] and transition-metal-based complexes,[52, 126–129, 40] phosphorescent porphyrin-based complexes have shown a lot of promise due to their narrow spectral bandwidth, comparatively high photoluminescent quantum

efficiency in the deep NIR region, and notable performance in stable device operations.[7, 130, 131] Near-infrared OLEDs based on a Pt(II)-porphyrin complex, i.e. Pt(II)-tetraphenyltetrabenzoporphyrin (PtTPTBP), reported by Thompson and co-workers, exhibited a peak external quantum efficiency (EQE) of 8.5% in a strong charge confined device structure,[132] and an operational lifetime of LT_{90} (time to 90% of the initial photo current) longer than 1000 h at 40 mA cm^{-2} in a stable device structure.[131] However, the emission spectrum of such device peaked only at 772 nm with the majority of electroluminescent wavelengths shorter than 800 nm.

Two strategies have been extensively explored to shift the emission wavelength of porphyrin complexes towards a deep NIR spectral region. One approach is to develop Pt(II)-azaporphyrin complexes, through which the conjugation systems are modified by replacing one or multiple meso carbon atoms with nitrogen atoms on the tetrabenzoporphyrin ring. For example, cis-PtN_2TBP and PtNTBP demonstrated largely bathochromic-shifted emissions peaking at 848 and 846 nm respectively compared to PtTPTBP, although the electroluminescent (EL) spectra was deemed unsatisfactory due to the small portion (~5%) of emitting photons with wavelengths longer than 900 nm.[39] The other approach focuses on decorating the pyrrolic rings with π-extended conjugation system. Schanze and co-workers reported a family of π-extended PtTPTBP derivatives, for which Pt(II) tetraphenyltetranaphthoporphyrin (PtTPTNP) and Pt(II) tetra(3,5-di-tert-butylphenyl)tetraanthroporphyrin ($PtAr_4TAP$) exhibited further bathochromic-shifted electroluminescent emissions peaking at 900 and 1005 nm, respectively.[41, 130, 133] However, $PtAr_4TAP$ was too heavy to be sublimed for vapor deposited OLEDs, and a solution based PLED exhibited a low EQE of 0.20% due to limited sets of suitable

functional materials.[133] On the other hand, PtTPTNP based OLEDs showed a highly respectable EQE of 3.8% with 50% emitting photons with wavelengths longer than 900 nm.[130] To develop more stable NIR OLEDs, it will be highly desirable to further improve the thermal stability of PtTPTNP, as its high sublimation temperature (>400 °C) and low sublimation yield (<10%) presents challenges in maintaining high quality material preparation and fabricating potentially stable OLEDs.

In this chapter, a novel PtTPTNP derivative was developed by introducing fluorine atoms on the meta positions of all four phenyl groups in TPTNP, i.e. Pt(II) tetra(3,5-difluorophenyl)tetranaphthoporphyrin (PtTPTNP-F_8), demonstrating a bathochromic-shifted electroluminescent (EL) spectrum peaking at 920 nm with 84% of photos with spectral wavelengths of longer than 900 nm. The judicious molecular design also improved the thermal stability of PtTPTNP-F_8 with a reduced sublimation temperature of below 400 °C and an improved sublimation yield of above 90%. Moreover, a one-step synthetic method for porphyrin ring has been developed, which can significantly simplify the synthetic routes and lower the material synthesis cost. A PtTPTNP-F_8 based OLED with a carefully selected host achieved a peak EQE of 1.9%, and a LT_{97} lifetime of more than 400 h at a constant current density of 20 mA cm^{-2}. In addition, a NIR OLED device using known stable components with PtTPTNP-F_8 demonstrated superior operational stability with a measured LT_{99} lifetime of longer than 1000 h at 20 mA cm^{-2}.

4.2 Experimental Section

Materials and regents: All commercial reagents were purchased and used as received without further purification. 1H-benzo[f]isoindole-1,3(2H)-dione, 2-(3,5-

difluorophenyl)acetic acid, ZnO, benzonitrile, and anisole were purchased from Sigma-Aldrich. Platinum(II) chloride ($PtCl_2$) was purchased from Alfa Aesar. Dichloromethane (DCM) was purchased from Fisher Scientific. Hydrochloric acid solution was purchased from BDH. All reactions were carried out under an inert N_2 atmosphere in oven-dried glassware. External bath temperatures were used to record all reaction mixture temperatures. For the two porphyrin-based NIR emitters, their synthetic methods are shown in Figure 4.1.

4.2.1 Preparation of PtTPTNP-F_8

Synthesis of ZnTPTNP-F_8: 1H-benzo[f]isoindole-1,3(2H)-dione (2.0 g, 10.14 mmol) and 2-(3,5-difluorophenyl)acetic acid (3.5 g, 20.28 mmol) were loaded into a round-bottom flask. The mixture was melted and stirred for 0.5 hour at 200 °C under a nitrogen atmosphere. ZnO (0.21 g, 2.54 mmol) was added to the melted mixture, and then heated at 310 °C for 5 hours. After that, the reaction mixture was cooled down to room temperature, and purified by column chromatography on Al_2O_3 using DCM and THF (200:1-50:1) as eluent to afford the desired product ZnTPTNP-F_8 as a dark-green solid (0.87 g, yield: 28%). ^{1}H NMR (500 MHz, $CDCl_3$, δ): 7.99 (d, *J*=5.0 Hz, 8H), 7.89-7.82 (m, 8H), 7.80 (s, 8H), 7.65-7.54 (m, 12H).

Synthesis of H_2TPTNP-F_8: To a solution of ZnTPTNP-F_8 (0.5 g, 0.41mmol) in 20 mL of dichloromethane (DCM) was added 10 mL of 6 M hydrochloric acid aqueous solution. The mixture was stirred at room temperature for 20 minutes, and then was extracted with DCM for three times. The combined organic layer was concentrated and the residue was purified by column chromatography on Al_2O_3 using DCM and hexane (1:10-1:2) as eluent to afford the desired product H_2TPTNP-F_8 as a dark-green solid (0.36

g, yield: 76%). ^{1}H NMR (500 MHz, $CDCl_3$, δ): 8.03 (d, *J*=5.5 Hz, 8H), 7.91-7.70 (m 16H), 7.62-7.51 (m, 12H).

Synthesis of PtTPTNP-F_8: $PtCl_2$ (0.08 g, 0.292 mmol) was dissolved in 10 mL of benzonitrile and was stirred for 20 min at 100 °C under a N_2 atmosphere. H_2TPTNP-F_8 (0.17 g, 0.146 mmol) and 50 mL of anisole was added into the solution, and then the mixture was stirred overnight at 160 °C. The mixture was cooled down to room temperature, and then the solvent was removed under reduced pressure. The residue was purified through column chromatography on Al_2O_3 using DCM and hexane (1:10-1:1) as eluent to afford the desired product PtTPTNP-F_8 as dark-green powder (0.17g, yield: 85%). The product was further purified by sublimation in a four-zone thermal-gradient furnace under high vacuum (380°C, 4.5×10^{-6} Torr) to afford the dark-green powder with a yield of 91%. ^{1}H NMR (500 MHz, $CHCl_3$, δ): 7.94 (d, *J*=6.5 Hz, 8H), 7.83-7.81 (m, 8H), 7.72 (s, 8H), 7.60-7.57 (m, 12H).

4.2.2 Preparation of PtTPTNP

Synthesis of ZnTPTNP: 1H-benzo[f]isoindole-1,3(2H)-dione (2.0 g, 10.14 mmol) and phenylacetic acid (2.8 g, 20.28 mmol) were loaded into a round-bottom flask. The mixture was melted and stirred for 0.5 hour at 200 °C under a nitrogen atmosphere. ZnO (0.21 g, 2.54 mmol) was added to the melted mixture, and then heated at 310 °C for 5 hours. After that, the reaction mixture was cooled down to room temperature, and purified by column chromatography on Al_2O_3 using DCM and THF (200:1-50:1) as eluent to afford the desired product ZnTPTNP as a dark-green solid (0.60 g, yield: 22%). ^{1}H NMR (400 MHz, $CDCl_3$, δ): 8.31 (d, *J*=6.5 Hz, 8H),), 8.07 (t, *J*=7.3 Hz, 4H), 7.93 (t, *J*=7.5 Hz,, 8H), 7.70-7.64 (m, 12H), 7.45-7.40 (m, 12H).

Synthesis of H_2TPTNP: To a solution of ZnTPTNP (0.15 g, 0.14 mmol) in 15 mL of dichloromethane (DCM) was added 15 mL of 6 M hydrochloric acid aqueous solution. The mixture was stirred at room temperature for 20 minutes, and then was extracted with DCM for three times. The combined organic layer was concentrated and the residue was purified by column chromatography on Al_2O_3 using DCM and hexane (1:10-1:2) as eluent to afford the desired product H_2TPTNP as a dark-green solid (0.11 g, yield: 80%). ^{1}H NMR (400 MHz, $CDCl_3$, δ): 8.45 (d, *J*=6.7 Hz, 8H),), 8.07 (t, *J*=7.4 Hz, 4H), 7.96 (t, *J*=7.6 Hz,, 8H), 7.76-7.62 (br, 12H), 7.56-7.31 (br, 12H).

Synthesis of PtTPTNP: $PtCl_2$ (0.026 g, 0.098 mmol) was dissolved in 1 mL of benzonitrile and was stirred for 20 min at 100 °C under a N_2 atmosphere. H_2TPTNP (0.050 g, 0.049 mmol) and 5 mL of anisole was added into the solution, and then the mixture was stirred overnight at 160 °C. The mixture was cooled down to room temperature, and then the solvent was removed under reduced pressure. The residue was purified through column chromatography on Al_2O_3 using DCM and hexane (1:10-1:1) as eluent to afford the desired product PtTPTNP as dark-green powder (0.054g, yield: 92%). ^{1}H NMR (400 MHz, $CDCl_3$, δ): 8.36 (d, *J*=7.7 Hz, 8H), 8.08 (t, *J*=7.7 Hz, 4H), 7.97 (t, *J*=7.4 Hz, 8H), 7.73-7.58 (br, 12H), 7.54-7.37 (br, 12H).

4.3 Results and Discussion

A typical synthetic procedure for Pt(II)-porphyrin complexes relies on the macrocycle formation, subsequent aromatization, and metalation. As shown in Figure 4.1, the traditional synthesis of intermediate H_2TPTNP took six reaction steps in total to afford the target molecule.[41, 130, 134, 135] It should be noted that the dilute solution required in the macrocycle formation process was not conducive to the scale-up of the

reaction. Inspired by Borisov's synthetic strategy for PtTPTBP,[136] the synthetic route to obtain both PtTPTNP and PtTPTNP-F_8 was improved and demonstrated in Scheme 1, in a simple and cost-effective way. Firstly, the porphyrin ring was synthesized by a template method in just a single step with zinc oxide to form the template under neat reaction condition. Due to the poor solubility, 1H-benzo[f]isoindole-1,3(2H)-dione was dissolved by phenylacetic acid or 2-(3,5-difluorophenyl)acetic acid firstly to ensure the miscibility of materials in the neat reaction system. As a result, the macrocycle formation for the intermediates, i.e., ZnTPTNP and ZnTPTNP-F_8, was largely facilitated in yields of 22% and 28%, respectively. It is worth mentioning that the fluorine substituents could promote the miscibility of materials better, leading to an improved reaction yield. Then the Pt(II)-porphyrin complexes were synthesized through the demetallation followed by platination. The synthetic route developed in this work simplified the reaction process, lowered the cost, and maintained a comparable yield in comparison with the previous synthetic approach. It was notable besides promoting the reaction, the introduction of fluorine substituents could also greatly increase the sublimation yield of PtTPTNP-F_8 larger than 90%.

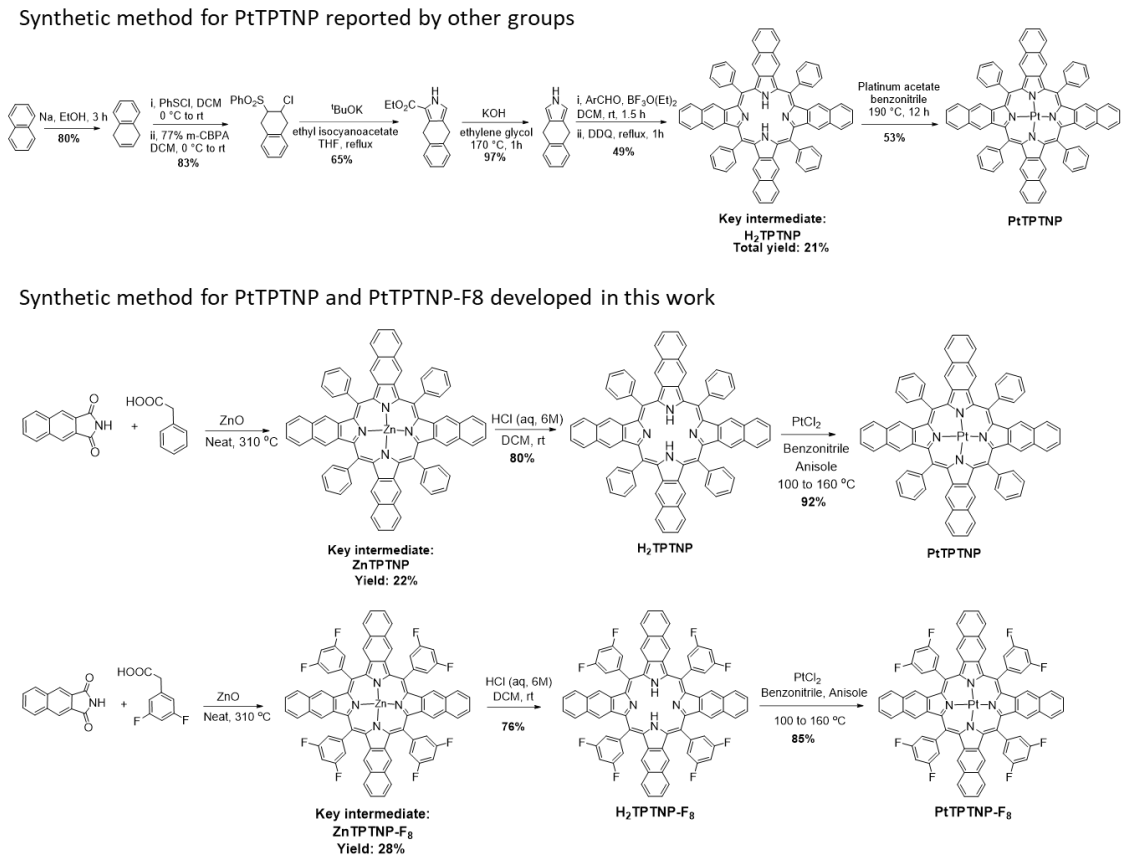

Figure 4.1 Synthetic routes for PtTPTNP reported in literature versus PtTPTNP and PtTPTNP-F_8 developed in this work.

The room-temperature absorption and emission spectra of PtTPTNP-F_8 in CH_2Cl_2 are provided in Figure 4.2a. The absorption spectrum displayed a Soret band peaking at 432 nm, corresponded to the $S_0 \rightarrow S_2$ transition, and a relatively stronger Q band absorption peaking at 695 nm, associated with the $S_0 \rightarrow S_1$ transition. PtTPTNP (Figure 4.3) showed quit similar absorption patterns to PtTPTNP-F_8. By comparison, the Q band absorption of PtTPTNP-F_8 exhibited a bathochromic shift of 6 nm relative to PtTPTNP. The photoluminescent spectrum of PtTPTNP-F_8 also displayed a bathochromic-shifted emission with a λ_{max} of 920 nm, deeper into NIR region than a reported λ_{max} of 883 nm for PtTPTNP.[130] The luminescent lifetime (τ) of PtTPTNP-F_8 in PMMA film at room

temperature was measured to be 15.4 μs, with a photoluminescent quantum yield (Φ_{PL}) of 9.7±5%.

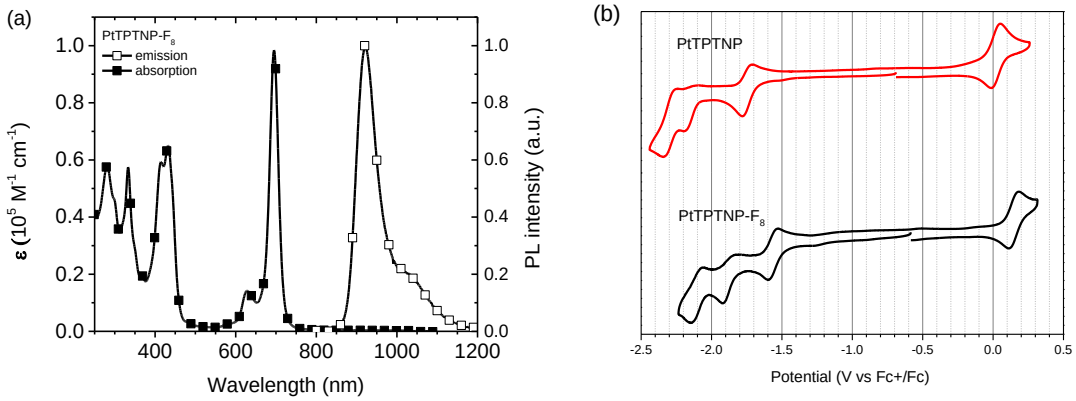

Figure 4.2 a) Room temperature absorption and photoluminescent emission of PtTPTNP-F_8. b) Cyclic voltammogram for PtTPTNP-F_8 and PtTPTNP in DMF, the oxidation and reduction potentials were determined by differential pulse voltammetry versus a ferrocene internal reference.

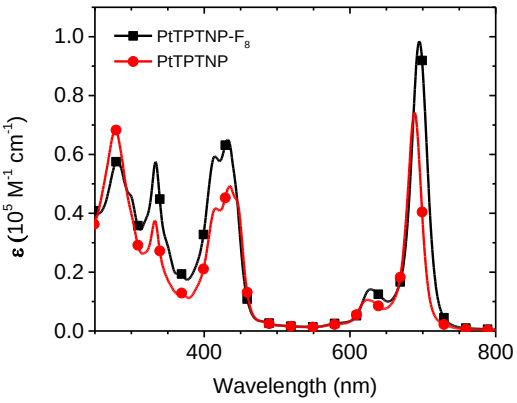

Figure 4.3 Room temperature absorption spectra of PtTPTNP-F_8 and PtTPTNP.

The electrochemical properties of PtTPTNP-F_8 and PtTPTNP were also examined by performing cyclic voltammetry (CV) in DMF, as shown in Figure 4.2b. The oxidation and reduction potentials were determined to be 0.11, -1.59, -1.92, and -2.14 V for PtTPTNP-F_8, and 0.024, -1.78, -2.32, and -2.81 V for PtTPTNP versus a ferrocene internal reference by differential pulse voltammetry. PtTPTNP-F_8 showed a

electrochemical smaller band gap of 1.70 eV by comparison with that of 1.80 eV for PtTPTNP. It was found that the fluorine substituents strongly affected the reduction potential without significantly affecting the oxidation potential, and shifted the reduction potential to a less negative value. The highest occupied molecular orbital (HOMO) and lowest unoccupied molecular orbital (LUMO) levels for PtTPTNP-F_8 calculated from its CV data were -4.75 and -2.97 eV, respectively.[137] It should be noted that the oxidation and reduction peaks of PtTPTNP-F_8 demonstrated reversible characteristics, which are highly desirable for phosphorescent emitters with long-term device operational stability.

The performance of PtTPTNP-F_8 in device settings was evaluated. PtTPTNP-F_8 was doped into 4,4'-Bis(N-carbazolyl)-1,1'-biphenyl (CBP) and bathocuproine (BCP) was utilized as HBL (device 1), both of which were consistent with the host and hole blocking materials used in previously reported PtTPTNP based OLEDs.[130] Taking into account the electrochemical instability of BCP, another device with a known stable hole blocker of BAlq (device 2) was also fabricated.[37, 138] The general device structure was ITO (100 nm)/ HATCN (10 nm)/ NPD (40 nm)/ 4% PtTPTNP-F_8 : CBP (25 nm)/ HBL (10 nm)/ BPyTP (40 nm)/ Liq (2 nm)/ Al.

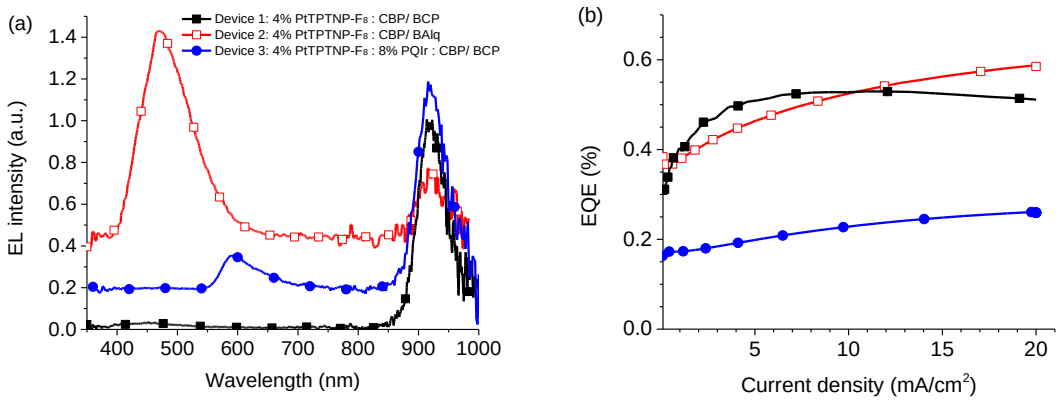

Figure 4.4 a) Electroluminescent spectra and b) EQE versus current density for devices 1-3 in a general device structure ITO/ HATCN (10 nm)/ NPD (40 nm)/ EML (25 nm)/ HBL (10 nm)/ BPyTP (40 nm)/ Liq (2 nm)/ Al, where device 1 is 4% PtTPTNP-F_8: CBP/ BCP, device 2 is 4% PtTPTNP-F_8: CBP/ BAlq, and device 3 is 4% PtTPTNP-F_8: 8% PQIr: CBP/ BCP.

The electroluminescent spectra for devices 1-2 are shown in Figure 4.4a. Device 1 exhibited a predominant PtTPTNP-F_8 emission peaking at 920 nm. A small amount of residual emission ranging from 350 to 550 nm was also detected, likely originating from the CBP, though no such residual emission was reported in previous PtTPTNP based device.[130] The peak EQE of device 1 was measured to be only 0.53%, as shown in Figure 4.4b, lower than the reported value of 3.8% for the PtTPTNP based OLED. Such discrepancy regarding the non-exclusive emission spectra and device efficiency can be attributed to two possible reasons: firstly, insufficient energy was transferred from CBP to PtTPTNP-F_8 because of the poor spectral overlap between the CBP emission and the PtTPTNP-F_8 absorption; secondly, device structure was not optimized for outcoupling efficiency. In device 2, the PtTPTNP-F_8 emission became very weak. In contrast, a non-exclusive emission peaking at 469 nm was pronounced, which was likely to originate from BAlq emission caused by undesired hole leakage into HBL and indicated the severe

charge imbalance inside this device setting. As expected, device 2 with an EQE of 0.58%, showed no obvious efficiency improvement.

To improve device efficiency, PQIr, as a potential sensitizer, was introduced into the emissive layer to assist the energy transfer from CBP to PtTPTNP-F_8. Referred to as device 3, the device has an emissive layer structure of 4% PtTPTNP-F_8: 8% PQIr: CBP. As shown in Figure 4.4, device 3 exhibited an electroluminescent spectrum consisting of a dominant PtTPTNP-F_8 emission as well as a non-exclusive emission peaking at 594 nm, and a low EQE of below 0.26%. The observed non-exclusive emission was likely attributed to PQIr emission because of an inefficient energy transfer from PQIr to PtTPTNP-F_8. One possible reason was that the fast radiative decay process of PQIr effectively competed against the energy transfer process from PQIr to PtTPTNP-F_8. Another possible explanation was that the compact recombination zone elongated the diffusion length from PQIr to PtTPTNP-F_8. It should be noted that the elimination of non-exclusive emission from CBP indicated efficient energy transferred from host to either sensitizer or dopant. Nevertheless, more studies, beyond the scope of this research, are needed to uncover and realize the efficient energy transfer in such devices consisting of sensitizer/phosphorescent emitters.

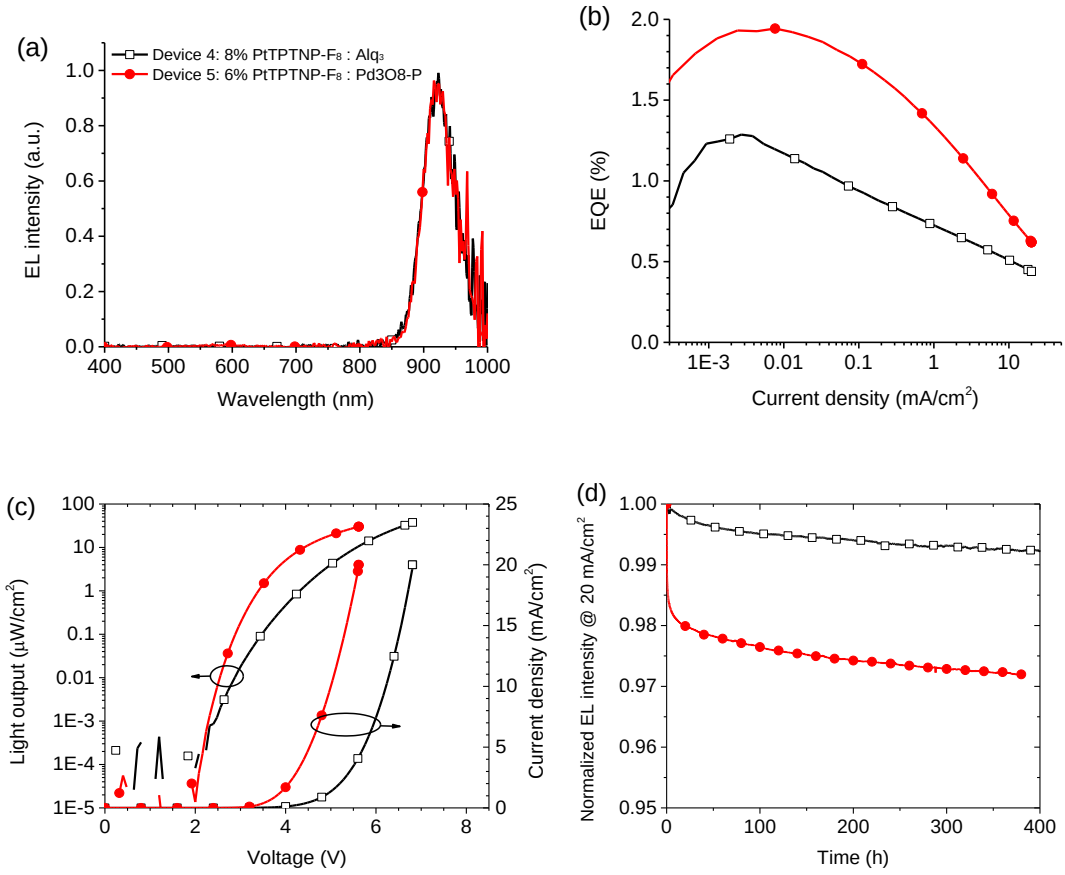

Figure 4.5 a) Electroluminescent spectra, b) EQE versus current density, c) radiant emittance and current density versus voltage, and d) relative EL intensity versus operational time at a constant current density of 20 mA cm^{-2} for devices 4-5. The general structure of devices 4 is ITO/ HATCN (10 nm)/ NPD (40 nm)/ 8% PtTPTNP-F_8: Alq_3 (25 nm)/ BAlq (10 nm)/ BPyTP (40 nm)/ Liq (2 nm)/ Al. The general structure of device 5 is ITO/ HATCN (10 nm)/ NPD (70 nm)/ 6% PtTPTNP-F_8: Pd3O8-P (25 nm)/ BAlq (10 nm)/ BPyTP (50 nm)/ Liq (2 nm)/ Al.

To further improve the device efficiency, tris-(8-hydroxyquinoline)aluminum (Alq_3) and Pd(II) 7-(3-(pyridin-2-yl-κN) phenoxy-κC)(benzo[4,5]imidazo-κN)([1,2-f]phenanthridine-κC) (Pd3O8-P) were selected as the hosts, respectively. On the one hand, the electron-transporting characteristic of Alq_3 or Pd3O8-P served to confine the charge carriers inside the EML. On the other hand, the larger spectral overlap between the Alq_3 or Pd3O8-P emissions and the PtTPTNP-F_8 Q band absorption facilitated the

energy transfer from the host to the emitter. Moreover, the known stable hole blocking material BAlq was selected as the HBL to further study the operational stabilities of NIR OLEDs.

Observed from Figure 4.5a, both devices 4 and 5 showed identical EL spectra with an exclusive emission from PtTPTNP-F_8 peaking at 920 nm. The percentage of PtTPTNP-F_8 emitted photons with wavelength beyond 900 nm drastically increased to 84%, exceeding the value of ~50% in the reported PtTPTNP based OLED, as shown in Table 4.1. It is worth mentioning that no emission was observed from HBL, i.e. BAlq, indicating a good charge carrier confinement inside the EML. According to Figure 4.5b, device 4 showed a peak EQE of 1.3%. In contrast, device 5 achieved a much higher peak EQE of 1.9%, which is comparable to the reported highest EQE (2.1%) of NIR OLEDs with the peak emission at 930 nm, to the authors' best knowledge;[40] however, device 5 had a much narrower EL spectrum with a full width at half maximum (FWHM) of 62 nm compared with that of ~190 nm for those reported efficient NIR OLEDs.[40] It should be pointed out that although device 5 experienced a severe efficiency roll-off, it is believed that such problem can be combated by broadening the recombination zone with a more charge-balanced device structure, which will be studied in future research. The device efficiency performance of device 5 demonstrated that porphyrin can be also a promising NIR emitter candidate to realize the high efficiency in the emission range beyond 900 nm. In addition, as shown in Figure 4.5c, devices 5 demonstrated a smaller driving voltage of 5.6 V to reach 20 mA cm^{-2} compared to that of 6.8 V for device 4, indicating a better device conductivity by utilizing Pd3O8-P as host. Correspondingly, devices 4 and

5 exhibited intensities of 37.1 and 30.2 μW cm^{-2} at a current density of 20 mA cm^{-2}, respectively.

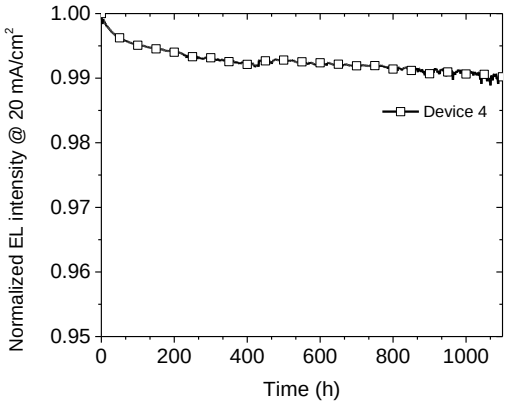

Figure 4.6 Relative EL intensity versus operational time at a constant current density of 20 mA cm^{-2} for Devices 4.

The operational stabilities of devices 4 and 5 were measured at a constant current density of 20 mA cm^{-2}, as shown in Figure 4.5d and Figure 4.6. Device 4 showed an excellent operational stability with LT_{99} lifetime of longer than 1000 h (Figure 4.6) and demonstrated the most stable OLED device operating at such a high current density among all the reported devices within the visible and NIR light range, to the authors' best knowledge.[131, 79, 33, 99] Device 5 also exhibited a very decent operational stability with LT_{97} lifetime of longer than 400 h. Such superior operational stabilities of both devices were mainly attributed to two factors: the sufficient suppression of chemical bond dissociation due to relatively low-energy hot (multiply excited) excitons or polarons, and the significantly weakened triplet-triplet annihilation and triplet-polaron quenching as a result of improved charge balance in the carefully selected device structure. Additionally, it is worth mentioning that the long-lived devices, employing fluorinated metal complex

as emitter, demonstrated that the fluorine substituents can be electrochemically stable in devices when they had minimum contribution in the HOMO orbitals.[139–141]

Table 4.1 Photophysical properties and device performance data summary for Pt(II) porphyrin complexes and devices incorporating them.

Pt(II) porphyrins	Soret, Q band/nm ($\varepsilon\times10^5$ M^{-1} cm^{-1})	emission at RT			device performance			
		λ_{max} /nm	Φ_{PL} /%	τ /μs	λ_{max} /nm	peak EQE /%	percentage of spectral area ≥900 nm	reference
PtTPTBP	425 (2.03), 610 (1.35)	770	70	53	772	8.5	0	[131, 132]
PtNTBP	403 (1.06), 628 (1.37)	842	22	40	848	2.8	0	[39, 142]
cis-PtN_2TBP	387 (0.51), 620 (1.47)	830	17	20	846	1.5	0	[39, 142]
PtTPTNP	436 (0.91), 689 (1.48)	883	15	12.7	900	3.8	~50%	[41, 130]
$PtAr_4TAP$	455 (0.29), 762 (0.46)	1022	8	3.2	1005	0.2	100%	[41, 133]
PtTPTNP-F_8	432 (0.65), 695 (0.98)	920	9.7	15.4	920	1.9	84%	this work

4.4 Conclusion

A simple and cost-effective synthetic approach was developed to afford the efficient and stable near-infrared PtTPTNP-F_8. By introducing fluorine atoms on the aromatic ring system, the thermal stability of PtTPTNP-F_8 was drastically increased with an exceptional sublimation yield of above 90%. An optimized OLED employing PtTPTNP-F_8 showed an exclusive NIR emission peaking at 920 nm and a peak EQE of 1.9%. Moreover, devices of PtTPTNP-F_8 fabricated in a known stable device structure achieved a measured LT_{99} lifetime of more than 1000 h at 20 mA cm^{-2}, which marks the most stable OLED operating at such a high current density among all reported visible or invisible emissive materials in the public domain. Future optimization of host and

blocking materials are expected to further improve the efficiency and operational stability of such NIR OLEDs.

5 PLATINUM COMPLEX BASED BLUE EMITTERS

5.1 Background

Comparing with traditional inorganic luminescent materials, organic emitters possess the unique morphological and optoelectronic properties, enabling the compatibility with cheap, flexible substrates, and low-cost fabrication. Blue organic emitters have become the bottleneck of their future development in full-color display and solid lighting applications due to their relatively low efficiency and unsatisfactory operational stability.[13, 143] To now, red and green phosphorescent emitters have become promising emitter candidates for commercialized red and green OLEDs due to their capability of realizing high efficiency and superior operational stability in device settings. Blue emitters still remain a big challenge in achieving satisfactory color quality, as well as high efficiency and simultaneous operational stability. That is largely because blue emission requires a much wider bandgap, i.e., HOMO-LUMO gap, of the emitting molecules, adding to the difficulty of molecular design of ligand molecules. Moreover, the processes of TTA and TPQ occurring on blue phosphorescent emitters could lead to higher energy hot excitons or polarons, inducing more severe chemical bond dissociation and thereby causing an expedited device degradation.[33, 143]

To meet the color gamut requirement of full-color display, blue phosphorescent emitters with high color quality are highly desired. Based on the definition by National Television System Committee (NTSC), the CIE coordinates of deep-blue emission should fall in (0.14, 0.08).[22, 144] However, it is extremely difficult to achieve CIE_y below 0.1 due to the broad or pronounced vibronic progression emission characteristics of many phosphorescent metal complexes. Recently, square planar Pt(II) and Pd(II)

complexes based blue emitters have made encouraging progress by coming up with various strategies to either shift the emission into more blue region or narrow down the emission bandwidth.

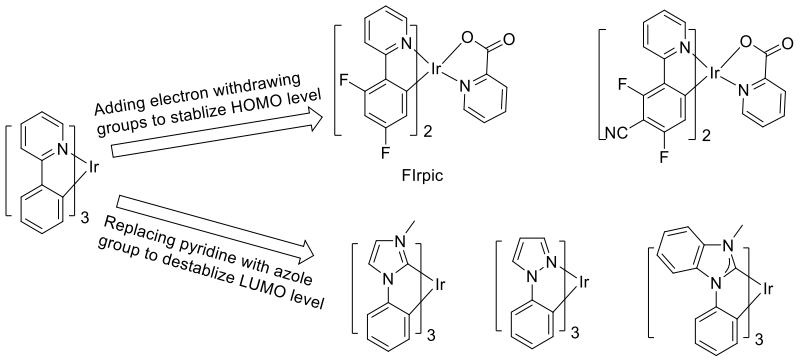

Figure 5.1 Color-tuning strategy for the development of blue emitters.[21]

Since the lowest triplet energy of phosphorescent emitters derives from mixed excited states involving both ligand-centered π-π^* and MLCT transitions, a widely used approach to obtain the blue emission is based on the modification of the frontier orbitals of the ligand. To be specific, either destabilizing the lowest unoccupied molecular orbital (LUMO) or stabilizing the highest occupied molecular orbital (HOMO) could effectively widen the bandgap and thereby correspondingly increasing the triplet energy.[21] The best-known green-emitting complex *fac*-[Ir(ppy)$_3$] was adopted to illustrate the color tuning strategies, as shown in Figure 5.1. Firstly, it has been demonstrated that the HOMO level of *fac*-[Ir(ppy)$_3$] can be stabilized by adding electron withdrawing groups, such as cyano unit, fluoro, etc., on its phenyl group. A Ir(III) complex named FIrpic, by introducing two electron withdrawing F atoms onto the phenyl ring, achieved a significant blue emission at 474 nm compared to the green emission of *fac*-[Ir(ppy)$_3$] at 510 nm.[145] However, the utilization of fluorine atoms may cause molecular degradation upon excitation during device operation, which poses challenges in

developing stable emitters.[146] Similarly, another approach has been developed by destabilizing the LUMO level via replacing pyridine ring with azole group. Tamayo et al. reported a emitter of *fac*-tris(phenylpyrazolyl)iridium(III), showing a emission peak at 414 nm at 77 K.[147] Holmes et al. synthesized a phosphorescent emitter *fac*-tris(phenyl-methyl-benzimidazolyl)iridium(III) which displayed deep-blue electroluminescent emission at 389 nm.[148]

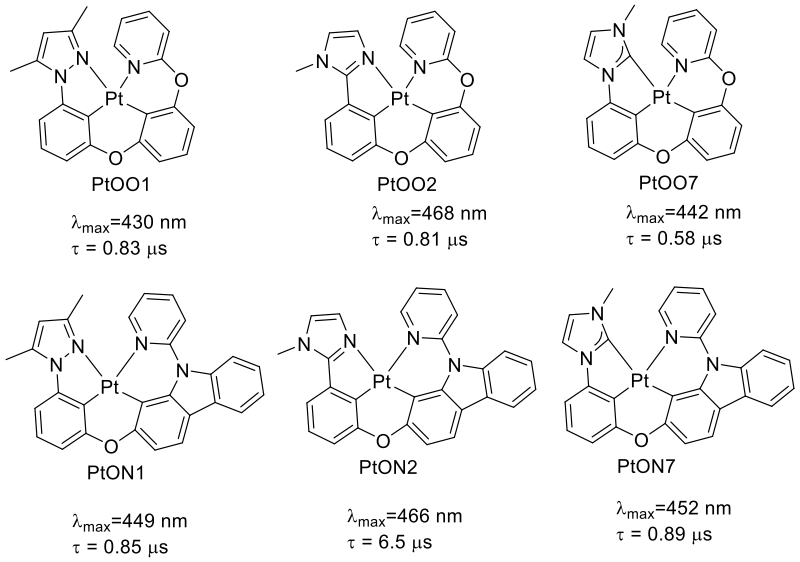

Figure 5.2 Molecular structure of selected tetradentate Pt(II) based phosphorescent blue emitters.

Through meticulous molecular design, tetradentate Pt(II) complexes can also achieve close to unity PL quantum yield and short luminescent lifetime in the range of microseconds, both of which are comparable to Ir complexes.[20, 149] Moreover, strategies utilized to tune the emission of Ir(III) complexes also apply to Pt(II) complexes. As shown in Figure 5.2, for PtOO1 and PtOO2, pyrazole and imidazole groups are adopted to destabilize the LUMO level, resulting in emissions peaking at 430 and 468 nm at room temperature, respectively.[149]. Additionally, N-heterocyclic

carbenes (NHCs) are considered one of promising chemical groups to shorten the emission wavelength due to the strong σ-donating character of the carbene carbon. A Pt(II) complex consisting of NHCs, i.e., PtON7, demonstrated a blue emission at 452 nm and a maximum external device efficiency (EQE) of 23.7%.[150]

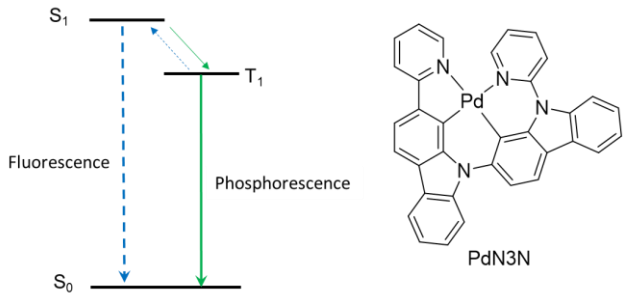

Figure 5.3 Schematic illustration of energy transfer of a Pd(II) complex, PdN3N, which can harvest both triplet and "blue" singlet excitons.[24]

Besides, another color tuning strategy, i.e., mixing thermally activated fluorescence with phosphorescence of the phosphorescent emitter, was proposed by Li and coworkers.[24, 93] As shown in Figure 5.3, a Pd(II) based phosphorescent complex named PdN3N harvested both triplet excitons and "blue" singlet, the latter of which was enabled by thermally activated RISC from excited triplet to singlet emission partially.[24] As temperature increases, an side-band emission at shorter wavelength range of 480-510 nm appeared relative to the 77 K emission at 522 nm. Moreover, a PdN3N device fabricated in a known stable structure demonstrated a remarkable device operational lifetime of LT_{90} at over 20,000 h at a luminescence of 100 cd m^{-2}.

A third strategy is improving the spectral purity by designing novel phosphorescent emitters with narrow-band emission spectrum. However, the majority of organic emissive materials exhibit broad emission with full-width at half-maximum (FWHM) ranging from 40 to70 nm, which largely compromise the color purity in display

and consequently reduce outcoupling efficiency in resonant microcavities and enhance the power consumption.[20, 22, 151]

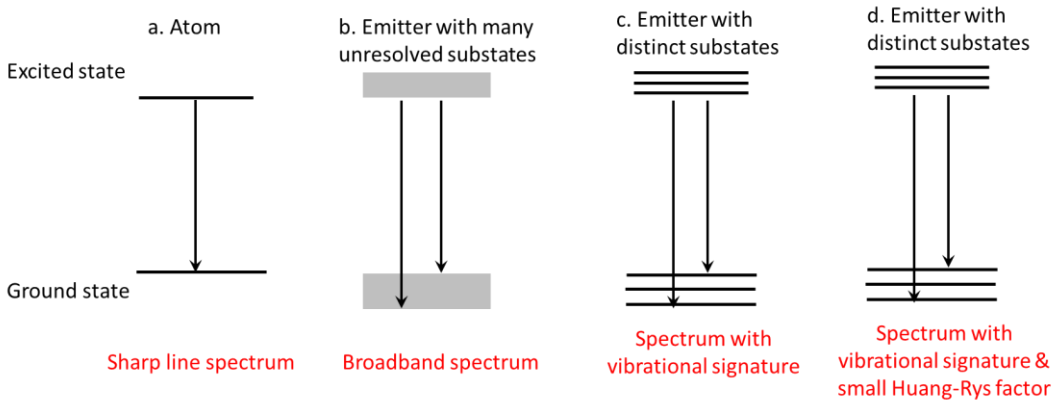

Figure 5.4 Emission spectral shape characteristic of various types of emitters.[152]

As discussed in chapter 1, the emission spectral shape and bandwidth of phosphorescent emitters are mainly determined by the properties of the lowest excited state and ground state. Luminescence of phosphorescent Ir(III), Pt(II) and Pd(II) complexes originates from the lowest triplet excited state (T1) which is typically composed of ^{3}LC and ^{1}MLCT/^{3}MLCT characters. As show in Figure 5.4b, if majority of T1 is originated from ^{1}MLCT/^{3}MLCT character, emitters typically exhibit broad Gaussian-shape emission, whereas the emission dominated by ^{3}LC character likely shows strong vibronic signature (Figure 5.4c). However, if an emitter has a rigid molecular structure with a single-dominant vibrational stretch, it will show an emission spectrum with more defined vibronic features, as depicted in Figure 5.4d.[152]

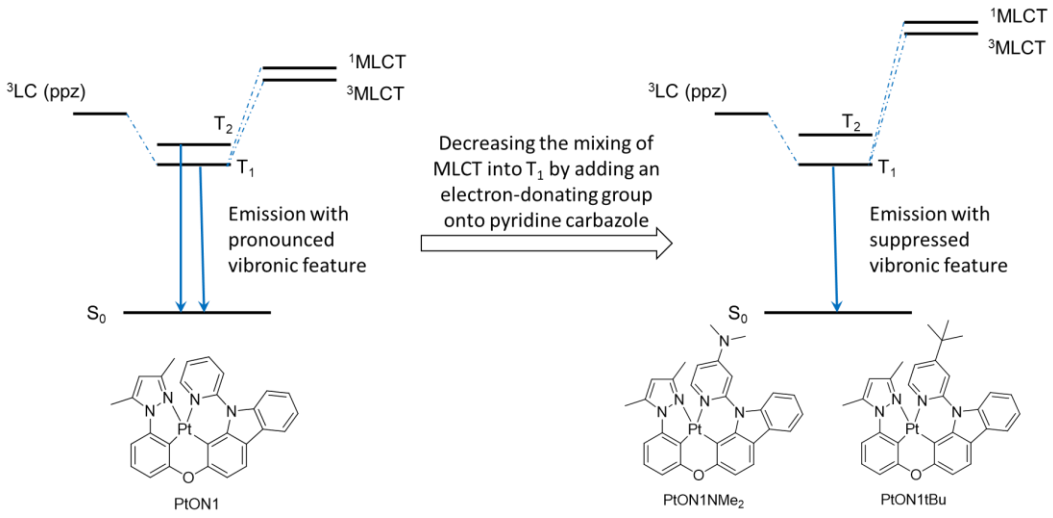

Figure 5.5 Schematic illustration of the strategy to tune the emission spectral bandwidth of PtON1.[86]

Li and coworkers has reported a series of tetradentate cyclometalated Pt(ppz-O-CbPy-R), where ppz and CbPy stand for phenyl-pyrazole and carbazole-pyridine respectively, and their emission spectral shape and bandwidth can be tuned by alerting substituents on the pyridyl moieties[86]. As described in Figure 5.5, PtON1 exhibited broad and dual emission peaks at 454 nm and 478 nm, which likely originated from a mixed ^{3}LC state of ppz moiety and ^{1}MLCT/^{3}MLCT state of metal ion and CbPy component, respectively, and the latter one was thermally accessible at elevated temperature. Results indicated spectral bandwidth can be effectively tuned by adjusting the ^{1}MLCT/^{3}MLCT state based on modification of CbPy component. By adding an electron donating group (-NMe_2) to the 4-position of pyridyl ring, a Pd(II) complex named PtON1NMe_2 demonstrated a much narrowed emission spectra peaking at 440 nm with a drastically suppressed vibronic peak. In contrast, by introducing an electron-withdrawing group of carbazole (Cz) to the same position of pyridyl ring, PtON1-Cz showed a totally different emission spectral shape, i.e., broad spectral bandwidth and

redshifted emission at 496 nm. That is largely because electron donating group of -NMe_2 destabilized the energy level of ^{1}MLCT/^{3}MLCT, resulting in less ^{1}MLCT/^{3}MLCT character in T1 state, whereas electron-withdrawing group of Cz decreased the energy level of ^{1}MLCT/^{3}MLCT state, resulting in a larger portion of ^{1}MLCT/^{3}MLCT character in the emission at room temperature.

In this chapter, various approaches are explored to develop blue phosphorescent emitters. A series of Pt(II) complexes, divided into three groups, were designed and synthesized, and their photophysical and electrochemical properties were carefully investigated. From the perspective of stability, imidazole group as a primary element was selected to incorporate into the ligand molecular design. Molecular modifications, including altering conjugation system and introduction of electron donating/withdrawing groups, were carried out on ligand molecules, which aimed at tuning emission properties, such as emission energy and spectral shape etc.

5.2 Experimental Section

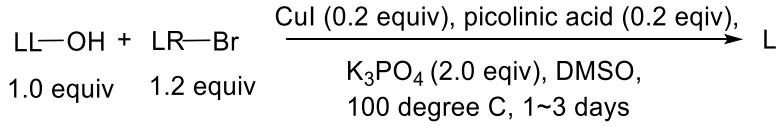

General synthetic method of the ligand L: LL-OH (1.0 eq), LR-Br (1.2 eq), CuI (0.2 eq), picolinic acid (0.2 eq) and K_3PO_4 (2.0 eq) were added to a dry flask equipped with a magnetic stir bar. The reaction system was evacuated and backfilled with nitrogen. The evacuation and backfill procedure were repeated for three times in total. Then solvent of DMSO (~1 M) was added under the protection of nitrogen. The mixture was under N_2 protection and stirred in an oil bath at a temperature of 100 ^{o}C for 1-3 days. Then reaction system was cooled down to ambient temperature and extracted with ethyl

acetate. The solvent was removed under reduced pressure, and the residue was purified through column chromatography on silica gel or Al_2O_3 using hexane/ethyl acetate as eluent to obtain the desired product ligand L.

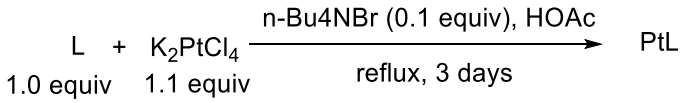

General synthetic method of the final product PtL: L (1.0 eq), K_2PtCl_4 (1.1 eq) and n-Bu_4NBr (0.1 eq) were added to a dry flask equipped with a magnetic stir bar. The reaction system was evacuated and backfilled with nitrogen. The evacuation and backfill procedure were repeated for three times in total. Then solvent of acetic acid (0.017 M) was added under the protection of nitrogen. Then the mixture was heated to reflux in an oil bath and stirred for 3 days under N_2 protection. Then the reaction system was cooled to ambient temperature and the solvent removed under reduced pressure. Then the solid was purified through column chromatography on silica gel or Al_2O_3 using dichloromethane/hexane as eluent to afford the desired final product of PtL.

5.3 The First Group of Imidazole-Based Pt(II) Complexes

Three groups of imidazole-based phosphorescent Pt(II) complexes were designed and synthesized. As shown in Figure 5.6, the first group of Pt(II) complexes share the same skeletal structure, i.e. conjugated phenyl-imidazole and pyridyl-carbazole fragments linked by an oxygen atom. Taking PtON2-P as a starting point, aza atoms were added on the phenyl ring in the imidazo[1,2-f]phenanthridine moiety to form pyridyl groups, yielding PtON2-Py2 and PtON2-Py5. Moreover, the newly formed pyridyl groups can potentially enhance the electrochemical stability due to their reduction functionality. Considering the potential formation of molecular aggregates, bulky groups of mesityl and

phenyl were introduced onto the imidazole ring to suppress the intermolecular interactions. Thus, in the first group, 6 imidazole-based Pt(II) complexes, i.e., PtON2-Py2, PtON2-Py5, PtON2-PP, PtON2-Py5-M, and PtON2-Py5-MtBu, were developed.

5.3.1 Material Preparation

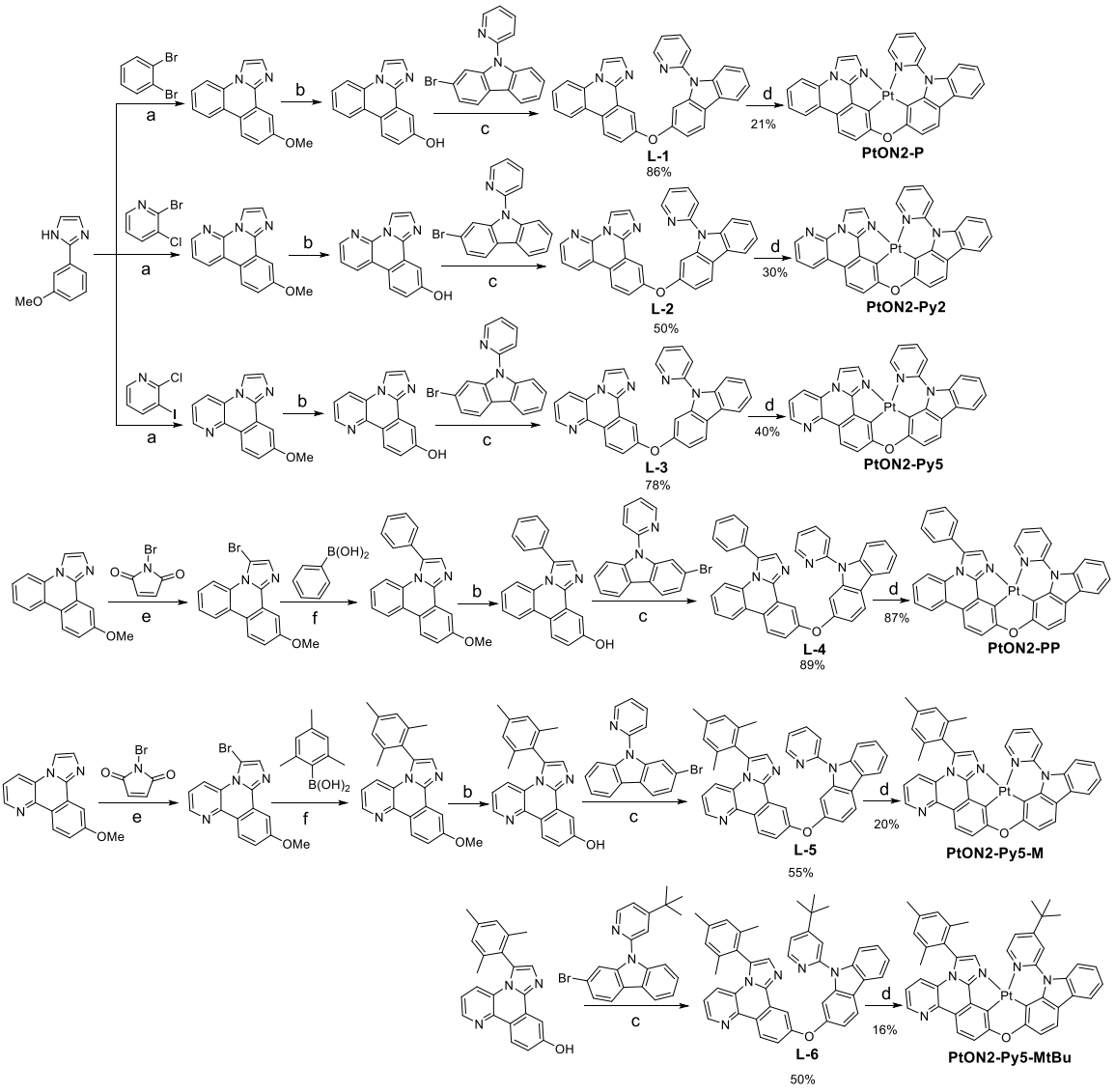

Figure 5.6 Synthetic routes of PtON2-P, PtON2-Py2, PtON2-Py5, PtON2-PP, PtON2-Py5-M, and PtON2-Py5-MtBu. Reagents and conditions: (a) $Pd(PPh_3)_4$ (0.1 equiv), Xantphos (0.1 equiv), K_2CO_3 (3.0 equiv), DMF, 140 ℃, overnight. (b) HBr, HOAc, reflux. (c) CuI (0.2 equiv), picolinic acid (0.2 eqiv), K_3PO_4 (2.0 eqiv), DMSO, 100 ℃, 1~3 days. (d) K_2PtCl_4 (1.2 equiv), n-Bu_4NBr (0.1 equiv), HOAc, reflux, 3 days.

(e) DMF, room temperature. (f) $Pd_2(dba)_3$ (0.25 equiv), S-phos (1 equiv), K_3PO_4 (4 equiv), toluene, reflux. Note: the yield is one-step reaction yield.

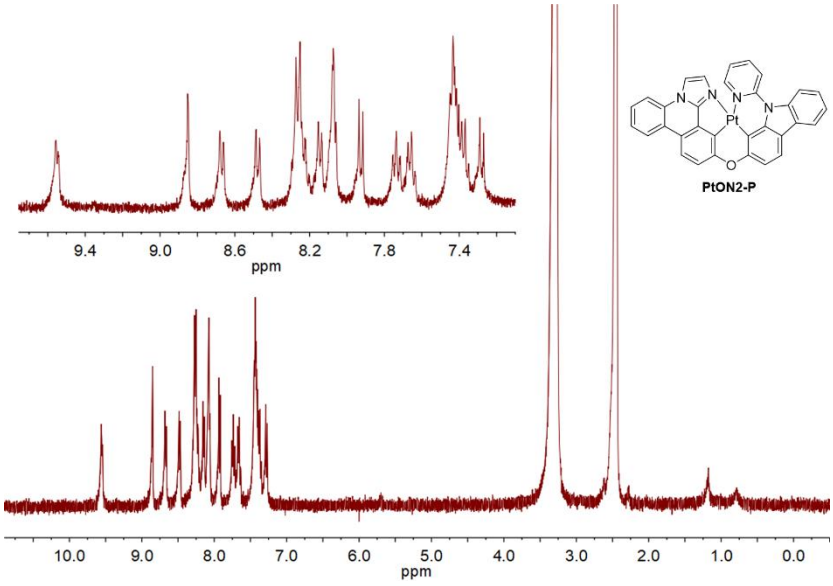

Figure 5.7 ^{1}H NMR spectrum of PtON2-P (DMSO-*d*6).

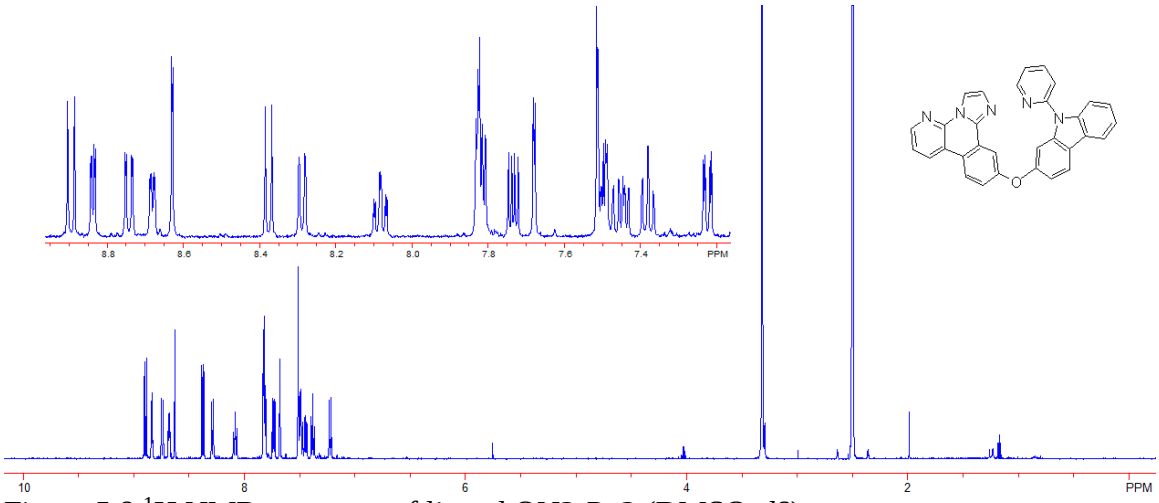

Figure 5.8 ^{1}H NMR spectrum of ligand ON2-Py2 (DMSO-*d*6).

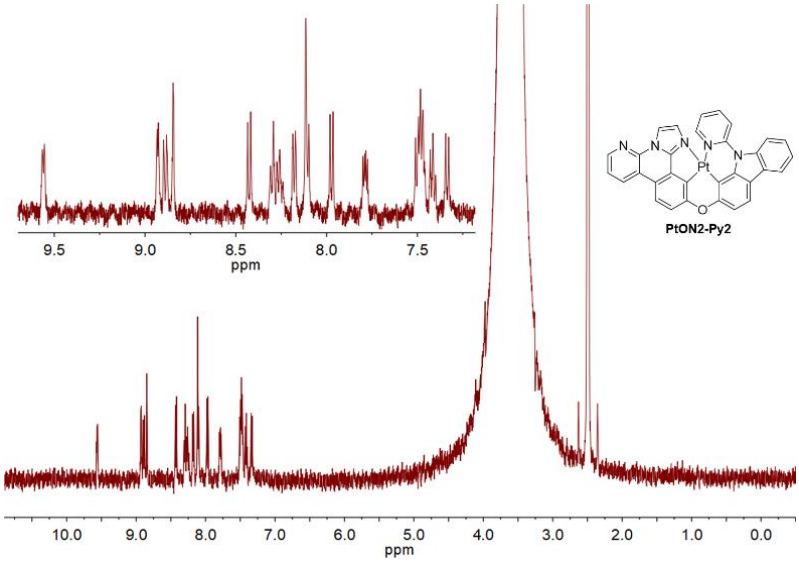

Figure 5.9 ^{1}H NMR spectrum of PtON2-Py2 (DMSO-*d*6).

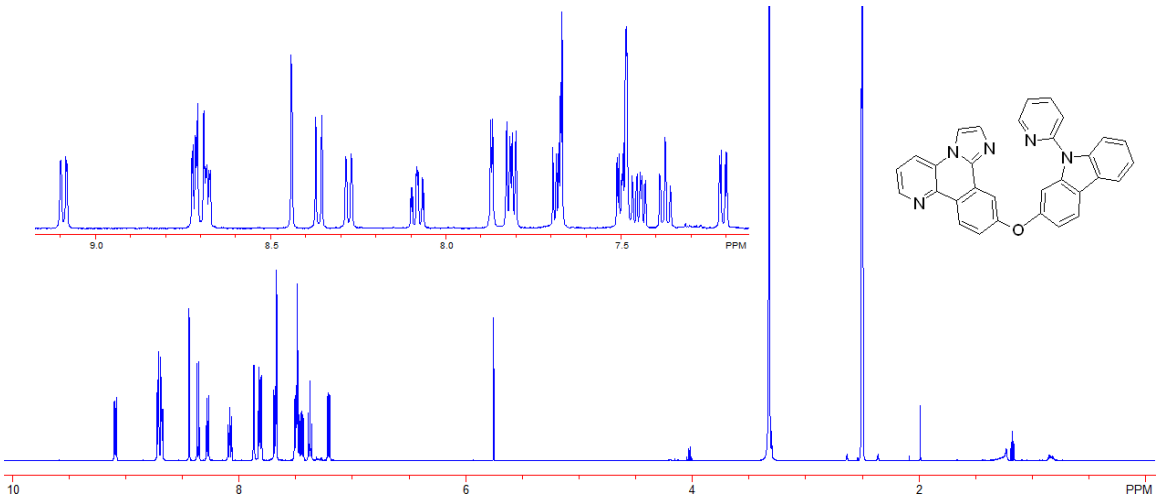

Figure 5.10 ^{1}H NMR spectrum of ligand ON2-Py5 (DMSO-*d*6).

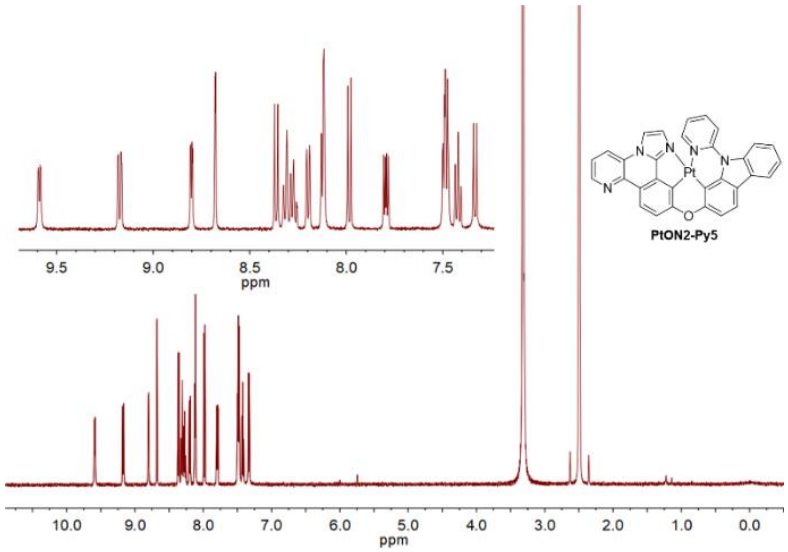

Figure 5.11 ^{1}H NMR spectrum of PtON2-Py5 (DMSO-*d*6).

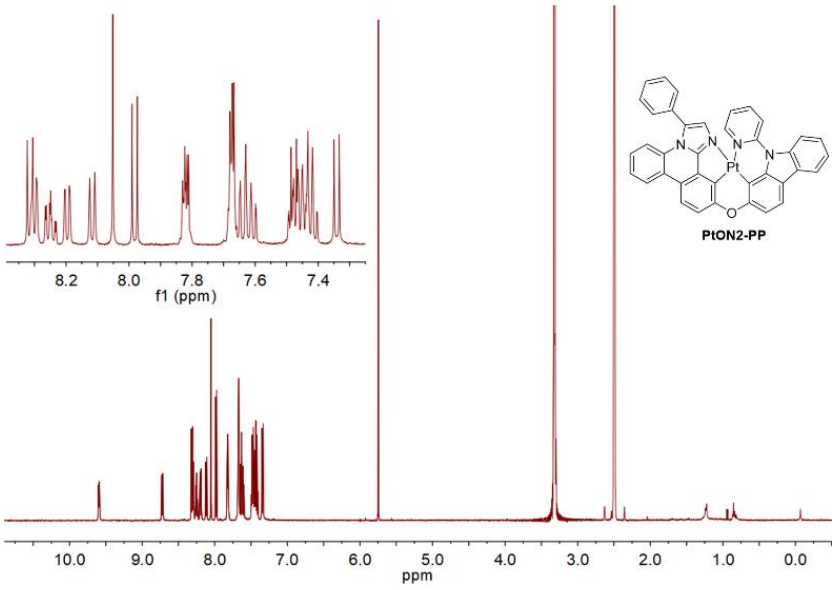

Figure 5.12 ^{1}H NMR spectrum of PtON2-PP (DMSO-*d*6).

5.3.2 Photophysical Properties

Absorption spectra of PtON2-P, PtON2-Py2, PtON2-Py5, and PtON2-PP are presented in Figure 5.13. They exhibited quite similar emission patterns with strong absorption bands below 360 nm which are assigned to $^{1}\pi$-π^{*} ligand centered (LC) transitions. The weak absorption band between 360 and 440 nm is the metal-to-ligand

charge transition (MLCT). The photoluminescent (PL) emission spectra of these complexes are displayed in Figure 5.14. At 77 K, they showed similar emission peaks in the range of 445-458 nm, indicating similar energy level of T1 state. However, their emission spectral shapes are different, and PtON2-P showed a very sharp emission with largely suppressed vibronic features compared to the other three complexes. That is possibly because the addition of phenyl ring or aza atoms enhanced the substates of ground and/or excited states. The density functional theory (DFT) calculations of PtON2-P, PtON2-Py2 and PtON2-Py5 (Figure 5.15) also indicated that the LUMOs of PtON2-Py2 and PtON2-Py5 were located on both pyridyl orbitals compared to the PtON2-P. At room temperature, red-shifted emissions were observed for PtON2-P and PtON2-PP with a red-shift value of 5 and 10 nm, respectively. As observed, there was no obvious emission peak shift for PtON2-Py2 and PtON2-Py5 at room temperature.

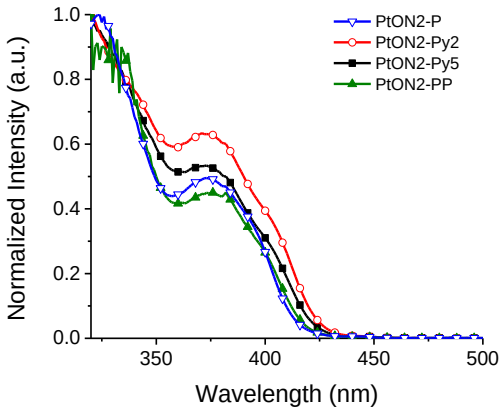

Figure 5.13 Room-temperature absorption spectrum of PtON2-P (open triangles), PtON2-Py2 (open circles), PtON2-Py5 (solid squares), and PtON2-PP (solid triangles) in dichloromethane (DCM).

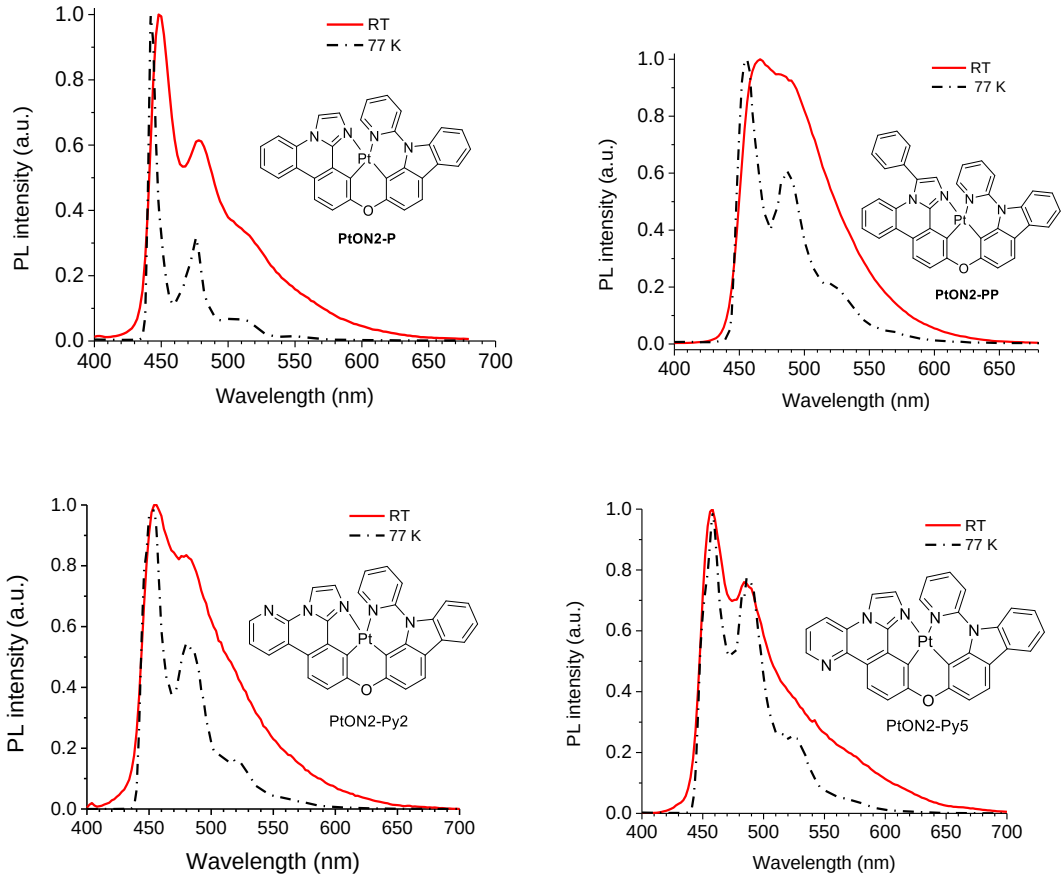

Figure 5.14 Photoluminescent (PL) spectra at room temperature and 77 K of PtON2-P, PtON2-PP, PtON2-Py2, and PtON2-Py5 with chemical structures in inset.

Table 5.1 Photophysical properties of PtON2-P, PtON2-PP, PtON2-Py2, PtON2-Py5, PtON2-Py5-M, and PtON2-Py5-M-tBu.

Complex	Emission @ 77 K		Emission @ RT	
	λ_{max} (nm)	FWHM (nm)	λ_{max} (nm)	FWHM (nm)
PtON2-P	445	7	450	47
PtON2-PP	456	46	466	74
PtON2-Py2	454	44	456	69
PtON2-Py5	458	51	458	59
PtON2-Py5-M	458	15	464	55
PtON2-Py5-M-tBu	458	43	464	56

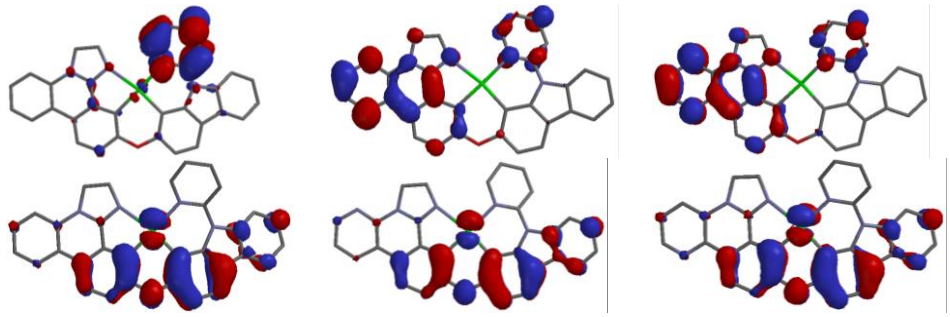

PtON2-P PtON2-Py2 PtON2-Py5

Figure 5.15 Density functional theory calculations of the orbit density for the HOMOs (bottom) and LUMOs (top) of PtON2-P, PtON2-Py2, and PtON2-Py5.

Moreover, an interesting optical phenomenon was observed for both PtON2-Py2 and PtON2-Py5. As shown in Figure 5.16, significantly narrowed room temperature PL spectra of PtON2-Py2 and PtON2-Py5 were detected at a relatively low concentration, and their first major vibronic transition relative to the dominant emission peak largely reduced, indicating that the vibronic transitions of PtON2-Py2 and PtON2-Py5 are likely concentration-dependent. More research is needed to reveal the emission mechanism of this emission spectral narrowing phenomenon.

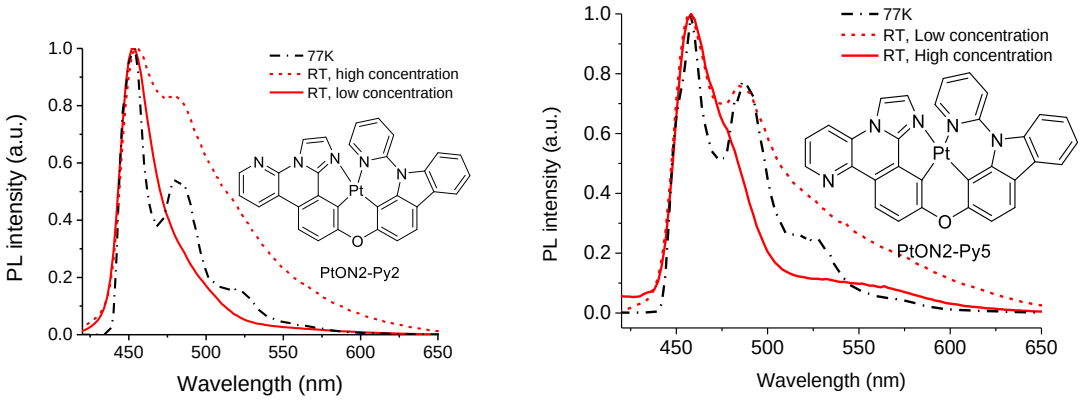

Figure 5.16 Photoluminescent (PL) spectra at room temperature and 77 K of PtON2-Py2 and PtON2-Py5 with different concentration.

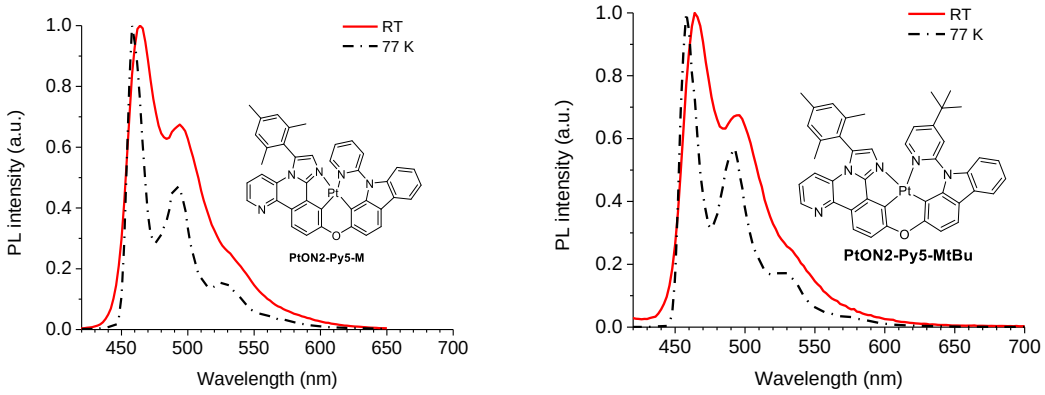

Figure 5.17 Photoluminescent (PL) spectra at room temperature and 77 K of PtON2-Py5-M and PtON2-Py5-MtBu with chemical structures in inset.

To potentially suppress formation of molecular aggregates and narrow the emission spectra, PtON2-Py5 was modified with the addition of bulky mesityl and t-butyl chemical groups, yielding two new complexes, i.e., PtON2-Py5-M and PtON2-Py5-MtBu. At 77 K, both of them showed same emission peaks at 458 nm as PtON2-Py5, but drastically suppressed vibronic features, as shown in Figure 5.17. At room temperature, they exhibited nearly identical emission with same emission peaks at 464 and similar FWHM value of around 55 nm and vibronic progression.

5.4 The Second Group of Imidazole-Based Pt(II) Complexes

To get much narrower emission, three new PtON2-based complexes, i.e., PtON2-Cz56, PtON2-Cz56-tBu, and PtON2-Sz56-tBu were designed, and Figure 5.18 shows their synthetic routes. The structural modification mainly focused on the peripheral group of the pristine ligand ON2-P, i.e., the phenyl ring conjugated with imidazole-phenyl group, by adding Cz or Sz groups, which could enlarge the conjugation system of ligand without significantly influencing the MLCT state. This design concept is expected to tune the LC and MLCT state separately, and eventually get narrow-band emissions.

5.4.1 Material Preparation

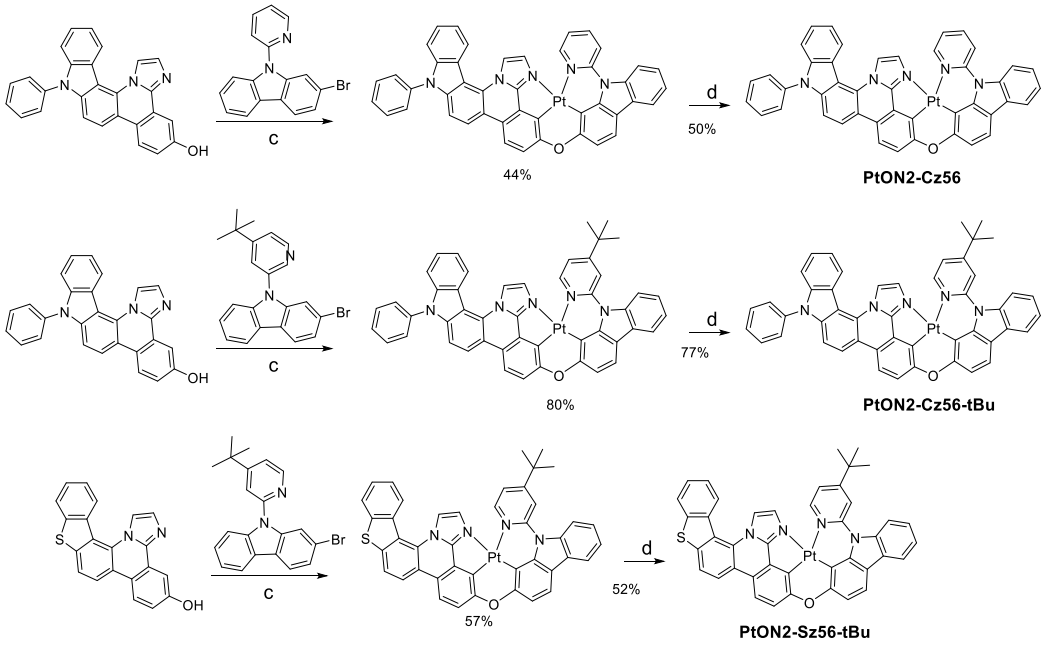

Figure 5.18 Synthetic routes of PtON2-Cz56, PtON2-Cz56-tBu, PtON2-Sz56-tBu. Note: the yield is one-step reaction yield.

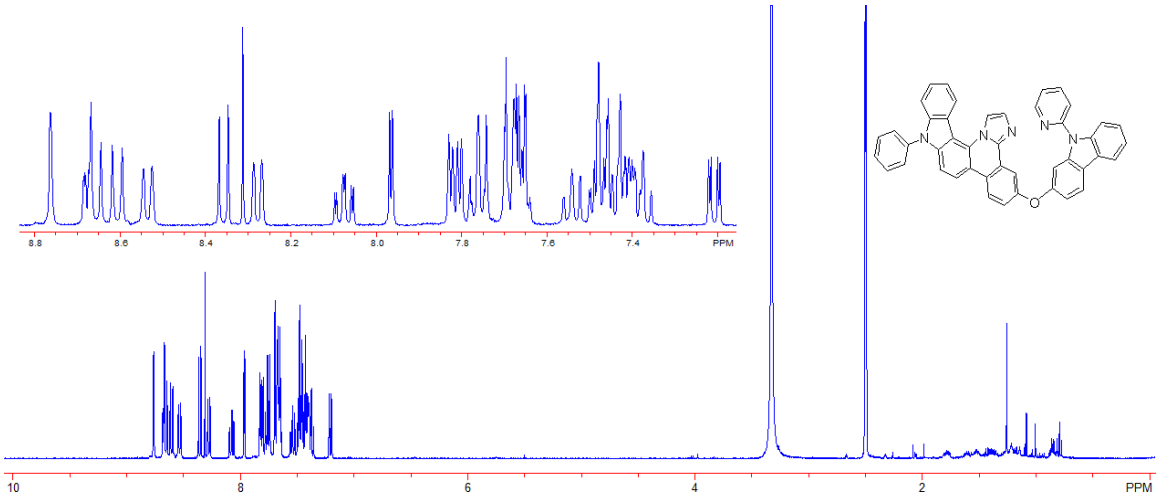

Figure 5.19 ^{1}H NMR spectrum of ligand ON2-Cz56 (DMSO-*d*6).

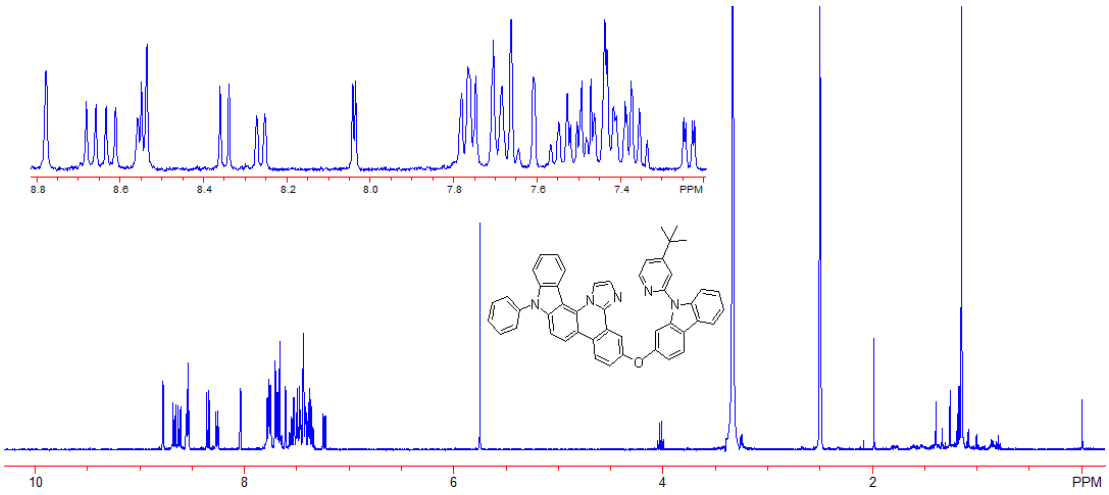

Figure 5.20 ^{1}H NMR spectrum of ligand ON2-Cz56-tBu (DMSO-*d*6).

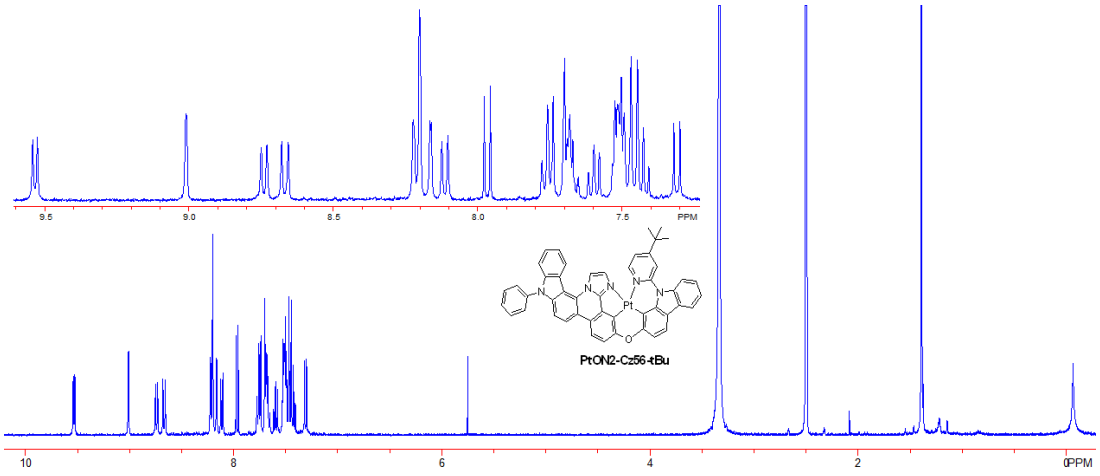

Figure 5.21 ^{1}H NMR spectrum of PtON2-Cz56-tBu (DMSO-*d*6).

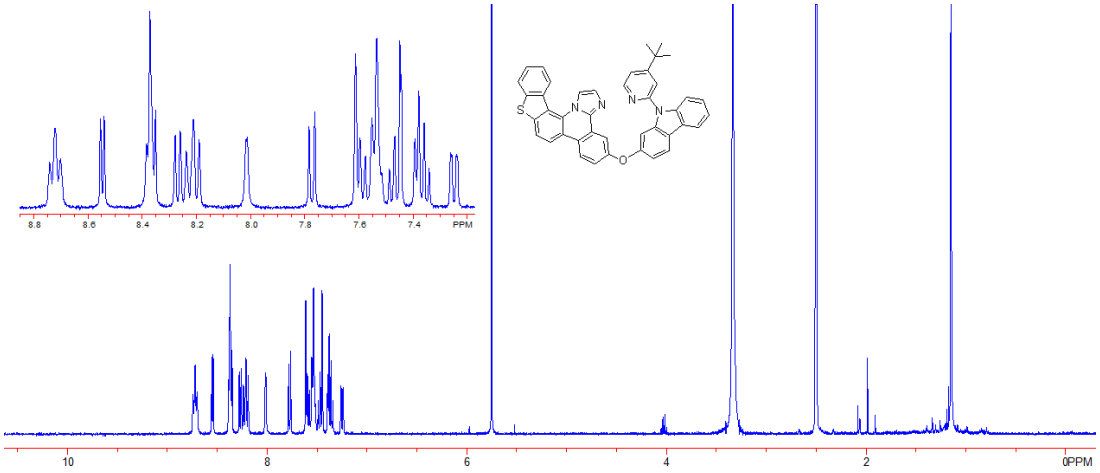

Figure 5.22 ^{1}H NMR spectrum of ligand ON2-Sz56-tBu (DMSO-*d*6).

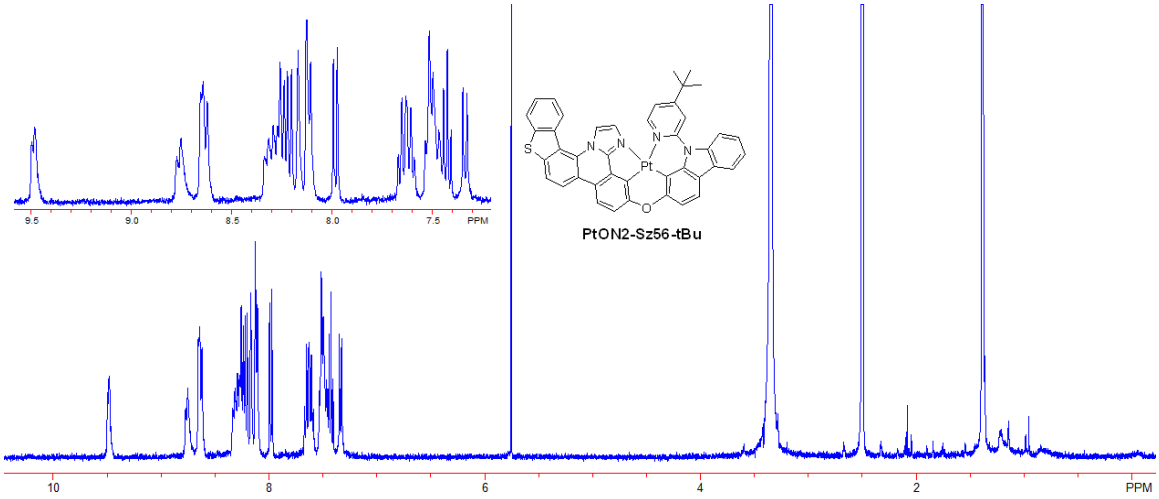

Figure 5.23 ^{1}H NMR spectrum of PtON2-Sz56-tBu (DMSO-*d*6).

5.4.2 Photophysical and Electrochemical Properties

Figure 5.24 shows the room temperature absorption spectra of PtON2-P, PtON2-Cz56, and PtON2-Sz56-tBu. These three complexes exhibited similar absorption pattern as a result of similar skeletal structure, and only vary in intensity of transition bands. The distinct strong absorption peaks between 250 and 370 nm (ε = 1.3-6.1×10^{4} M^{-1} cm^{-1}) can be assigned to $^{1}(\pi$-$\pi^*)$ transitions on the cyclometalating ligand. The weak absorption bands between 370 and 440 nm were attributed to metal-to-ligand charge transfer (^{1}MLCT). Due to the larger conjugated aromatic system, PtON2-Cz56 showed the most intense transition bands.

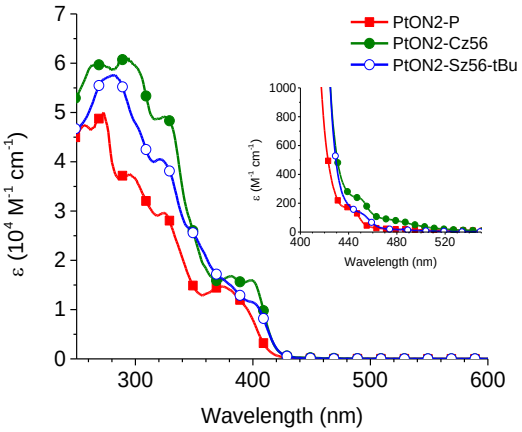

Figure 5.24 Room-temperature absorption spectrum of PtON2-P (solid squares), PtON2-Cz56 (solid circles), and PtON2-Sz56-tBu (open circles) in dichloromethane (DCM).

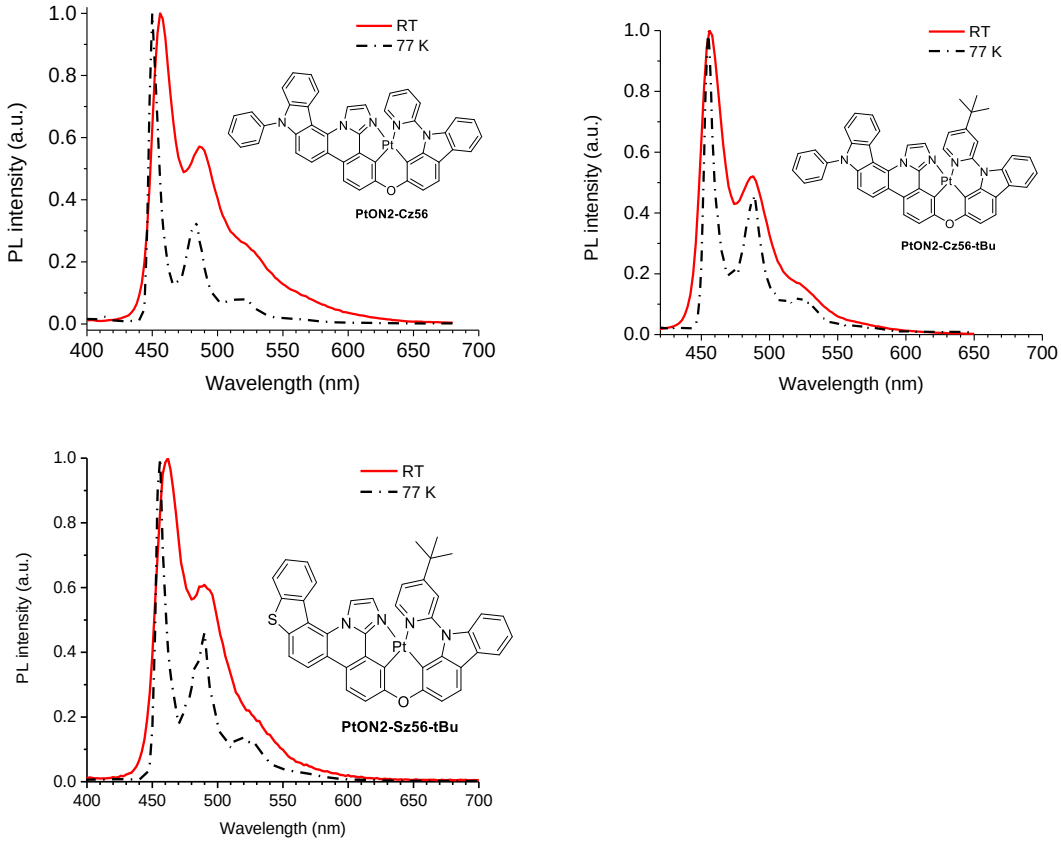

Figure 5.25 PL spectra at room temperature and 77 K of PtON2-Cz56, PtON2-Cz56-tBu, and PtON2-Sz56-tBu with chemical structures in inset.

Table 5.2 Photophysical properties of PtON2-Cz56, PtON2-Cz56-tBu, and PtON2-Sz56-tBu.

Complex	Emission @ 77 K		Emission @ RT	
	λ_{max} (nm)	FWHM (nm)	λ_{max} (nm)	FWHM (nm)
PtON2-Cz56	450	6	456	45
PtON2-Cz56-tBu	456	8	456	41
PtON2-Sz56-tBu	456	8	462	47

Photophysical properties of PtON2-Cz56, PtON2-Cz56-tBu, and PtON2-Sz56-tBu were investigated by recording their emission spectra at 77 K and room temperature, as shown in Figure 5.25 and Table 5.2. PtON2-Cz56 exhibited a sharp emission spectrum peaking at 450 nm with very pronounced vibronic features, and the FWHM is only 6 nm. At room temperature. its emission spectrum red-shifted to 456 nm with enhanced vibronic sidebands. In comparison with PtON2-Cz56, PtON2-Cz56-tBu displayed a red-shifted 77 K emission at 456 nm with relatively stronger sidebands. Interestingly, the room-temperature emission of PtON2-Cz56-tBu showed no changes in peak wavelength still at 456 nm, and slightly enhanced sidebands which were weaker than those of PtON2-Cz56. For PtON2-Sz56-tBu, it demonstrated almost identical 77 K emission to PtON2-Cz56-tBu. However, at room temperature, PtON2-Sz56-tBu emission was largely shifted to 462 nm with relatively stronger vibronic sidebands.

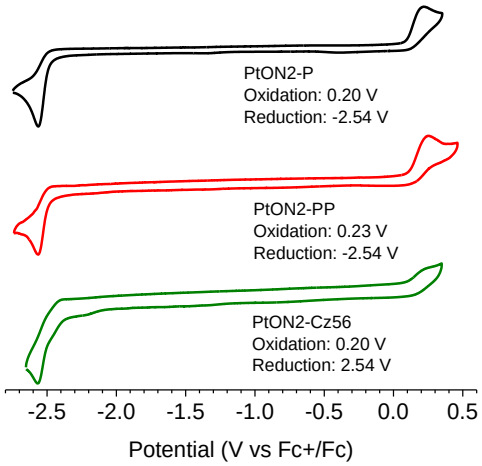

Figure 5.26 Cyclic voltammograms for PtON2-P, PtON2-PP, and PtON2-Cz56. The oxidation and reduction potentials were determined by differential pulse voltammetry in dimethylformamide versus a ferrocene internal reference.

Moreover, electrochemical property comparison among PtON2-P, PtON2-PP, and PtON2-Cz56 are provided in Figure 5.26. They showed similar values in their oxidation (0.20 - 0.23 V) and reduction potentials (-2.54 V), indicating similar HOMO and LUMO energy levels for all of them, which is consistent with their emission energy. Both the reduction and oxidation peaks of PtON2-P and PtON2-PP exhibited quasi-reversible behaviors. By comparison, PtON2-Cz56 displayed both irreversible reduction and oxidation peaks, which is likely caused by the poor solubility of PtON2-Cz56 in DMF.

5.5 The Third Group of Imidazole-Based Pt(II) Complexes

Almost all imidazole-based Pt(II) complexes from both the first and second groups showed strong vibronic sidebands, which greatly enlarged the spectral bandwidth to around 50 nm. Therefore, a third group of imidazole-based Pt(II) complexes was designed to suppress the sidebands and increase the spectral purity. The right segment of pyridyl-carbazole group utilized in the first and second groups of complexes was replaced with similar group to the right segment. As a result, a rigid and square-planar tetradentate

imidazole-based Pt(II) complexes are synthesized, and the synthetic routes are demonstrated in Figure 5.27. To prevent the potential formation of molecular aggregates, bulky mesityl or phenyl groups were added onto the imidazole ring.

5.5.1 Material Preparation

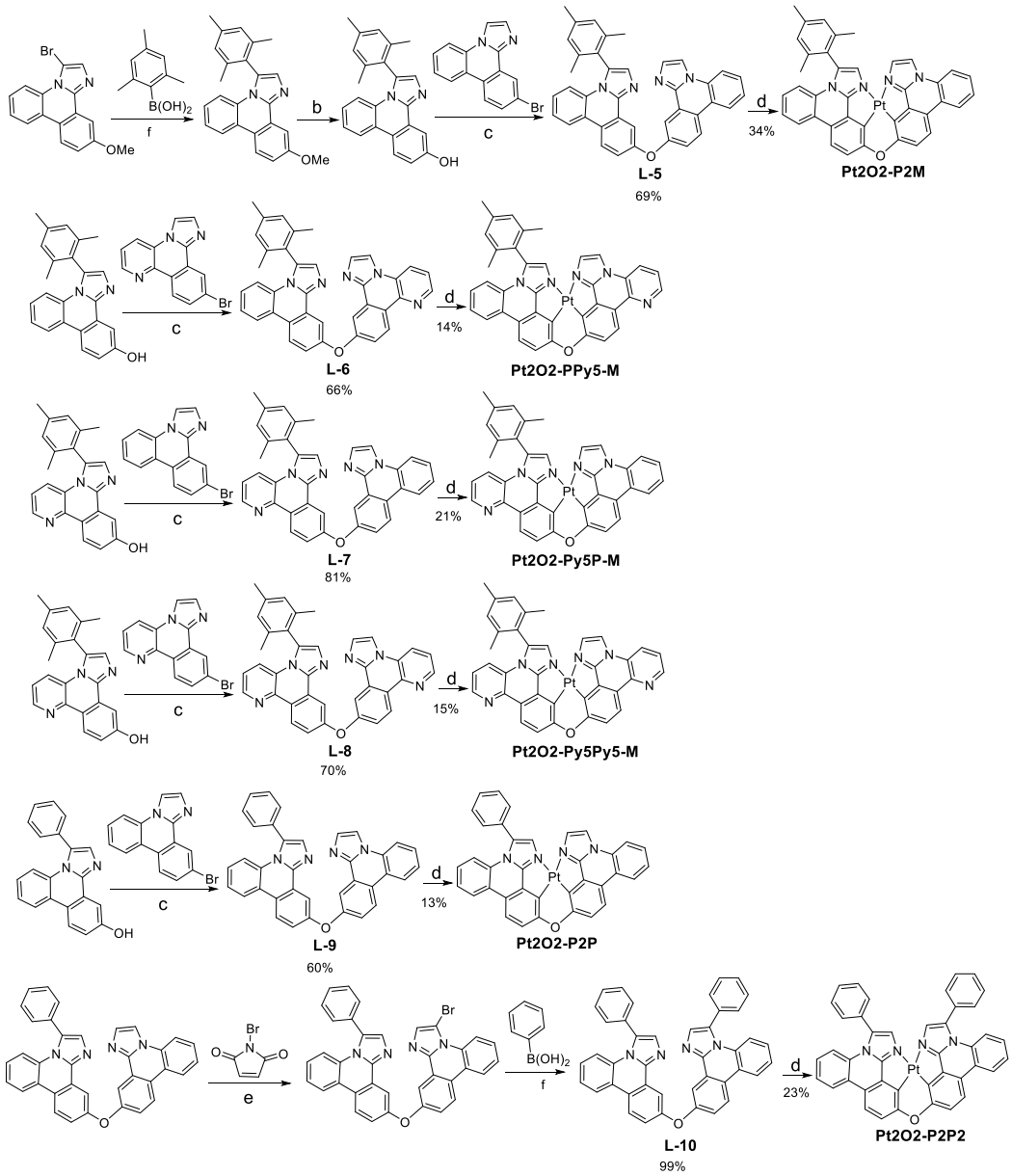

Figure 5.27 Synthetic routes of blue Pt2O2-P2M, Pt2O2-PPy5-M, Pt2O2-Py5P-M, Pt2O2-Py5Py5-M, Pt2O2-P2P, and Pt2O2-P2P2. Note: the yield is one-step reaction yield.

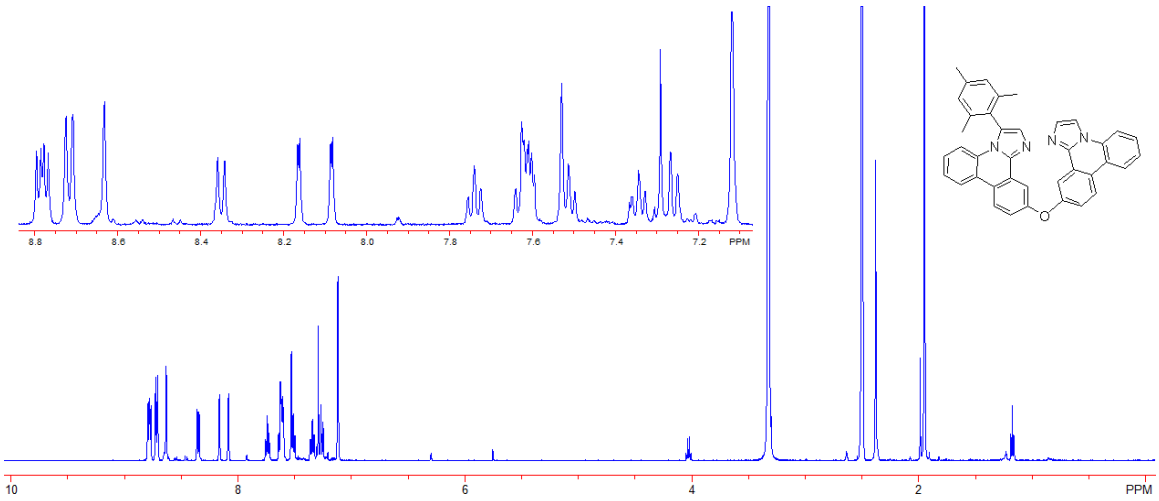

Figure 5.28 ^{1}H NMR spectrum of ligand 2O2-P2M (DMSO-*d*6).

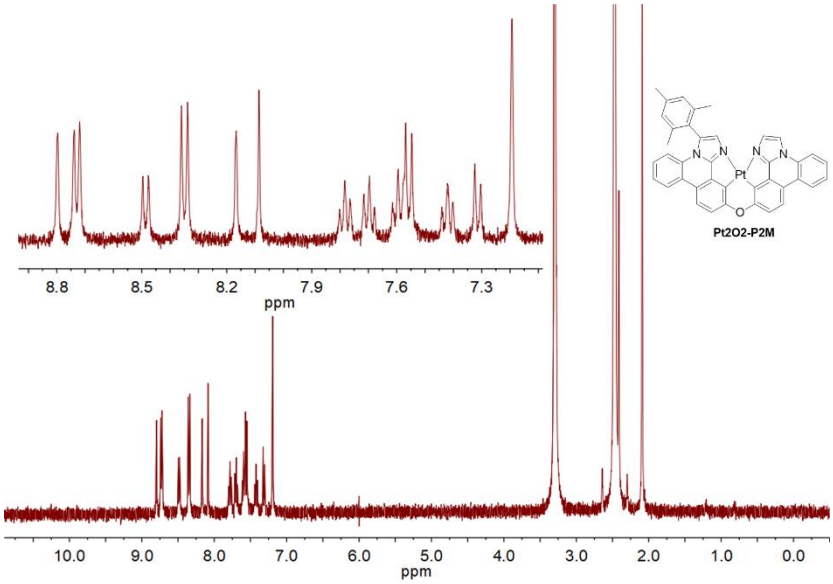

Figure 5.29 ^{1}H NMR spectrum of Pt2O2-P2M (DMSO-*d*6).

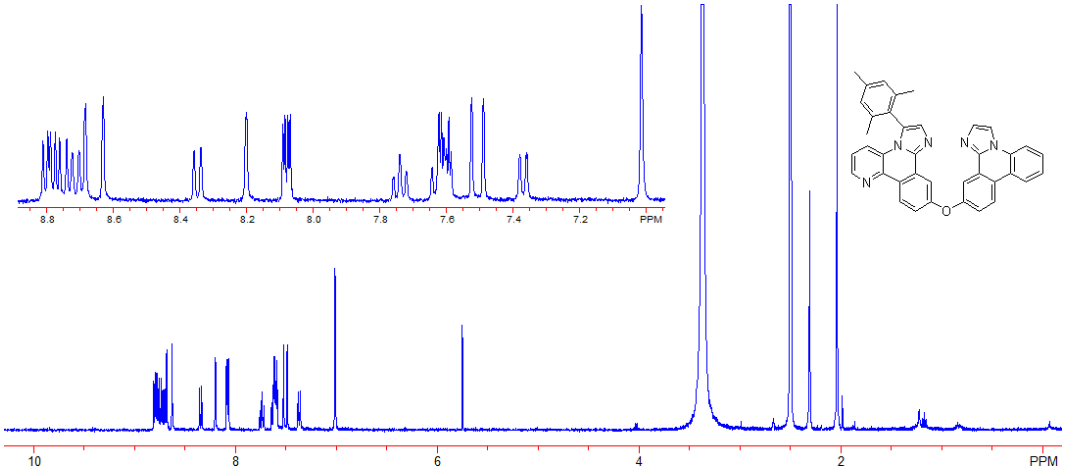

Figure 5.30 ^{1}H NMR spectrum of ligand 2O2-Py5P-M (DMSO-*d*6).

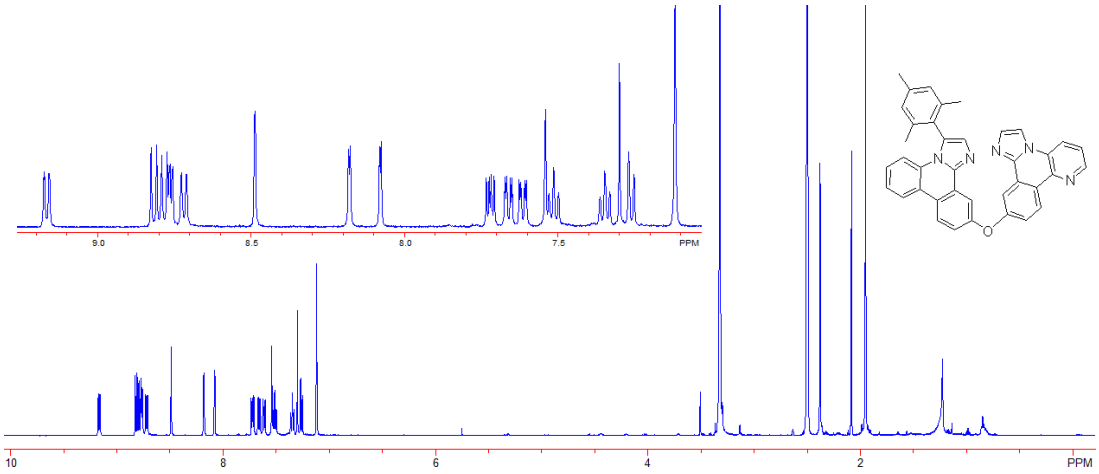

Figure 5.31 ^{1}H NMR spectrum of ligand 2O2-PPy5-M (DMSO-*d*6).

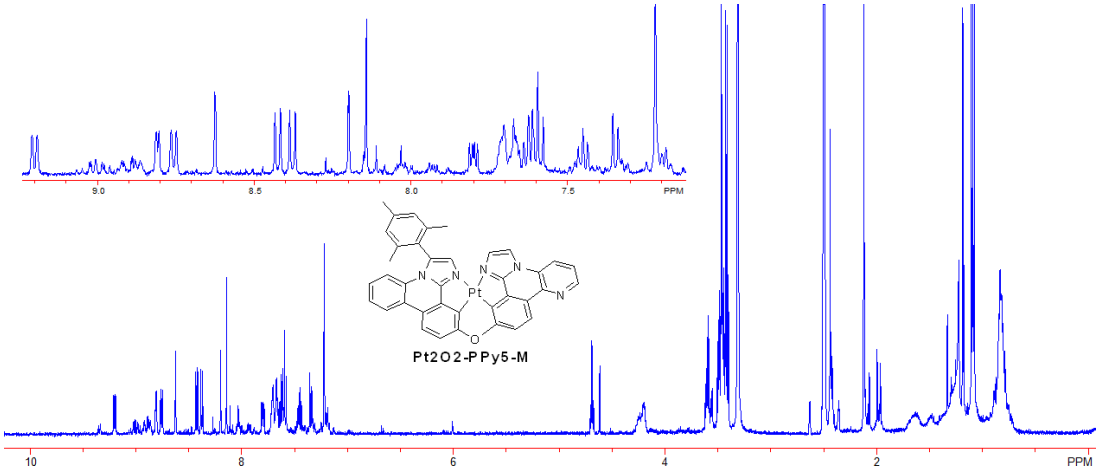

Figure 5.32 ^{1}H NMR spectrum of Pt2O2-PPy5-M (DMSO-*d*6).

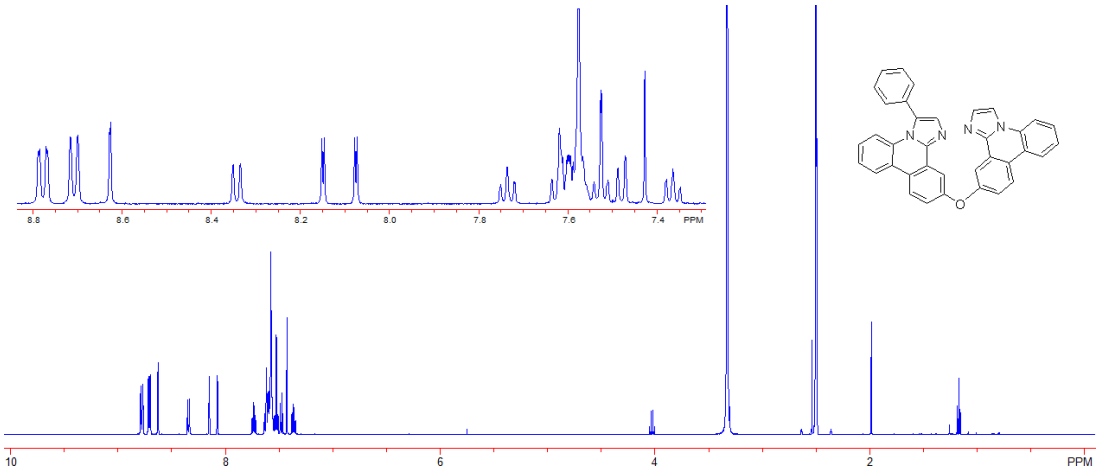

Figure 5.33 ^{1}H NMR spectrum of ligand 2O2-P2P (DMSO-*d*6).

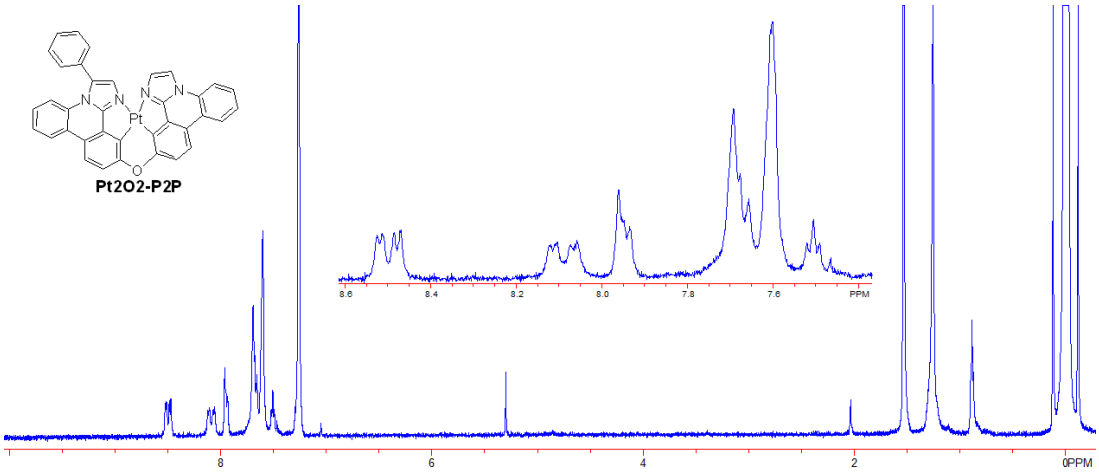

Figure 5.34 ^{1}H NMR spectrum of Pt2O2-P2P ($CDCl_3$).

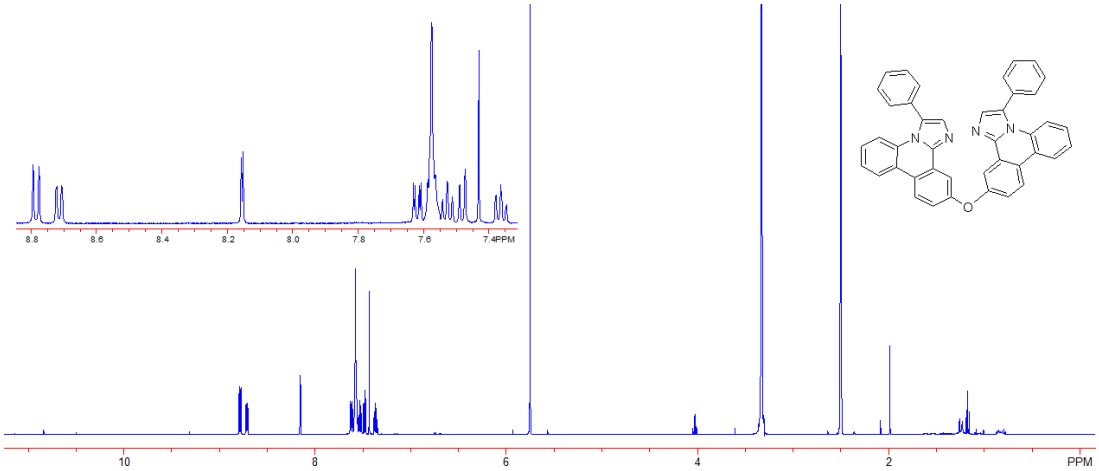

Figure 5.35 ^{1}H NMR spectrum of ligand 2O2-P2P2 (DMSO-*d*6).

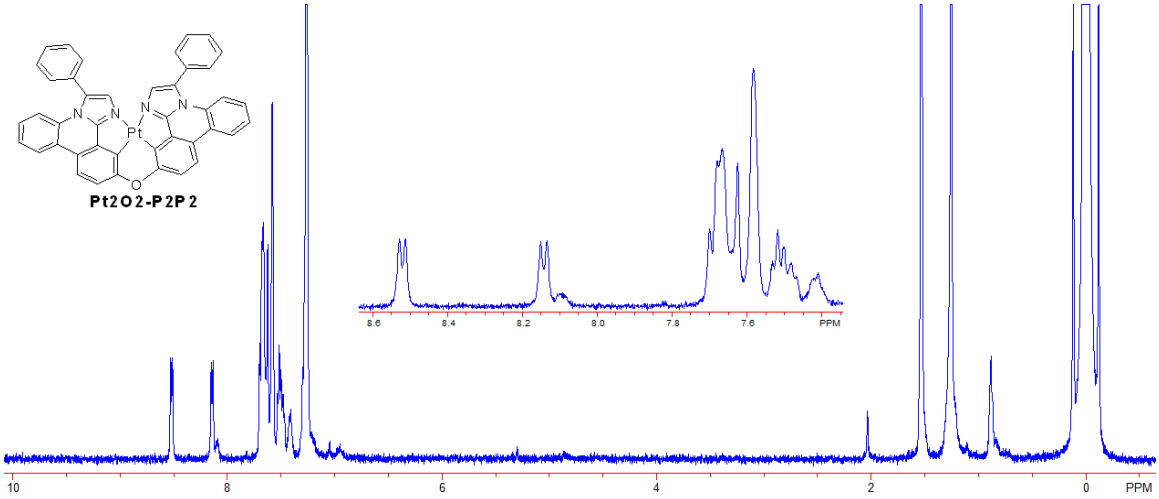

Figure 5.36 ^{1}H NMR spectrum of Pt2O2-P2P2 ($CDCl_3$).

5.5.2 Photophysical Properties

Figure 5.37 shows the room-temperature absorption spectra of selected PtON2-PP, Pt2O2-P2M, Pt2O2-P2P, and Pt2O2-P2P2 in dichloromethane (DCM). Pt2O2-P2M, Pt2O2-P2P, and Pt2O2-P2P2 exhibited different absorption patterns to PtON2-PP due to the different skeletal structures. The distinct strong absorption peaks between 250 and 370 nm (ε = 1.3-7.4×10^4 M^{-1} cm^{-1}) can be assigned to $^{1}(\pi$-$\pi^*)$ transitions on the cyclometalating ligand. The weak absorption bands between 370 and 440 nm were attributed to metal-to-ligand charge transfer (^{1}MLCT) involving both the cyclometalating ligand and the Pt ion.

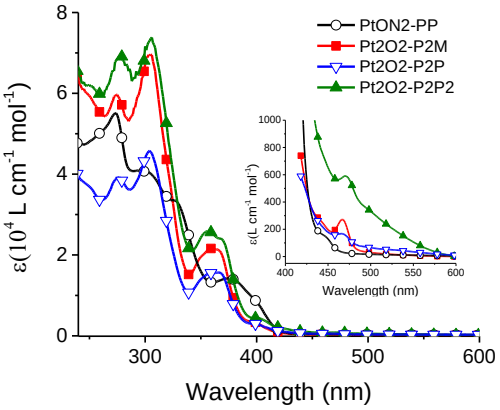

Figure 5.37 Room-temperature absorption spectrum of PtON2-PP (open circles), Pt2O2-P2M (solid squares), Pt2O2-P2P (open triangles), and Pt2O2-P2P2 (solid triangles) in dichloromethane (DCM).

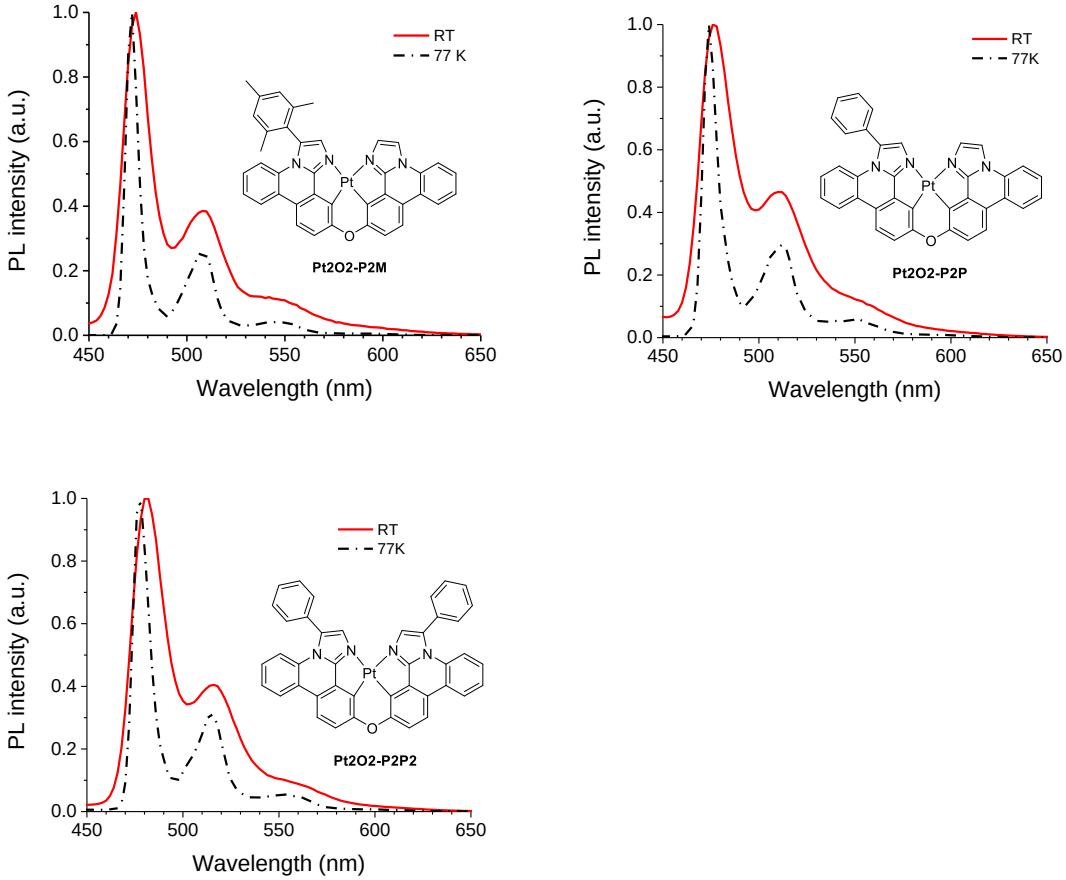

Figure 5.38 PL spectra at room temperature and 77 K of Pt2O2-P2M, Pt2O2-P2P, and Pt2O2-P2P2 with chemical structures in inset.

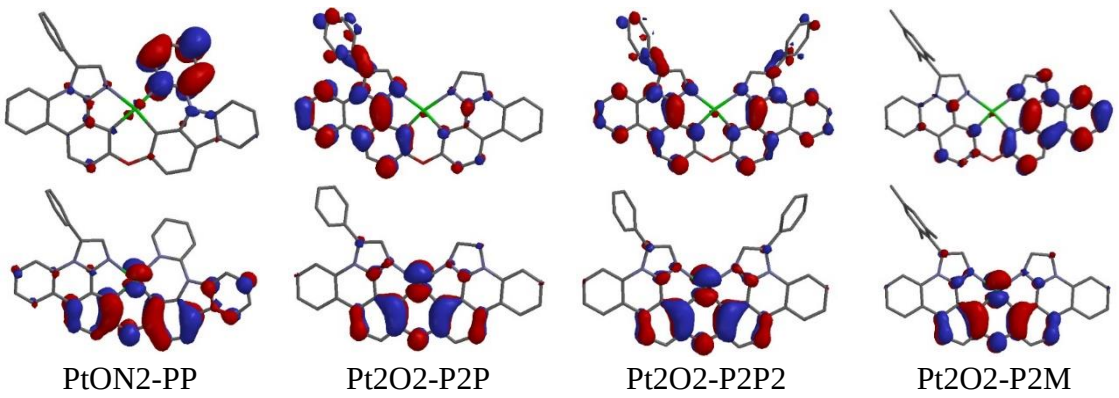

Figure 5.39 Density functional theory calculations of the orbit density for the HOMOs (bottom) and LUMOs (top) of PtON2-PP, Pt2O2-P2P, Pt2O2-P2P2, and Pt2O2-P2M.

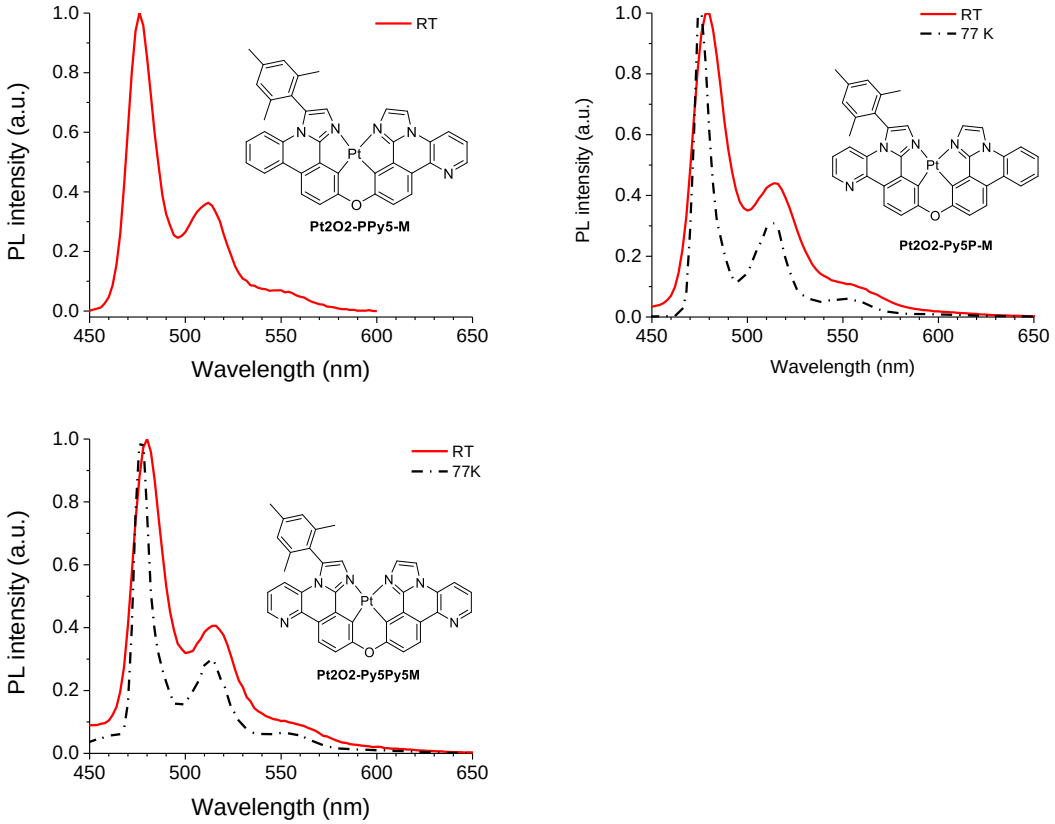

Figure 5.40 PL spectra at room temperature and 77 K of Pt2O2-PPy5-M, Pt2O2-Py5P-M, and Pt2O2-Py5Py5-M with chemical structures in inset.

Table 5.3 Photophysical properties of Pt2O2-P2M, Pt2O2-P2P, Pt2O2-P2P2, Pt2O2-PPy5-M, Pt2O2-Py5P-M, and Pt2O2-Py5Py5-M.

Complex	Emission @ 77 K		Emission @ RT	
	λ_{max} (nm)	FWHM (nm)	λ_{max} (nm)	FWHM (nm)
Pt2O2-P2M	472	8	472	16
Pt2O2-P2P	474	9	476	22
Pt2O2-P2P2	478	9	482	21
Pt2O2-PPy5-M	-	-	476	16
Pt2O2-Py5P-M	476	10	480	20
Pt2O2-Py5Py5-M	478	9	480	18

Photophysical properties of Pt2O2-P2M, Pt2O2-P2P, and Pt2O2-P2P2 were investigated by recording their emission at 77K and room temperature. At 77 K, Pt2O2-P2M, Pt2O2-P2P, and Pt2O2-P2P2 exhibited emissions peaking at 472, 474, and 478 nm, respectively. The longest emission peak wavelength of Pt2O2-P2P2 is likely because phenyl group compared to mesityl can form a larger conjugation with imidazole ring, which is confirmed with the smaller tilted angle between phenyl substituent and main frame surface by the DFT calculations (Figure 5.39). At room temperature, Pt2O2-P2M showed no changes in emission peak wavelength, whereas Pt2O2-P2P and Pt2O2-P2P2 exhibited a slight redshift in the range of 2-4 nm. Moreover, all of Pt2O2-P2M, Pt2O2-P2P and Pt2O2-P2P2 displayed narrow-band emission with FWHM value of 16, 22, and 21 nm, respectively. Emission spectra of another three Pt(II) complexes, i.e, Pt2O2-PPy5-M, Pt2O2-Py5P-M, and Pt2O2-Py5Py5-M, are shown in Figure 5.40. Their emission peaks at room temperature displayed a slightly longer wavelength in the range of 476-480 nm. Pt2O2-PPy5-M, Pt2O2-Py5P-M, and Pt2O2-Py5Py5-M also achieved narrow-band emission with FWHM values of 16, 20, and 18 nm, respectively. To the author's best knowledge, Pt2O2-P2M and Pt2O2-PPy5-M

are among the narrowest emission spectrum of Ir(III) and Pt(II) complexes,[20, 22, 86] and is with higher color purity than most reported quantum-dot emission spectra.[101, 153]

6 CONCLUSIONS AND FUTURE OUTLOOK

In this dissertation, a series of tetradentate Pd(II) complex, i.e., Pd3O8-P, Pd3O8-Py2 and Pd3O8-Py5, featuring molecular aggregate emission were developed. Stable and efficient OLEDs employing phosphorescent molecular aggregates, especially at high brightness level, were demonstrated. The luminescent lifetime of Pd(II) complex aggregates was demonstrated to be shorter than 1 μs with close-to-unity photoluminescence quantum yield. As a result, an extremely efficient and stable phosphorescent molecular aggregates based OLED was developed by utilizing a Pd(II) complex named Pd3O8-Py5 as an emitter. The Pd3O8-Py5 based amber OLED exhibited a peak EQE of 37.3% and a reduced efficiency roll-off with high EQEs of 36.0% and 32.5% at 1000 and 10000 cd m^{-2} respectively. This efficient device also demonstrates a long measured LT_{95} lifetime of over 500 h with an initial brightness of 17304 cd m^{-2} corresponding to an estimated LT_{95} lifetime of 48246 h at 1000 cd m^{-2}.

Moreover, with judicious ligand design, four tetradentate Pd(II) complexes, i.e., Pd3O3, Pd3O8-P, Pd3O8-Py2 and Pd3O8-Py5, featuring phosphorescent molecular aggregates emission were investigated by thoroughly examining their electrochemical, photophysical properties and device performance. Results indicated that slight structural changes of ligands could modify the hole and electron transporting capabilities, and alter the horizontal emitting dipole ratios of aggregate in amorphous film, and the latter of which are sensitive to the thin film deposition conditions including the deposition rate and the choice of the templating layer.

It is worth pointing out that these tetradentate metal complexes has the triplets in the blue-emitting region along with the fact of remarkable electrochemical stability

demonstrated in the device settings, suggesting that phosphorescent molecular aggregate based emitter may also assist the development of efficient and long-lived blue OLEDs in the future. Additionally, provided that the luminescent lifetime (τ) of Pd(II) complex aggregates was shortened more than 100-fold to below 1μs compared to its monomer emission, phosphorescent molecular aggregates with bigger heavy metal ions (such as Pt(II) etc.) may even demonstrate shorter excited-state lifetimes such as in the nanosecond range, through which TTA or TPQ processes can be effectively supressed. Thus, it is of great interest to conduct an in-depth computational study of the quantum mechanics of both the monomer and aggregate species and their molecular dynamics inside thin films, which may eventually assist the development of molecular aggregate based OLEDs even in deep-blue emission range with long operational lifetime. Moreover, by utilizing both high-energy monomer emission and low-energy aggregate emission of a single emitter, it is of great promise to develop both stable and efficient single-doped white OLEDs, which will largely simplify the device structure and lower the fabrication cost.

There is an increasing demand for NIR OLEDs with an emission spectrum beyond 900 nm to expand their applications in biometric authentication, night vision display, and telecommunication, etc. In this dissertation, a stable and efficient near-infrared Pt(II) porphyrin complex, i.e. Pt(II) tetra(3,5-difluorophenyl)tetranaphthoporphyrin named PtTPTNP-F_8 was developed, and exhibited electroluminescent spectrum peaking at 920 nm with 84% of spectral wavelengths longer than 900 nm. By introducing fluorine atoms on the meta positions of all four phenyl groups, PtTPTNP-F_8 can successfully overcome the common thermal instability issue

emerging from the heavy Pt(II) porphyrin complexes, demonstrating a sublimation yield of above 90%. By carefully choosing the host materials, an NIR OLED with PtTPTNP-F_8 as an emissive material achieved a high peak EQE of 1.9%. Furthermore, devices of PtTPTNP-F_8 fabricated in a stable device architecture demonstrated extraordinary operational stability with a LT_{99} lifetime of >1000 h at a constant driving current density of 20 mA cm^{-2}. This work demonstrated that porphyrin can be a promising NIR emitter candidate to realize the high efficiency. It is believed that in a more charge-balanced device with state-of-art electron/hole transporting and blocking materials, an NIR OLED with better performance especially at high driving voltage will be expected.

Additionally, this dissertation also studied the photophysical properties of a series of imidazole-based blue Pt(II) complexes. Results indicated that structural modification of ligand molecules can effectively tune the emission wavelength and spectral bandwidth of the blue phosphorescent emitters. Several blue Pt(II) complexes, such as Pt2O2-P2M and Pt2O2-PPy5-M, exhibited narrow emission spectra peaking at 472 and 476 nm with FWHM value of 16 nm.

REFERENCES

1. Pope, M., Kallmann, H. P., & Magnante, P. (1963). Electroluminescence in Organic Crystals. *The Journal of Chemical Physics*, *38*(8), 2042–2043. https://doi.org/10.1063/1.1733929

2. Sano, M., Pope, M., & Kallmann, H. (1965). Electroluminescence and Band Gap in Anthracene. *The Journal of Chemical Physics*, *43*(8), 2920–2921. https://doi.org/10.1063/1.1697243

3. Helfrich, W., & Schneider, W. G. (1965). Recombination Radiation in Anthracene Crystals. *Physical Review Letters*, *14*(7), 229–231. https://doi.org/10.1103/PhysRevLett.14.229

4. Tang, C. W., & VanSlyke, S. A. (1987). Organic electroluminescent diodes. *Applied Physics Letters*, *51*(12), 913–915. https://doi.org/10.1063/1.98799

5. Yersin, H., Rausch, A. F., Czerwieniec, R., Hofbeck, T., & Fischer, T. (2011). The triplet state of organo-transition metal compounds. Triplet harvesting and singlet harvesting for efficient OLEDs. *Coordination Chemistry Reviews*, *255*(21–22), 2622–2652. https://doi.org/10.1016/j.ccr.2011.01.042

6. Yersin, H. (2008). *Highly Efficient OLEDs with Phosphorescent Materials*. John Wiley & Sons.

7. Baldo, M. A., O'Brien, D. F., You, Y., Shoustikov, A., Sibley, S., Thompson, M. E., & Forrest, S. R. (1998). Highly efficient phosphorescent emission from organic electroluminescent devices. *Nature*, *395*(6698), 151–154. https://doi.org/10.1038/25954

8. Baldo, M. A., Lamansky, S., Burrows, P. E., Thompson, M. E., & Forrest, S. R. (1999). Very high-efficiency green organic light-emitting devices based on electrophosphorescence. *Applied Physics Letters*, *75*(1), 4–6. https://doi.org/10.1063/1.124258

9. Kwong, R. C., Sibley, S., Dubovoy, T., Baldo, M., Forrest, S. R., & Thompson, M. E. (1999). Efficient, Saturated Red Organic Light Emitting Devices Based on Phosphorescent Platinum(II) Porphyrins. *Chemistry of Materials*, *11*(12), 3709–3713. https://doi.org/10.1021/cm9906248

10. Baldo, M. A., Thompson, M. E., & Forrest, S. R. (2000). High-efficiency fluorescent organic light-emitting devices using a phosphorescent sensitizer. *Nature*, *403*(6771), 750–753. https://doi.org/10.1038/35001541

11. Sun, Y., Giebink, N. C., Kanno, H., Ma, B., Thompson, M. E., & Forrest, S. R. (2006). Management of singlet and triplet excitons for efficient white organic light-emitting devices. *Nature*, *440*, 908.

12. Sun, Y., & Forrest, S. R. (2008). Enhanced light out-coupling of organic light-emitting devices using embedded low-index grids. *Nature Photonics; London*, *2*(8), 483–487. http://dx.doi.org.ezproxy1.lib.asu.edu/10.1038/nphoton.2008.132

13. Zhang, Y., Lee, J., & Forrest, S. R. (2014). Tenfold increase in the lifetime of blue phosphorescent organic light-emitting diodes. *Nature Communications*, *5*(1), 5008. https://doi.org/10.1038/ncomms6008

14. Qu, Y., Slootsky, M., & Forrest, S. R. (2015). Enhanced light extraction from organic light-emitting devices using a sub-anode grid. *Nature Photonics*, *9*(11), 758–763. https://doi.org/10.1038/nphoton.2015.194

15. Lee, J., Chen, H.-F., Batagoda, T., Coburn, C., Djurovich, P. I., Thompson, M. E., & Forrest, S. R. (2016). Deep blue phosphorescent organic light-emitting diodes with very high brightness and efficiency. *Nature Materials*, *15*(1), 92–98. https://doi.org/10.1038/nmat4446

16. Salehi, A., Fu, X., Shin, D.-H., & So, F. (2019). Recent Advances in OLED Optical Design. *Advanced Functional Materials*, *29*(15), 1808803. https://doi.org/10.1002/adfm.201808803

17. Chan, C.-Y., Tanaka, M., Nakanotani, H., & Adachi, C. (2018). Efficient and stable sky-blue delayed fluorescence organic light-emitting diodes with CIEy below 0.4. *Nature Communications*, *9*(1), 5036. https://doi.org/10.1038/s41467-018-07482-6

18. Kim, D.-H., D'Aléo, A., Chen, X.-K., Sandanayaka, A. D. S., Yao, D., Zhao, L., … Adachi, C. (2018). High-efficiency electroluminescence and amplified spontaneous emission from a thermally activated delayed fluorescent near-infrared emitter. *Nat. Photon.*, *12*(2), 98–104. https://doi.org/10.1038/s41566-017-0087-y

19. Cui, L.-S., Gillett, A. J., Zhang, S.-F., Ye, H., Liu, Y., Chen, X.-K., … Friend, R. H. (2020). Fast spin-flip enables efficient and stable organic electroluminescence from charge-transfer states. *Nature Photonics*, *14*(10), 636–642. https://doi.org/10.1038/s41566-020-0668-z

20. Fleetham, T., Li, G., & Li, J. (2017). Phosphorescent Pt(II) and Pd(II) complexes for efficient, high-color-quality, and stable OLEDs. *Adv. Mater.*, *29*(5), 1601861. https://doi.org/10.1002/adma.201601861

21. Fleetham, T. B., Huang, L., Klimes, K., Brooks, J., & Li, J. (2016). Tetradentate Pt(II) complexes with 6-membered chelate rings: a new route for stable and efficient blue organic light emitting diodes. *Chemistry of Materials*, *28*(10), 3276–3282. https://doi.org/10.1021/acs.chemmater.5b04957

22. Fleetham, T., Li, G., Wen, L., & Li, J. (2014). Efficient “Pure” Blue OLEDs Employing Tetradentate Pt Complexes with a Narrow Spectral Bandwidth. *Advanced Materials*, *26*(41), 7116–7121. https://doi.org/10.1002/adma.201401759

23. Li, G., Fleetham, T., & Li, J. (2014). Efficient and stable white organic light-emitting diodes employing a single emitter. *Advanced Materials*, *26*(18), 2931–2936. https://doi.org/10.1002/adma.201305507

24. Zhu, Z.-Q., Fleetham, T., Turner, E., & Li, J. (2015). Harvesting all electrogenerated excitons through metal assisted delayed fluorescent materials. *Adv. Mater.*, *27*(15), 2533–2537. https://doi.org/10.1002/adma.201401772

25. Zhang, D., Song, X., Gillett, A. J., Drummond, B. H., Jones, S. T. E., Li, G., … Duan, L. (2020). Efficient and Stable Deep-Blue Fluorescent Organic Light-Emitting Diodes Employing a Sensitizer with Fast Triplet Upconversion. *Advanced Materials*, *32*(19), 1908355. https://doi.org/10.1002/adma.201908355

26. Nguyen, T. B., Nakanotani, H., Hatakeyama, T., & Adachi, C. (2020). The Role of Reverse Intersystem Crossing Using a TADF-Type Acceptor Molecule on the Device Stability of Exciplex-Based Organic Light-Emitting Diodes. *Advanced Materials*, *32*(9), 1906614. https://doi.org/10.1002/adma.201906614

27. Forrest, S. R. (2020). *Organic Electronics: Foundations to Applications*. Oxford University Press.

28. Zhang, D., Huang, T., & Duan, L. (2020). Emerging Self-Emissive Technologies for Flexible Displays. *Advanced Materials*, *32*(15), 1902391. https://doi.org/10.1002/adma.201902391

29. Murawski, C., Leo, K., & Gather, M. C. (2013). Efficiency Roll-Off in Organic Light-Emitting Diodes. *Advanced Materials*, *25*(47), 6801–6827. https://doi.org/10.1002/adma.201301603

30. Murawski, C., Leo, K., & Gather, M. C. (2013). Efficiency roll-off in organic light-emitting diodes. *Adv. Mater.*, *25*(47), 6801–6827. https://doi.org/10.1002/adma.201301603

31. Zhang, Y., Whited, M., Thompson, M. E., & Forrest, S. R. (2010). Singlet–triplet quenching in high intensity fluorescent organic light emitting diodes. *Chemical Physics Letters*, *495*(4–6), 161–165. https://doi.org/10.1016/j.cplett.2010.06.079

32. Zhang, Y., & Forrest, S. R. (2013). Triplet diffusion leads to triplet–triplet annihilation in organic phosphorescent emitters. *Chemical Physics Letters*, *590*, 106–110. https://doi.org/10.1016/j.cplett.2013.10.048

33. Lee, J., Jeong, C., Batagoda, T., Coburn, C., Thompson, M. E., & Forrest, S. R. (2017). Hot excited state management for long-lived blue phosphorescent organic

light-emitting diodes. *Nat. Commun.*, *8*, 15566. https://doi.org/10.1038/ncomms15566

34. Lunt, R. R., Giebink, N. C., Belak, A. A., Benziger, J. B., & Forrest, S. R. (2009). Exciton diffusion lengths of organic semiconductor thin films measured by spectrally resolved photoluminescence quenching. *Journal of Applied Physics*, *105*(5), 053711. https://doi.org/10.1063/1.3079797

35. Staroske, W., Pfeiffer, M., Leo, K., & Hoffmann, M. (2007). Single-Step Triplet-Triplet Annihilation: An Intrinsic Limit for the High Brightness Efficiency of Phosphorescent Organic Light Emitting Diodes. *Physical Review Letters*, *98*(19). https://doi.org/10.1103/PhysRevLett.98.197402

36. Reineke, S., Schwartz, G., Walzer, K., Falke, M., & Leo, K. (2009). Highly phosphorescent organic mixed films: The effect of aggregation on triplet-triplet annihilation. *Applied Physics Letters*, *94*(16), 163305. https://doi.org/10.1063/1.3123815

37. Smith, A. R. G., Ruggles, J. L., Cavaye, H., Shaw, P. E., Darwish, T. A., James, M., … Burn, P. L. (2011). Investigating Morphology and Stability of Fac-tris (2-phenylpyridyl)iridium(III) Films for OLEDs. *Adv. Funct. Mater.*, *21*(12), 2225–2231. https://doi.org/10.1002/adfm.201002365

38. Li, J., Djurovich, P. I., Alleyne, B. D., Yousufuddin, M., Ho, N. N., Thomas, J. C., … Thompson, M. E. (2005). Synthetic Control of Excited-State Properties in Cyclometalated Ir(III) Complexes Using Ancillary Ligands. *Inorganic Chemistry*, *44*(6), 1713–1727. https://doi.org/10.1021/ic048599h

39. Huang, L., Park, C. D., Fleetham, T., & Li, J. (2016). Platinum (II) azatetrabenzoporphyrins for near-infrared organic light emitting diodes. *Appl. Phys. Lett.*, *109*(23), 233302. https://doi.org/10.1063/1.4971363

40. Wei, Y.-C., Wang, S. F., Hu, Y., Liao, L.-S., Chen, D.-G., Chang, K.-H., … Chou, P.-T. (2020). Overcoming the energy gap law in near-infrared OLEDs by exciton–vibration decoupling. *Nature Photonics*, *14*(9), 570–577. https://doi.org/10.1038/s41566-020-0653-6

41. Sommer, J. R., Shelton, A. H., Parthasarathy, A., Ghiviriga, I., Reynolds, J. R., & Schanze, K. S. (2011). Photophysical Properties of Near-Infrared Phosphorescent π-Extended Platinum Porphyrins. *Chem. Mater.*, *23*(24), 5296–5304. https://doi.org/10.1021/cm202241e

42. Zhang, Y., Wang, Y., Song, J., Qu, J., Li, B., Zhu, W., & Wong, W.-Y. (2018). Near-Infrared Emitting Materials via Harvesting Triplet Excitons: Molecular Design, Properties, and Application in Organic Light Emitting Diodes. *Adv. Opt. Mater.*, *6*(18), 1800466. https://doi.org/10.1002/adom.201800466

43. Rausch, A. F., Homeier, H., Djurovich, P. I., Thompson, M. E., & Yersin, H. (2007). Spin-orbit coupling routes and OLED performance: studies of blue-light emitting Ir(III) and Pt (II) complexes. In *Organic Light Emitting Materials and Devices XI* (Vol. 6655, p. 66550F). Presented at the Organic Light Emitting Materials and Devices XI, International Society for Optics and Photonics. https://doi.org/10.1117/12.731225

44. Hofbeck, T., & Yersin, H. (2010). The Triplet State of fac-Ir(ppy)3. *Inorganic Chemistry*, *49*(20), 9290–9299. https://doi.org/10.1021/ic100872w

45. Yersin, H., Donges, D., Humbs, W., Strasser, J., Sitters, R., & Glasbeek, M. (2002). Organometallic Pt(II) Compounds. A Complementary Study of a Triplet Emitter Based on Optical High-Resolution and Optically Detected Magnetic Resonance Spectroscopy. *Inorganic Chemistry*, *41*(19), 4915–4922. https://doi.org/10.1021/ic020132o

46. Yersin, H. (2004). Triplet Emitters for OLED Applications. Mechanisms of Exciton Trapping and Control of Emission Properties. In *Transition Metal and Rare Earth Compounds* (Vol. 241, pp. 1–26). Berlin, Heidelberg: Springer Berlin Heidelberg. https://doi.org/10.1007/b96858

47. Pinter, P., Mangold, H., Stengel, I., Münster, I., & Strassner, T. (2016). Enhanced Photoluminescence Quantum Yields through Excimer Formation of Cyclometalated Platinum(II) N-Heterocyclic Carbene Complexes. *Organometallics*, *35*(5), 673–680. https://doi.org/10.1021/acs.organomet.5b00982

48. Ma, B., Li, J., Djurovich, P. I., Yousufuddin, M., Bau, R., & Thompson, M. E. (2005). Synthetic control of Pt···Pt separation and photophysics of binuclear platinum complexes. *Journal of the American Chemical Society*, *127*(1), 28–29. https://doi.org/10.1021/ja044313w

49. Kim, K.-H., Liao, J.-L., Lee, S. W., Sim, B., Moon, C.-K., Lee, G.-H., … Kim, J.-J. (2016). Crystal organic light-emitting diodes with perfectly oriented non-doped Pt-based emitting layer. *Advanced Materials*, *28*(13), 2526–2532. https://doi.org/10.1002/adma.201504451

50. Ganesan, P., Hung, W.-Y., Tso, J.-Y., Ko, C.-L., Wang, T.-H., Chen, P.-T., … Chi, Y. (2019). Functional pyrimidinyl pyrazolate Pt(II) complexes: role of nitrogen atom in tuning the solid-state stacking and photophysics. *Advanced Functional Materials*, *0*(0), 1900923. https://doi.org/10.1002/adfm.201900923

51. Cheng, G., Wan, Q., Ang, W.-H., Kwong, C.-L., To, W.-P., Chow, P.-K., … Che, C.-M. (2019). High-Performance Deep-Red/Near-Infrared OLEDs with Tetradentate [Pt(O^N^C^N)] Emitters. *Advanced Optical Materials*, *7*(5), 1801452. https://doi.org/10.1002/adom.201801452

52. Tuong Ly, K., Chen-Cheng, R.-W., Lin, H.-W., Shiau, Y.-J., Liu, S.-H., Chou, P.-T., … Chi, Y. (2017). Near-infrared organic light-emitting diodes with very high external quantum efficiency and radiance. *Nat. Photonics*, *11*(1), 63–68. https://doi.org/10.1038/nphoton.2016.230

53. Ma, B., Djurovich, P. I., & Thompson, M. E. (2005). Excimer and electron transfer quenching studies of a cyclometalated platinum complex. *Coordination Chemistry Reviews*, *249*(13–14), 1501–1510. https://doi.org/10.1016/j.ccr.2005.02.004

54. D'Andrade, B., & Forrest, S. R. (2003). Formation of triplet excimers and dimers in amorphous organic thin films and light emitting devices. *Chemical Physics*, *286*(2), 321–335. https://doi.org/10.1016/S0301-0104(02)00921-7

55. Li, G., Fleetham, T., & Li, J. (2014). Efficient and Stable White Organic Light-Emitting Diodes Employing a Single Emitter. *Advanced Materials*, *26*(18), 2931–2936. https://doi.org/10.1002/adma.201305507

56. Fleetham, T., Ji, Y., Huang, L., Fleetham, T. S., & Li, J. (2017). Efficient and stable single-doped white OLEDs using a palladium-based phosphorescent excimer. *Chemical Science*, *8*(12), 7983–7990. https://doi.org/10.1039/C7SC02512B

57. Fleetham, T., Ecton, J., Wang, Z., Bakken, N., & Li, J. (2013). Single-doped white organic light-emitting device with an external quantum efficiency over 20%. *Advanced Materials*, *25*(18), 2573–2576. https://doi.org/10.1002/adma.201204602

58. Kim, K.-H., Ma, J.-Y., Moon, C.-K., Lee, J.-H., Baek, J. Y., Kim, Y.-H., & Kim, J.-J. (2015). Controlling Emitting Dipole Orientation with Methyl Substituents on Main Ligand of Iridium Complexes for Highly Efficient Phosphorescent Organic Light-Emitting Diodes. *Advanced Optical Materials*, *3*(9), 1191–1196. https://doi.org/10.1002/adom.201500141

59. Lai, S.-W., Lam, H.-W., Lu, W., Cheung, K.-K., & Che, C.-M. (2002). Observation of Low-Energy Metal−Metal-to-Ligand Charge Transfer Absorption and Emission: Electronic Spectroscopy of Cyclometalated Platinum(II) Complexes with Isocyanide Ligands. *Organometallics*, *21*(1), 226–234. https://doi.org/10.1021/om0106276

60. Lai, S.-W., & Che, C.-M. (2004). Luminescent Cyclometalated Diimine Platinum(II) Complexes: Photophysical Studies and Applications. In *Transition Metal and Rare Earth Compounds* (Vol. 241, pp. 27–63). Berlin, Heidelberg: Springer Berlin Heidelberg. https://doi.org/10.1007/b96859

61. Cho, S., Mara, M. W., Wang, X., Lockard, J. V., Rachford, A. A., Castellano, F. N., & Chen, L. X. (2011). Coherence in Metal−Metal-to-Ligand-Charge-Transfer Excited States of a Dimetallic Complex Investigated by Ultrafast Transient

Absorption Anisotropy. *The Journal of Physical Chemistry A*, *115*(16), 3990–3996. https://doi.org/10.1021/jp109174f

62. Fleetham, T., & Li, J. (2014). Recent advances in white organic light-emitting diodes employing a single-emissive material. *Journal of Photonics for Energy*, *4*(1), 040991. https://doi.org/10.1117/1.JPE.4.040991

63. Williams, E. L., Haavisto, K., Li, J., & Jabbour, G. E. (2007). Excimer-Based White Phosphorescent Organic Light-Emitting Diodes with Nearly 100 % Internal Quantum Efficiency. *Advanced Materials*, *19*(2), 197–202. https://doi.org/10.1002/adma.200602174

64. Yang, X., Wang, Z., Madakuni, S., Li, J., & Jabbour, G. E. (2008). Highly efficient excimer-based white phosphorescent devices with improved power efficiency and color rendering index. *Applied Physics Letters*, *93*(19), 193305. https://doi.org/10.1063/1.3013324

65. Murphy, L., Brulatti, P., Fattori, V., Cocchi, M., & Gareth Williams, J. A. (2012). Blue-shifting the monomer and excimer phosphorescence of tridentate cyclometallated platinum(ii) complexes for optimal white-light OLEDs. *Chemical Communications*, *48*(47), 5817–5819. https://doi.org/10.1039/C2CC31330H

66. Shigehiro, T., Yagi, S., Maeda, T., Nakazumi, H., Fujiwara, H., & Sakurai, Y. (2013). Photo- and Electroluminescence from 2-(Dibenzo[*b* , *d*]furan-4-yl)pyridine-Based Heteroleptic Cyclometalated Platinum(II) Complexes: Excimer Formation Drastically Facilitated by an Aromatic Diketonate Ancillary Ligand. *The Journal of Physical Chemistry C*, *117*(1), 532–542. https://doi.org/10.1021/jp307853t

67. Fleetham, T., Huang, L., & Li, J. (2014). Tetradentate platinum complexes for efficient and stable excimer-based white OLEDs. *Advanced Functional Materials*, *24*(38), 6066–6073. https://doi.org/10.1002/adfm.201401244

68. Kim, K.-H., & Kim, J.-J. (2018). Origin and control of orientation of phosphorescent and TADF dyes for high-efficiency OLEDs. *Advanced Materials*, *30*(42), 1705600. https://doi.org/10.1002/adma.201705600

69. Kim, J., Batagoda, T., Lee, J., Sylvinson, D., Ding, K., Saris, PatrickJ. G., … Forrest, S. R. (2019). Systematic Control of the Orientation of Organic Phosphorescent Pt Complexes in Thin Films for Increased Optical Outcoupling. *Advanced Materials*, 1900921. https://doi.org/10.1002/adma.201900921

70. Zhang, Q., Li, B., Huang, S., Nomura, H., Tanaka, H., & Adachi, C. (2014). Efficient blue organic light-emitting diodes employing thermally activated delayed fluorescence. *Nature Photonics; London*, *8*(4), 326–332. http://dx.doi.org.ezproxy1.lib.asu.edu/10.1038/nphoton.2014.12

71. Hua, H., Hu, X., & Gao, C. (2013). A high-resolution optical see-through head-mounted display with eyetracking capability. *Optics Express, 21*(25), 30993–30998. https://doi.org/10.1364/OE.21.030993

72. D'Andrade, B. W., & Forrest, S. R. (2004). White organic light-emitting devices for solid-state lighting. *Advanced Materials, 16*(18), 1585–1595. https://doi.org/10.1002/adma.200400684

73. So, F., Kido, J., & Burrows, P. (2008). Organic light-emitting devices for solid-state lighting. *MRS Bull., 33*(7), 663–669. https://doi.org/10.1557/mrs2008.137

74. Baldo, M. A., Adachi, C., & Forrest, S. R. (2000). Transient analysis of organic electrophosphorescence. II. Transient analysis of triplet-triplet annihilation. *Physical Review B, 62*(16), 10967–10977. https://doi.org/10.1103/PhysRevB.62.10967

75. Reineke, S., Walzer, K., & Leo, K. (2007). Triplet-exciton quenching in organic phosphorescent light-emitting diodes with Ir-based emitters. *Physical Review B, 75*(12), 125328. https://doi.org/10.1103/PhysRevB.75.125328

76. Coburn, C., Lee, J., & Forrest, S. R. (2016). Charge balance and exciton confinement in phosphorescent organic light emitting diodes. *Advanced Optical Materials, 4*(6), 889–895. https://doi.org/10.1002/adom.201600067

77. Su, S.-J., Gonmori, E., Sasabe, H., & Kido, J. (2008). Highly efficient organic blue-and white-light-emitting devices having a carrier- and exciton-confining structure for reduced efficiency roll-off. *Advanced Materials, 20*(21), 4189–4194. https://doi.org/10.1002/adma.200801375

78. Park, Y.-S., Lee, S., Kim, K.-H., Kim, S.-Y., Lee, J.-H., & Kim, J.-J. (2013). Exciplex-forming co-host for organic light-emitting diodes with ultimate efficiency. *Advanced Functional Materials, 23*(39), 4914–4920. https://doi.org/10.1002/adfm.201300547

79. Klimes, K., Zhu, Z.-Q., & Li, J. (2019). Efficient blue phosphorescent OLEDs with improved stability and color purity through judicious triplet exciton management. *Advanced Functional Materials, 29*(31), 1903068. https://doi.org/10.1002/adfm.201903068

80. Lee, S., Kim, K.-H., Limbach, D., Park, Y.-S., & Kim, J.-J. (2013). Low roll-off and high efficiency orange organic light emitting diodes with controlled co-doping of green and red phosphorescent dopants in an exciplex forming co-host. *Advanced Functional Materials, 23*(33), 4105–4110. https://doi.org/10.1002/adfm.201300187

81. Gong, S., Chen, Y., Luo, J., Yang, C., Zhong, C., Qin, J., & Ma, D. (2011). Bipolar tetraarylsilanes as universal hosts for blue, green, orange, and white

electrophosphorescence with high efficiency and low efficiency roll-off. *Advanced Functional Materials*, *21*(6), 1168–1178. https://doi.org/10.1002/adfm.201002066

82. Kawamura, Y., Brooks, J., Brown, J. J., Sasabe, H., & Adachi, C. (2006). Intermolecular interaction and a concentration-quenching mechanism of phosphorescent Ir(III) complexes in a solid film. *Physical Review Letters*, *96*(1), 017404. https://doi.org/10.1103/PhysRevLett.96.017404

83. Holmes, R. J., Forrest, S. R., Sajoto, T., Tamayo, A., Djurovich, P. I., & Thompson, M. E. (2006). Reduced geminate recombination in iridium-based electrophosphorescent materials. *Organic Electronics*, *7*(3), 163–172. https://doi.org/10.1016/j.orgel.2006.03.009

84. Wang, Q., Oswald, I. W. H., Yang, X., Zhou, G., Jia, H., Qiao, Q., … Gnade, B. E. (2014). A non-doped phosphorescent organic light-emitting device with above 31% external quantum efficiency. *Advanced Materials*, *26*(48), 8107–8113. https://doi.org/10.1002/adma.201402947

85. Chow, P. K., Ma, C., To, W.-P., Tong, G. S. M., Lai, S.-L., Kui, S. C. F., … Che, C.-M. (2013). Strongly phosphorescent palladium(II) complexes of tetradentate ligands with mixed oxygen, carbon, and nitrogen donor atoms: photophysics, photochemistry, and applications. *Angewandte Chemie International Edition*, *52*(45), 11775–11779. https://doi.org/10.1002/anie.201305590

86. Li, G., Wolfe, A., Brooks, J., Zhu, Z.-Q., & Li, J. (2017). Modifying emission spectral bandwidth of phosphorescent platinum(II) complexes through synthetic control. *Inorganic Chemistry*, *56*(14), 8244–8256. https://doi.org/10.1021/acs.inorgchem.7b00961

87. Lamansky, S., Djurovich, P., Murphy, D., Abdel-Razzaq, F., Kwong, R., Tsyba, I., … Thompson, M. E. (2001). Synthesis and characterization of phosphorescent cyclometalated iridium complexes. *Inorganic Chemistry*, *40*(7), 1704–1711. https://doi.org/10.1021/ic0008969

88. Díez, Á., Forniés, J., Larraz, C., Lalinde, E., López, J. A., Martín, A., … Sicilia, V. (2010). Structural and luminescence studies on π···π and Pt···Pt interactions in mixed chloro-isocyanide cyclometalated platinum(II) complexes. *Inorganic Chemistry*, *49*(7), 3239–3251. https://doi.org/10.1021/ic902094c

89. Chan, K. H.-Y., Chow, H.-S., Wong, K. M.-C., Yeung, M. C.-L., & Yam, V. W.-W. (2010). Towards thermochromic and thermoresponsive near-infrared (NIR) luminescent molecular materials through the modulation of inter- and/or intramolecular Pt···Pt and π–π interactions. *Chemical Science*, *1*(4), 477–482. https://doi.org/10.1039/C0SC00208A

90. Lai, S.-W., Cheung, T.-C., Chan, M. C. W., Cheung, K.-K., Peng, S.-M., & Che, C.-M. (2000). Luminescent mononuclear and binuclear cyclometalated

palladium(II) complexes of 6-phenyl-2,2'-bipyridines: spectroscopic and structural comparisons with platinum(II) analogues[1,2]. *Inorganic Chemistry*, *39*(2), 255–262. https://doi.org/10.1021/ic991089g

91. Lu, W., Chan, M. C. W., Zhu, N., Che, C.-M., Li, C., & Hui, Z. (2004). Structural and spectroscopic studies on Pt···Pt and π–π interactions in luminescent multinuclear cyclometalated platinum(II) homologues tethered by oligophosphine auxiliaries. *Journal of the American Chemical Society*, *126*(24), 7639–7651. https://doi.org/10.1021/ja039727o

92. Kim, D., & Brédas, J.-L. (2009). Triplet excimer formation in platinum-based phosphors: a theoretical study of the roles of Pt−Pt bimetallic interactions and interligand π–π interactions. *Journal of the American Chemical Society*, *131*(32), 11371–11380. https://doi.org/10.1021/ja809924t

93. Zhu, Z.-Q., Park, C.-D., Klimes, K., & Li, J. (2019). Highly efficient blue OLEDs based on metal-assisted delayed fluorescence Pd(II) complexes. *Advanced Optical Materials*, *7*(6), 1801518. https://doi.org/10.1002/adom.201801518

94. Lee, J., Chopra, N., Bera, D., Maslov, S., Eom, S.-H., Zheng, Y., … So, F. (2011). Down-donversion white organic light-emitting diodes using microcavity structure. *Advanced Energy Materials*, *1*(2), 174–178. https://doi.org/10.1002/aenm.201000014

95. Do, Y. R., Kim, Y. C., Song, Y.-W., Cho, C.-O., Jeon, H., Lee, Y.-J., … Lee, Y.-H. (2003). Enhanced light extraction from organic light-emitting diodes with 2D SiO_2/SiNx photonic crystals. *Advanced Materials*, *15*(14), 1214–1218. https://doi.org/10.1002/adma.200304857

96. Youn, W., Lee, J., Xu, M., Singh, R., & So, F. (2015). Corrugated sapphire substrates for organic light-emitting diode light extraction. *ACS Applied Materials & Interfaces*, *7*(17), 8974–8978. https://doi.org/10.1021/acsami.5b01533

97. Zhu, Z.-Q., Klimes, K., Holloway, S., & Li, J. (2017). Efficient cyclometalated platinum(II) complex with superior operational stability. *Adv. Mater.*, *29*(6), 1605002. https://doi.org/10.1002/adma.201605002

98. Féry, C., Racine, B., Vaufrey, D., Doyeux, H., & Cinà, S. (2005). Physical mechanism responsible for the stretched exponential decay behavior of aging organic light-emitting diodes. *Applied Physics Letters*, *87*(21), 213502. https://doi.org/10.1063/1.2133922

99. Nakanotani, H., Masui, K., Nishide, J., Shibata, T., & Adachi, C. (2013). Promising operational stability of high-efficiency organic light-emitting diodes based on thermally activated delayed fluorescence. *Sci. Rep.*, *3*(1), 2127. https://doi.org/10.1038/srep02127

100. Seo, S., Shitagaki, S., Ohsawa, N., Inoue, H., Suzuki, K., Nowatari, H., & Yamazaki, S. (2014). Exciplex-triplet energy transfer: A new method to achieve extremely efficient organic light-emitting diode with external quantum efficiency over 30% and drive voltage below 3 V. *Japanese Journal of Applied Physics*, *53*(4), 042102. https://doi.org/10.7567/JJAP.53.042102

101. Qian, L., Zheng, Y., Xue, J., & Holloway, P. H. (2011). Stable and efficient quantum-dot light-emitting diodes based on solution-processed multilayer structures. *Nature Photonics*, *5*(9), 543–548. https://doi.org/10.1038/nphoton.2011.171

102. Li, L.-K., Tang, M.-C., Lai, S.-L., Ng, M., Kwok, W.-K., Chan, M.-Y., & Yam, V. W.-W. (2019). Strategies towards rational design of gold(iii) complexes for high-performance organic light-emitting devices. *Nature Photonics*, *13*(3), 185–191. https://doi.org/10.1038/s41566-018-0332-z

103. Forrest, S. R. (2004). The path to ubiquitous and low-cost organic electronic appliances on plastic. *Nature*, *428*(6986), 911–918. https://doi.org/10.1038/nature02498

104. Gather, M. C., Köhnen, A., & Meerholz, K. (2011). White Organic Light-Emitting Diodes. *Advanced Materials*, *23*(2), 233–248. https://doi.org/10.1002/adma.201002636

105. Shin, H., Lee, S., Kim, K.-H., Moon, C.-K., Yoo, S.-J., Lee, J.-H., & Kim, J.-J. (2014). Blue Phosphorescent Organic Light-Emitting Diodes Using an Exciplex Forming Co-host with the External Quantum Efficiency of Theoretical Limit. *Advanced Materials*, *26*(27), 4730–4734. https://doi.org/10.1002/adma.201400955

106. Kim, J., Hou, S., Zhao, H., & Forrest, S. R. (2020). Nanoscale Mapping of Morphology of Organic Thin Films. *Nano Letters*, *20*(11), 8290–8297. https://doi.org/10.1021/acs.nanolett.0c03440

107. Lampe, T., Schmidt, T. D., Jurow, M. J., Djurovich, P. I., Thompson, M. E., & Brütting, W. (2016). Dependence of Phosphorescent Emitter Orientation on Deposition Technique in Doped Organic Films. *Chemistry of Materials*, *28*(3), 712–715. https://doi.org/10.1021/acs.chemmater.5b04607

108. Jurow, M. J., Mayr, C., Schmidt, T. D., Lampe, T., Djurovich, P. I., Brütting, W., & Thompson, M. E. (2016). Understanding and predicting the orientation of heteroleptic phosphors in organic light-emitting materials. *Nature Materials*, *15*(1), 85–91. https://doi.org/10.1038/nmat4428

109. Chow, P.-K., Cheng, G., Tong, G. S. M., Ma, C., Kwok, W.-M., Ang, W.-H., … Che, C.-M. (2016). Highly luminescent palladium(ii) complexes with sub-millisecond blue to green phosphorescent excited states. Photocatalysis and highly efficient PSF-OLEDs †Electronic supplementary information (ESI) available.

CCDC 1048773 and 1449190. For ESI and crystallographic data in CIF or other electronic format see DOI: 10.1039/c6sc00462h. *Chemical Science*, *7*(9), 6083–6098. https://doi.org/10.1039/c6sc00462h

110. Cao, L., Klimes, K., Ji, Y., Fleetham, T., & Li, J. (2021). Efficient and stable organic light-emitting devices employing phosphorescent molecular aggregates. *Nature Photonics*, *15*(15), 230–237. https://doi.org/10.1038/s41566-020-00734-2

111. Cui, L.-S., Deng, Y.-L., Tsang, D. P.-K., Jiang, Z.-Q., Zhang, Q., Liao, L.-S., & Adachi, C. (2016). Controlling Synergistic Oxidation Processes for Efficient and Stable Blue Thermally Activated Delayed Fluorescence Devices. *Advanced Materials*, *28*(35), 7620–7625. https://doi.org/10.1002/adma.201602127

112. Shin, H., Lee, J.-H., Moon, C.-K., Huh, J.-S., Sim, B., & Kim, J.-J. (2016). Sky-Blue Phosphorescent OLEDs with 34.1% External Quantum Efficiency Using a Low Refractive Index Electron Transporting Layer. *Advanced Materials*, *28*(24), 4920–4925. https://doi.org/10.1002/adma.201506065

113. Salehi, A., Ho, S., Chen, Y., Peng, C., Yersin, H., & So, F. (2017). Highly Efficient Organic Light-Emitting Diode Using A Low Refractive Index Electron Transport Layer. *Advanced Optical Materials*, *5*(11), 1700197. https://doi.org/10.1002/adom.201700197

114. Zampetti, A., Minotto, A., & Cacialli, F. (2019). Near-Infrared (NIR) Organic Light-Emitting Diodes (OLEDs): Challenges and Opportunities. *Adv. Funct. Mater.*, *29*(21), 1807623. https://doi.org/10.1002/adfm.201807623

115. Qiu, W., Xiao, Z., Roh, K., Noel, N. K., Shapiro, A., Heremans, P., & Rand, B. P. (2019). Mixed Lead–Tin Halide Perovskites for Efficient and Wavelength-Tunable Near-Infrared Light-Emitting Diodes. *Adv. Mater.*, *31*(3), 1806105. https://doi.org/10.1002/adma.201806105

116. Ishii, A., & Miyasaka, T. (2020). Sensitized Yb3+ Luminescence in CsPbCl3 Film for Highly Efficient Near-Infrared Light-Emitting Diodes. *Adv. Sci.*, *7*(4), 1903142. https://doi.org/10.1002/advs.201903142

117. Stender, B., Völker, S. F., Lambert, C., & Pflaum, J. (2013). Optoelectronic Processes in Squaraine Dye-Doped OLEDs for Emission in the Near-Infrared. *Adv. Mater.*, *25*(21), 2943–2947. https://doi.org/10.1002/adma.201204938

118. Qian, G., Zhong, Z., Luo, M., Yu, D., Zhang, Z., Wang, Z. Y., & Ma, D. (2009). Simple and Efficient Near-Infrared Organic Chromophores for Light-Emitting Diodes with Single Electroluminescent Emission above 1000 nm. *Adv. Mater.*, *21*(1), 111–116. https://doi.org/10.1002/adma.200801918

119. Minotto, A., Murto, P., Genene, Z., Zampetti, A., Carnicella, G., Mammo, W., … Cacialli, F. (2018). Efficient Near-Infrared Electroluminescence at 840 nm with

"Metal-Free" Small-Molecule:Polymer Blends. *Adv. Mater.*, *30*(34), 1706584. https://doi.org/10.1002/adma.201706584

120. Murto, P., Minotto, A., Zampetti, A., Xu, X., Andersson, M. R., Cacialli, F., & Wang, E. (2016). Triazolobenzothiadiazole-Based Copolymers for Polymer Light-Emitting Diodes: Pure Near-Infrared Emission via Optimized Energy and Charge Transfer. *Adv. Opt. Mater.*, *4*(12), 2068–2076. https://doi.org/10.1002/adom.201600483

121. Liu, T., Zhu, L., Zhong, C., Xie, G., Gong, S., Fang, J., … Yang, C. (2017). Naphthothiadiazole-Based Near-Infrared Emitter with a Photoluminescence Quantum Yield of 60% in Neat Film and External Quantum Efficiencies of up to 3.9% in Nondoped OLEDs. *Adv. Funct. Mater.*, *27*(12), 1606384. https://doi.org/10.1002/adfm.201606384

122. Yuan, Y., Hu, Y., Zhang, Y.-X., Lin, J.-D., Wang, Y.-K., Jiang, Z.-Q., … Lee, S.-T. (2017). Over 10% EQE Near-Infrared Electroluminescence Based on a Thermally Activated Delayed Fluorescence Emitter. *Adv. Funct. Mater.*, *27*(26), 1700986. https://doi.org/10.1002/adfm.201700986

123. Sun, R. G., Wang, Y. Z., Zheng, Q. B., Zhang, H. J., & Epstein, A. J. (2000). 1.54 μm infrared photoluminescence and electroluminescence from an erbium organic compound. *J. Appl. Phys.*, *87*(10), 7589–7591. https://doi.org/10.1063/1.373027

124. Harrison, B. S., Foley, T. J., Bouguettaya, M., Boncella, J. M., Reynolds, J. R., Schanze, K. S., … Ramakrishnan, S. (2001). Near-infrared electroluminescence from conjugated polymer/lanthanide porphyrin blends. *Appl. Phys. Lett.*, *79*(23), 3770–3772. https://doi.org/10.1063/1.1421413

125. Slooff, L. H., Polman, A., Cacialli, F., Friend, R. H., Hebbink, G. A., van Veggel, F. C. J. M., & Reinhoudt, D. N. (2001). Near-infrared electroluminescence of polymer light-emitting diodes doped with a lissamine-sensitized Nd3+ complex. *Appl. Phys. Lett.*, *78*(15), 2122–2124. https://doi.org/10.1063/1.1359782

126. Lee, T.-C., Hung, J.-Y., Chi, Y., Cheng, Y.-M., Lee, G.-H., Chou, P.-T., … Wu, C.-C. (2009). Rational Design of Charge-Neutral, Near-Infrared-Emitting Osmium(II) Complexes and OLED Fabrication. *Adv. Funct. Mater.*, *19*(16), 2639–2647. https://doi.org/10.1002/adfm.200900233

127. Liao, J.-L., Chi, Y., Yeh, C.-C., Kao, H.-C., Chang, C.-H., A. Fox, M., … Lee, G.-H. (2015). Near infrared-emitting tris-bidentate Os(ii) phosphors: control of excited state characteristics and fabrication of OLEDs. *J. Mater. Chem. C*, *3*(19), 4910–4920. https://doi.org/10.1039/C5TC00204D

128. Williams, E. L., Li, J., & Jabbour, G. E. (2006). Organic light-emitting diodes having exclusive near-infrared electrophosphorescence. *Appl. Phys. Lett.*, *89*(8), 083506. https://doi.org/10.1063/1.2335275

129. Xue, J., Xin, L., Hou, J., Duan, L., Wang, R., Wei, Y., & Qiao, J. (2017). Homoleptic Facial Ir(III) Complexes via Facile Synthesis for High-Efficiency and Low-Roll-Off Near-Infrared Organic Light-Emitting Diodes over 750 nm. *Chem. Mater.*, *29*(11), 4775–4782. https://doi.org/10.1021/acs.chemmater.7b00518

130. Sommer, J. R., Farley, R. T., Graham, K. R., Yang, Y., Reynolds, J. R., Xue, J., & Schanze, K. S. (2009). Efficient Near-Infrared Polymer and Organic Light-Emitting Diodes Based on Electrophosphorescence from (Tetraphenyltetranaphtho[2,3]porphyrin)platinum(II). *ACS Applied Materials & Interfaces*, *1*(2), 274–278. https://doi.org/10.1021/am800236x

131. Borek, C., Hanson, K., Djurovich, P. I., Thompson, M. E., Aznavour, K., Bau, R., … Brown, J. (2007). Highly Efficient, Near-Infrared Electrophosphorescence from a Pt–Metalloporphyrin Complex. *Angew Chem. Int. Ed.*, *46*(7), 1109–1112. https://doi.org/10.1002/anie.200604240

132. Sun, Y., Borek, C., Hanson, K., Djurovich, P. I., Thompson, M. E., Brooks, J., … Forrest, S. R. (2007). Photophysics of Pt-porphyrin electrophosphorescent devices emitting in the near infrared. *Appl. Phys. Lett.*, *90*(21), 213503. https://doi.org/10.1063/1.2740113

133. Graham, K. R., Yang, Y., Sommer, J. R., Shelton, A. H., Schanze, K. S., Xue, J., & Reynolds, J. R. (2011). Extended Conjugation Platinum(II) Porphyrins for use in Near-Infrared Emitting Organic Light Emitting Diodes. *Chem. Mater.*, *23*(24), 5305–5312. https://doi.org/10.1021/cm202242x

134. Finikova, O. S., Aleshchenkov, S. E., Briñas, R. P., Cheprakov, A. V., Carroll, P. J., & Vinogradov, S. A. (2005). Synthesis of Symmetrical Tetraaryltetranaphtho[2,3]porphyrins. *J. Org. Chem.*, *70*(12), 4617–4628. https://doi.org/10.1021/jo047741t

135. Finikova, O. S., Cheprakov, A. V., & Vinogradov, S. A. (2005). Synthesis and Luminescence of Soluble meso-Unsubstituted Tetrabenzo- and Tetranaphtho[2,3]porphyrins. *J. Org. Chem.*, *70*(23), 9562–9572. https://doi.org/10.1021/jo051580r

136. Borisov, S. M., & Klimant, I. (2009). Efficient metallation in diphenylether – A convenient route to luminescent platinum(II) complexes. *Dyes and Pigments*, *83*(3), 312–316. https://doi.org/10.1016/j.dyepig.2009.05.008

137. D'Andrade, B. W., Datta, S., Forrest, S. R., Djurovich, P., Polikarpov, E., & Thompson, M. E. (2005). Relationship between the ionization and oxidation potentials of molecular organic semiconductors. *Org. Electron.*, *6*(1), 11–20. https://doi.org/10.1016/j.orgel.2005.01.002

138. D'Andrade, B. W., Forrest, S. R., & Chwang, A. B. (2003). Operational stability of electrophosphorescent devices containing p and n doped transport layers. *Appl. Phys. Lett.*, *83*(19), 3858–3860. https://doi.org/10.1063/1.1624473

139. Theisen, R. F., Huang, L., Fleetham, T., Adams, J. B., & Li, J. (2015). Ground and excited states of zinc phthalocyanine, zinc tetrabenzoporphyrin, and azaporphyrin analogs using DFT and TDDFT with Franck-Condon analysis. *The Journal of Chemical Physics*, *142*(9), 094310. https://doi.org/10.1063/1.4913757

140. Ortega-Guerrero, A., Fumanal, M., Capano, G., & Smit, B. (2020). From Isolated Porphyrin Ligands to Periodic Al-PMOF: A Comparative Study of the Optical Properties Using DFT/TDDFT. *The Journal of Physical Chemistry C*, *124*(39), 21751–21760. https://doi.org/10.1021/acs.jpcc.0c06885

141. Perepogu, A. K., & Bangal, P. R. (2008). Preparation and characterization of free-standing pure porphyrin nanoparticles. *Journal of Chemical Sciences*, *120*(5), 485–491. https://doi.org/10.1007/s12039-008-0076-2

142. Borisov, S. M., Zenkl, G., & Klimant, I. (2010). Phosphorescent Platinum(II) and Palladium(II) Complexes with Azatetrabenzoporphyrins—New Red Laser Diode-Compatible Indicators for Optical Oxygen Sensing. *ACS Applied Materials & Interfaces*, *2*(2), 366–374. https://doi.org/10.1021/am900932z

143. Jeong, C., Coburn, C., Idris, M., Li, Y., Djurovich, P. I., Thompson, M. E., & Forrest, S. R. (2019). Understanding molecular fragmentation in blue phosphorescent organic light-emitting devices. *Organic Electronics*, *64*, 15–21. https://doi.org/10.1016/j.orgel.2018.10.001

144. Tsai, T.-C., Hung, W.-Y., Chi, L.-C., Wong, K.-T., Hsieh, C.-C., & Chou, P.-T. (2009). A new ambipolar blue emitter for NTSC standard blue organic light-emitting device. *Organic Electronics*, *10*(1), 158–162. https://doi.org/10.1016/j.orgel.2008.10.017

145. Adachi, C., Kwong, R. C., Djurovich, P., Adamovich, V., Baldo, M. A., Thompson, M. E., & Forrest, S. R. (2001). Endothermic energy transfer: A mechanism for generating very efficient high-energy phosphorescent emission in organic materials. *Applied Physics Letters*, *79*(13), 2082–2084. https://doi.org/10.1063/1.1400076

146. Schmidbauer, S., Hohenleutner, A., & König, B. (2013). Chemical Degradation in Organic Light-Emitting Devices: Mechanisms and Implications for the Design of New Materials. *Advanced Materials*, *25*(15), 2114–2129. https://doi.org/10.1002/adma.201205022

147. Tamayo, A. B., Alleyne, B. D., Djurovich, P. I., Lamansky, S., Tsyba, I., Ho, N. N., … Thompson, M. E. (2003). Synthesis and Characterization of Facial and

Meridional Tris-cyclometalated Iridium(III) Complexes. *Journal of the American Chemical Society*, *125*(24), 7377–7387. https://doi.org/10.1021/ja034537z

148. Holmes, R. J., Forrest, S. R., Sajoto, T., Tamayo, A., Djurovich, P. I., Thompson, M. E., … Brown, J. J. (2005). Saturated deep blue organic electrophosphorescence using a fluorine-free emitter. *Applied Physics Letters*, *87*(24), 243507. https://doi.org/10.1063/1.2143128

149. Turner, E., Bakken, N., & Li, J. (2013). Cyclometalated Platinum Complexes with Luminescent Quantum Yields Approaching 100%. *Inorganic Chemistry*, *52*(13), 7344–7351. https://doi.org/10.1021/ic302490c

150. Hang, X.-C., Fleetham, T., Turner, E., Brooks, J., & Li, J. (2013). Highly Efficient Blue-Emitting Cyclometalated Platinum(II) Complexes by Judicious Molecular Design. *Angewandte Chemie International Edition*, *52*(26), 6753–6756. https://doi.org/10.1002/anie.201302541

151. Shirasaki, Y., Supran, G. J., Bawendi, M. G., & Bulović, V. (2013). Emergence of colloidal quantum-dot light-emitting technologies. *Nature Photonics*, *7*(1), 13–23. https://doi.org/10.1038/nphoton.2012.328

152. Li, G., Fleetham, T., Turner, E., Hang, X.-C., & Li, J. (2015). Highly Efficient and Stable Narrow-Band Phosphorescent Emitters for OLED Applications. *Advanced Optical Materials*, *3*(3), 390–397. https://doi.org/10.1002/adom.201400341

153. Mashford, B. S., Stevenson, M., Popovic, Z., Hamilton, C., Zhou, Z., Breen, C., … Kazlas, P. T. (2013). High-efficiency quantum-dot light-emitting devices with enhanced charge injection. *Nature Photonics*, *7*(5), 407–412. https://doi.org/10.1038/nphoton.2013.70

APPENDIX A

DATA OF MATERIALS AND OLED DEVICES

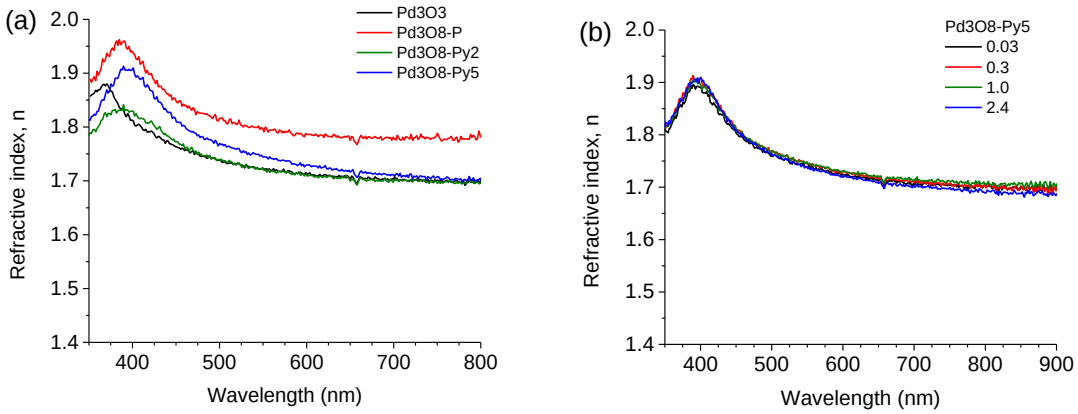

Figure A.1 Plots of refractive index versus wavelength for a) Pd3O3, Pd3O8-P, Pd3O8-Py2 and Pd3O8-Py5 vapor-deposited films and b) Pd3O8-Py5 thin films with various deposition rates of 0.03, 0.3, 1.0, 2.4 Å s^{-1} grown on silicon substrate.

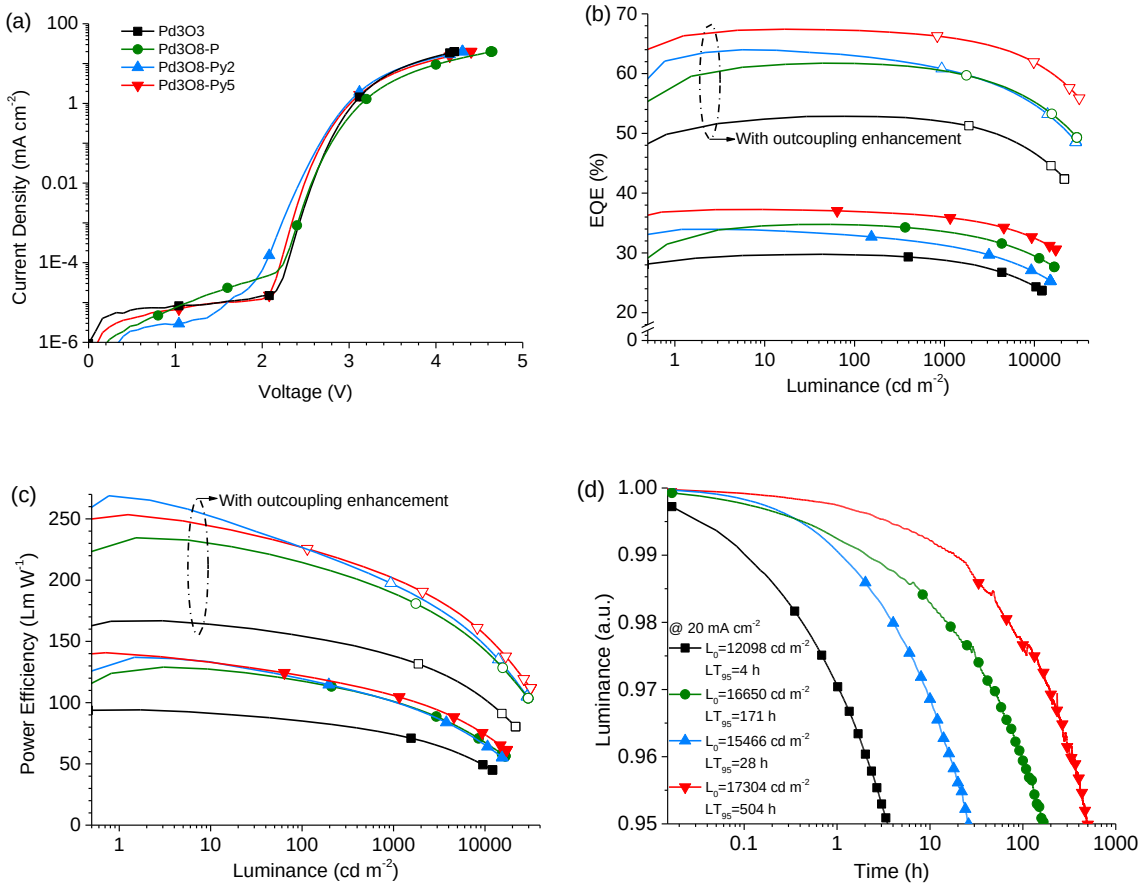

Figure A.2 a) Current density–voltage characteristics, b) EQE versus luminance, c) power efficiency (PE) versus luminance, and d) plots of relative luminance versus operational time at a constant current density of 20 mA cm^{-2} for Pd3O3, Pd3O8-P, Pd3O8-Py2 and Pd3O8-Py5 based devices. The general device structure is ITO/ HATCN (10 nm)/ NPD (70 nm)/ TrisPCz (10 nm)/ emitter (20 nm)/ BAlq (10 nm)/ BPyTP (50 nm)/ LiF (1 nm)/ Al (100 nm). EQE and PE versus luminance of the devices with optical outcoupling enhancement were measured by applying index matching gel between silicon photodiode and glass substrate.

APPENDIX B

LIST OF SELECTED PUBLICATIONS

In this dissertation, Chapters 3 and 4 are modified versions of papers published or to be submitted for publication.

Chapter 3:

Cao, L., Klimes, K., Ji, Y., Fleetham, T., & Li, J. (2021). Efficient and stable organic light-emitting devices employing phosphorescent molecular aggregates. Nature Photonics, 15(15), 230–237. https://doi.org/10.1038/s41566-020-00734-2.

Cao, L., Zhu, Z.-Q., Klimes, K., & Li, J. (2021). Efficient and Stable Molecular Aggregate Based Organic Light Emitting Diodes with Judicious Ligand Design. Adv. Mater. https://doi.org/10.1002/adma.202101423.

Chapter 4:

Cao, L., Li, J., Zhu, Z.-Q., Huang, L., & Li, J. Stable and Efficient Near-Infrared Organic Light-Emitting Diodes Employing a Platinum(II) Porphyrin Complex, submitted.